FINITE ELEMENT ANALYSIS OF ICE-STRUCTURE INTERACTION WITH A VISCOELASTIC MODEL COUPLED WITH DAMAGE MECHANICS

CHUANKE LI

Finite Element Analysis of Ice-structure Interaction with a Viscoelastic Model Coupled with Damage Mechanics

by

© Chuanke Li, B.Eng

A thesis submitted to the School of Graduate Studies
In partial fulfillment of the requirement for the degree of
Master of Engineering

Faculty of Engineering and Applied Science
Memorial University of Newfoundland
September 2002

St. John's Newfoundland Canada

Abstract

Medium scale ice indentation tests were conducted at Hobson's Choice Island in 1989 and 1990. A damaged layer was found near the contact interface of the indentor and ice mass. The fluctuation of ice load is believed to be related to the layer. Triaxial small scale tests have been conducted at Memorial University of Newfoundland. The tests showed that microcracking is dominant at low confining pressure levels and recrystallization and pressure melting are dominant under high confining pressure levels. At the medium pressure levels, both the two mechanisms are inhibited and damage remains low. The tests also showed that increasing temperature has a softening effect on ice. The data of the tests is used to calibrate the damage parameter as a function of confining pressure and deviatoric stress. Strain localization and rupture observed from these tests are also studied.

A constitutive model coupled with damage effects was established for finite element implication. Both the triaxial small-scale test and medium scale test are simulated by the finite element program, ABAQUS. Results of small-scale model show that inhomogeneity plays a significant role in triggering the strain localization and its consequent rupture. Results of medium-scale model are compared with the field data and they show a good agreement. The damage evolution process, stress state, energy flux and scale effect are also investigated.

Acknowledgements

I greatly appreciate my supervisor, Dr. Ian Jordaan, for all his support and academic guidance and instruction during the course of this work. The interest and patience he has shown throughout the research period have been singular. His suggestions and insights regarding the fundamentals of this topic have been invaluable. The approach to independent study which he has sought to instill, I believe, was not only an encouragement for the task at hand but also should prove very useful in future research and even a precious asset for the future career. I would also like to acknowledge the Faculty of Engineering and Applied Science and The School of Graduate Studies in Memorial University of Newfoundland for the many ways in which they have helped me to complete this project.

Special thank to Dr. Paul Barrette, for his guidance of the data of tests as well as valuable suggestions and discussion during the work, and to my friends and colleagues, Mr. Paul Stuckey and Mr. John Pond, for their sincere concern and help in this work. Finally, I wish to especially thank my dear wife, Haiyan Li, for her endless support and encouragement.

Contents

List of Figures

List of Tables

Nomenclature

C_{ijkl}	compliance tensor
D	damage parameter in Kachanov's damage concept
$D(t)$	creep compliance
E	elastic modulus (MPa)
E'	elastic modulus at current state (MPa)
E_0	original elastic modulus before damage (MPa)
E_K	elastic modulus in Kelvin unit
E_R	reference elastic modulus in Shapery's model (MPa)
$E(t)$	relaxation modulus
G	shear modulus (MPa)
G'	shear modulus at current state
G_0	original shear modulus before damage (MPa)
H	plastic hardening modulus
K	bulk modulus (MPa)
K_0	original bulk modulus before damage (MPa)
K_{ijkl}	forth order stiffness tensor
N	crack density
$\dot{N}_c$	reference growth rate of crack density
P	hydrostatic pressure (MPa)
P_c	confining pressure (MPa)
Q	activation energy
R	Boltzman constant (8.314 J $mol^{-1}K^{-1}$)
S	damage parameter
S_{cs}	damage parameter under constant stress conditions
S_e	damage parameter under experimental conditions
T	temperature (°C)
T_m	melting temperature of ice (K)
W	strain energy
W_c	complementary strain energy
V	initial volume in Schapery's approach (m^3)
a	one half of the crack length (m)
d	average grain size (m)
e	equivalent strain
e_{ij}^e	elastic strain deviator
e_{ij}^d	delayed elastic strain deviator

e_{ij}^{c}	viscous strain deviator
m	creep exponent for Maxwell unit
n	creep exponent for Kelvin unit
p_1	reference confining pressure (MPa)
p_2	reference confining pressure (MPa)
γ	total shear strain
γ_p	shear strain for plastic loading
γ_v	inelastic shear strain
s	von Mises stress (MPa)
s_{cs}	constant effective stress (MPa)
s_e	experimentally effective stress (MPa)
s_i	entropy of ice
s_w	entropy of water
s_{ij}	stress deviator (MPa)
v_i	volume of ice (m^3)
v_w	volume of water (m^3)
β	strain enhancement factor
β_d	delayed elastic strain enhancement factor
β_c	creep strain enhancement factor
δ_{ij}	delta function
ε	total strain of Burgers body
ε^e	instantaneous elastic component in Burgers body
ε^d	delayed elastic component in Burgers body
ε^c	viscous component in Burgers body
ε_v	volumetric strain
$\dot{\varepsilon}^d$	delayed elastic strain rate in Burgers body
$\dot{\varepsilon}^c$	creep strain rate in Glen's law
$\dot{\varepsilon}_0^c$	reference creep strain rate
$\dot{\varepsilon}_0^d$	reference delayed elastic strain rate
$\dot{\varepsilon}_{ij}^d$	delayed elastic strain rate tensor
$\dot{\varepsilon}_{ij}^c$	creep strain rate tensor
μ	viscous coefficient
ν	Poisson's ratio
ν_0	original Posson's ration before damage
σ	stress (MPa)
σ_{ij}	stress tensor (MPa)
σ_{ij}'	the components of a constant symmetric tensor in Schapery's approach
σ_0	reference stress (MPa)

σ_c	critical stress for crack nucleation (MPa)
σ_v	volumetric stress (MPa)
ψ	reduced time or pseudo-time (s)
φ_i	elastic compliance modulus in broad spectrum method (MPa^{-1})
η_i	viscous coefficient in broad spectrum method (MPa^{-1})
τ	shear stress (MPa)

Chapter 1

Introduction and Outline

In arctic and sub-arctic water areas, sea ice and icebergs provide a challenge to oil and gas industry. This leads to a focus on an adequate understanding of the mechanical behaviour of ice during its interaction with an offshore structure. The objective of the present research is to develop mechanical models for ice-structure interaction that will aid in the design of offshore structures subjected to impacts with ice in arctic and sub-arctic waters.

The load acting on structures during an ice impact event is transmitted though localized, short-lived zones of intense high pressure along the contact surface (see Figure 1.1). Theses zones are called " hot spots" or " critical zones". In ship ramming trials on sea ice with the icebreaker C.C.G.S. Louis S. St. Laurent in 1994 at North Pole, numerous local peaks in pressure were recorded on the hull during contact. Medium scale indentation tests on Hobson's Choice Ice Island have shown peak pressures reaching as

high as 70 MPa (Frederking *et al.* 1990a,b). Understanding of the high-pressure zones will not only aid in estimating the global impact force but also should be valuable to the design of individual components making up the structure. A probabilistic model of high-pressure zones has been developed based on the idealization of the high pressure zones as a point load by Jordaan *et al.* (1993). The present research will develop a mechanical model to predict the local impact load and the pressure distribution within these zones. In order to establish the model, it is necessary to understand the deformation under compressive loading conditions. A power law relationship is well recognized for a small amount of deformations in ice. However, the ice within the contact zones shows large deformations and the formation of a damaged layer. Small-scale experiments in Memorial University of Newfoundland showed that damage can enhance the deformation of ice significantly (Meglis *et al.* 1999, Melanson, 1998 and Barrette, in preparation). In this research a mechanical model based on Glen's law coupled with damage mechanics is formulated. The damage parameter to be used in this research is based on the Schapery's approach (Schapery, 1991), which has been further developed by Xiao (1997) and Jordaan (2001) to include the pressure softening effects. The damage model has been calibrated against triaxial small-scale tests carried out at Memorial University of Newfoundland. Since a small-scale specimen can be treated as an element in the ice mass of a medium scale test, the calibrated model can be applied to large models. The model has been applied to the study of the failure modes of ice specimens under compressive loading conditions. Finite element analysis with a UMAT (user's material subroutine) is used to predict the formation of the layer and the stress distribution of a medium-scale

test. Scale effect of high-pressure zones is also studied in this thesis, because it is important for predicting the local design load of the offshore structures.

The scope of the present research can be outlined as follows:

1. Literature review of the mechanical behavour of ice, including ice mechanics, damage mechanics, Schapery's approach and the coupled model of ice mechanics and damage mechanics.
2. Description of the medium-scale tests and triaxial small-scale tests. Discussion of the formation of the damage layer in medium-scale tests and the failure modes of small-scale specimens.
3. Constitutive model for finite element application; analysis of triaxial small-scale tests to calibrate the constants in the damage model.
4. Study of mechanisms of strain localization and numerical analysis for the understanding of potential mechanisms of strain localization and rupture in ice specimens.
5. Finite element analysis of an indentation test to study the damage evolution, stress distribution, formation of the layer and scale effect of high-pressure zones.

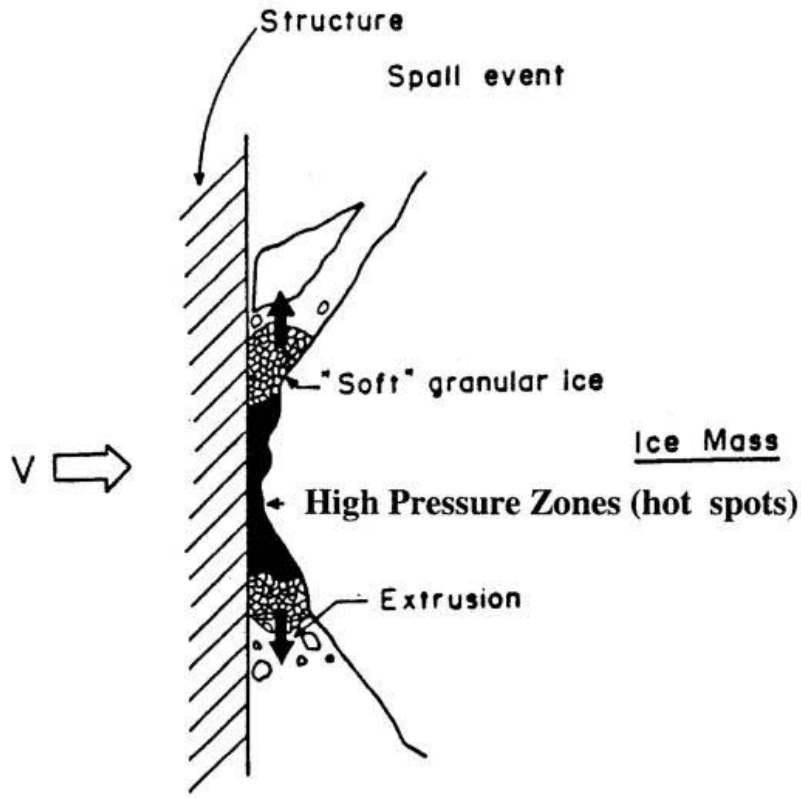

Figure 1.1 Sketch of hot spots (modified from Jordaan and Xiao, 1992).

Chapter 2

Review of Relevant Mechanics

In order to develop a model for the interaction between ice and structures, a proper understanding of the mechanical behaviour of ice is necessary. In this chapter, the mechanical behaviour of ice with and without damage effects is reviewed.

2.1 Viscoelastic Model

The mechanical properties of ice, as described by Sanderson (1988) can be classified into two areas: continuum ductile behaviour and brittle behaviour. The second is related to high strain rates, high strain levels and the development of a large number of cracks which will be studied in Section 2.3. In this section, the continuum ductile behaviour under small strain levels is reviewed and fresh water ice is discussed unless otherwise indicated. A large number of studies based on experimental work under uniaxial and

biaxial stress conditions have been undertaken (Sinha, 1979, 1982; Mellor and Cole, 1983; Cole, 1983; Jacka and Maccagnan,1984; Smith and Schulson,1993, Jezek, *et al.* 1985). A number of studies under triaxial stress conditions have also been performed (Jones,1982; Stone *et al.*, 1989; Kalifa *et al.*, 1992; Rist and Murrel, 1994; Rist *et al.*, 1994, Stone *et al.*, 1997, Melanson, 1998; Meglis *et al.*, 1999). A review of recent experiments under triaxial stress conditions was made by Barrette (2001).

A typical creep curve of ice under constant stress conditions is shown in Figure 2.1. It can be divided to three phases: primary creep (delayed elastic strain), secondary creep (viscous strain) and tertiary creep. A viscoelastic model shown in Figure 2.2 including a Maxwell unit and Kelvin unit has been used to model the ice behavior by Jordaan and McKenna (1988) and Xiao (1991). The spring in the Maxwell unit represents the instant elastic strain whereas the dashpot represents the viscous strain. The Kelvin unit represents the delayed elastic strain. The tertiary strain is related to microcracking and recrystalization as described by Sanderson (1988) and will be discussed in Section 2.3. Therefore, the total strain of ice under constant stress conditions can be expressed as:

$$\varepsilon = \varepsilon^e + \varepsilon^d + \varepsilon^c , \tag{2.1}$$

where ε^e is the instantaneous elastic component; ε^d is the delayed elastic component and ε^c is the viscous component.

2.1.1 Elasticity of Ice

Granular ice is typically treated as an isotropic material in engineering problems. Two constants can characterize its elastic properties: the elastic modulus E, and the Poisson's ratio, v. Following Hooke's law, the elastic strain of ice is given as

$$\varepsilon^e = \frac{\sigma}{E}. \tag{2.2}$$

The elastic modulus can be determined by reading the initial tangent value from a stress strain curve obtained from a very rapid test. This is not very accurate since ice creeps at any stress. This effect can be minimized by high frequency measurements.

Although the elastic modulus and Poisson's ratio vary with temperature and a temperature dependent equation was given by Glen (1975), it was shown (Sinha,1978) that the effect of temperature on the elastic modulus is not significant and can be neglected. A study by Sinha (1989) shows that the elastic modulus varies from 9 GPa to 10.16 GPa and v varies from 0.308 to 0.365 in the temperature range of -50 °C to 0 °C. With the high frequency dynamic measurements, the elastic modulus varies from 9 to 9.5 MPa in a temperature range of -5 °C to -10 °C and the Poisson's ratio varies from 0.3 to 0.33 for polycrystalline ice of low porosity (Mellor, 1983). Mellor's work also shows that the elastic modulus of sea ice is highly dependent on the porosity and varies from 10 GPa to 1 GPa when the porosity is from 0 to 0.3. Theoretical and experimental models for calculating the elastic modulus of sea ice as a function of brine volume have been proposed by Schwarz and Weeks (1977).

2.1.2 The Creep of Ice

Under small strain levels, the creep of ice includes two phases as shown in Figure 2.1: delayed elastic strain (primary creep) and viscous strain (secondary creep).

The viscous strain is the permanent component of the total strain. Physically, it is associated with dislocation movements within the grains. Glen's law (Glen, 1955) is commonly accepted for polycrystalline ice under uniaxial compression or tension conditions. It is expressed as follows:

$$\dot{\varepsilon}^c = A\sigma^n, \tag{2.3}$$

where n is a material constant and A is a shift factor of temperature in the form of:

$$A = B\exp(-Q/RT), \tag{2.4}$$

where B is a material constant; Q is the activation energy; R is Boltzman constant (R = 8.314 J $mol^{-1}K^{-1}$); T is absolute temperature. It can be seen from Eq. (2.4) that ice obeys the thermorheologically simple principle. The thermorheologically simple principle means that once the behaviour of a material at a given temperature is known, the behaviour at other temperature of interest can be obtained by a shift factor. Sinha (1978) confirmed that ice follows the thermorheologically simple principle at small strain levels as described in Eq.(2.4) and without considering the temperature effect, the following equation was applied in his model:

$$\dot{\varepsilon}^c = \dot{\varepsilon}_0^c(\sigma/\sigma_0)^n, \tag{2.5}$$

where $\dot{\varepsilon}_c^0$ and σ_0 are the reference strain rate and stress, respectively.

Jonas and Muller (1969) developed an equation expressed below including dynamic recrystallization on strain rate.

$$\dot{\varepsilon} = \phi_f \exp(-\frac{\Delta H}{KT})\exp(\frac{v[\tau - \tau_B]}{KT}) \tag{2.6}$$

where ϕ_f is a structure factor ; ΔH is the activation energy in the presence of pressure, v is activation volume; τ is the shear stress and τ_B is the internal generated back stress. A similar model for viscoelastic materials was also studied by Findley *et al.* (1976) and Schapery (1997b).

The delayed elastic strain is totally recoverable after the unloading process (see Figure 2.1) if time is long enough. Physically, it is related to grain distortion and sliding due to the shear stress generated between the grain boundaries. Sinha (1978, 1983) developed a grain size and temperature dependent equation based on viscoelastic theory under constant and monotonic uniaxial loading conditions expressed as follows:

$$\varepsilon^d = \frac{cd_1}{d}(\frac{\sigma}{E})^s[1 - \exp(-(\alpha_T t)^b)], \tag{2.7}$$

where c, s, b and α_T are all constants dependent on temperature T and grain size d; d_1 is the unit grain size.

A general nonlinear viscoelastic model was given by Jordaan and McKenna (1988). It was based on the assumption that the viscous coefficient is power law dependent on stress inside the dashpot of the Kelvin unit described as follows:

$$\mu_K = \frac{1}{C\sigma_d^{n-1}}, \tag{2.8}$$

where C and n are a constant; and σ_d is the stress inside the dashpot.

Then, in the Kelvin unit of Figure 2.2, the governing equation for equilibrium under constant stress conditions will be:

$$\dot{\varepsilon}^d = \frac{\sigma_s}{E_K} = -\frac{\sigma_d}{E_K}, \tag{2.9}$$

where E_K is the elastic modulus of the Kelvin unit and σ_s is the stress inside the spring of the Kelvin unit.

Therefore, by a mathematical transformation of Eq.(2.9), the following equation can be obtained.

$$\frac{d\sigma_d}{\sigma_d} = -\frac{E_K}{\mu_K(\sigma_d)}dt. \tag{2.10}$$

By integrating the both sides, the delayed elastic strain can be expressed as follows:

$$\varepsilon^d = \frac{\sigma}{E_K}[1-\exp\{-E_K\int_0^t \frac{1}{\mu_K(\sigma_d)}dt\}], \tag{2.11}$$

where $\int_0^t \frac{1}{\mu_K(\sigma_d)}$ is called the pseudo-time or reduced time.

The delayed elastic strain which includes both the stress nonlinearity and temperature dependence was proposed by Schapery (1997a) as follows:

$$\varepsilon^d = \int_0^t J[\psi(t)-\psi(\tau)]\frac{d\sigma}{d\tau}d\tau + \int_0^t \alpha_d[\psi(t)-\psi(\tau)]d\tau, \tag{2.12}$$

where J represents the creep compliance, ψ is the reduced time including both the stress and temperature effects, and α_d is the thermal expansion tensor.

2.1.3 Broad Spectrum Method

Since ice is a highly nonlinear viscoelastic material, more accurate results will be achieved if a chain of Kelvin units with spectrum values for the springs and dashpot are applied to model the delayed elastic strain. A spring-dashpot model with a series of Kelvin units is shown in Figure 2.3. For linear viscoelastic materials, using the Boltzmann superposition principle, the strain for creep test and stress for relaxation tests, respectively, can be expressed by two hereditary integrals (Flugge, 1975):

$$\varepsilon(t) = \int_0^t J(t-\tau)\frac{d\sigma}{d\tau}d\tau \tag{2.13}$$

$$\sigma(t) = \int_0^t E(t-\tau)\frac{d\varepsilon}{d\tau}d\tau, \tag{2.14}$$

where $J(t)$ is called the creep compliance and $E(t)$ is called the relaxation modulus. Based on the theymodynamics of irreversible processes, the creep compliance and relaxation modulus for the broad spectrum method described in Figure 2.3 can be expressed in the following manner:

$$J(t) = \frac{1}{E_1} + \frac{t}{\mu_1} + \sum_2^N \varphi_i\{1-\exp(-\frac{t}{t_c^i})\}$$

$$E(t) = E_1 + \sum_2^N E_i\{1-\exp(-\frac{t}{t_c^i})\}, \tag{2.15}$$

where $\varphi_i = 1/E_i$ and $t_c^i = \frac{\eta_i}{E_i}$.

If the number of Kelvin elements in the model increases indefinitely, the creep compliance becomes (Findley *et al.*, 1976):

$$J(t) = \frac{1}{E_1} + \frac{t}{\mu_1} + \int_0^{\infty} \varphi(t_c)\{1 - \exp(-\frac{t}{t_c})\}dt_c \,. \tag{2.16}$$

The relaxation modulus takes a similar form.

For nonlinear materials such as ice, a stress dependent viscous coefficient should be used instead of a constant value in Eq.(2.15) or Eq.(2.16). Jordaan *et al.* (1988) and Xiao (1997) used two Kelvin elements and three Kelvin elements in the model, respectively. The comparison of creep test results under constant stress conditions with Xiao's broad spectrum model results is illustrated in Figure 2.4. In practice, as pointed out by Jordaan *et al.* (1990), for a series of Kelvin units a spectrum of retardation times with a distribution function is required, which will increase significantly the difficulty and complexity for modeling and fitting of the experimental data. In this research, because delayed elastic strain becomes small compared to viscous strain as studied by Xiao (1991) and Melanson (1998), a simplified model with one Kelvin unit as shown in Figure 2.2 is applied to model the ice mechanical behaviour.

2.2 Review of Damage Mechanics

2.2.1 The Concept of Damage Mechanics

Modern engineering materials subjected to unfavorable mechanical and environmental conditions undergo microstructural changes which decrease their strength. Since these changes impair the mechanical properties of these materials, the term "damage" is used. The changes of material structure mentioned are, in general, irreversible, since during the process of damage the entropy increases. Damage can be

caused by microcracks or fracture. Thermal effects and environmental degradation factors can also contribute to damage of structures.

Much of the early work done in the field of damage mechanics was performed by Kachanov (1958). In his later work (Kachanov, 1986), the damage on a structure was measured by a scalar parameter defined as the ratio between the area of voids (caused by damage) and the overall area of the structure. Consider an undamaged material under uniaxial loading. The stress is defined as

$$\sigma = \frac{P}{A_0}, \tag{2.17}$$

where P is the uniaxial force, and A_0 is the original, undamaged area. If the material undergoes isotropic damage, the amount of damage can be "measured" using the variable:

$$D = \frac{A}{A_0}, \qquad (0 \le D \le 1) \tag{2.18}$$

where A is the damaged area (voids and cracks openings, see Figure 2.5). Because of damage in the material, the effective stress in the material is increased and the material is not as strong as it was originally. The effective stress is given as:

$$\sigma_{eff} = \frac{P}{A_0 - A} = \frac{P}{A_0(1-D)} = \frac{\sigma}{1-D}. \tag{2.19}$$

The strain experienced by the damaged material is only influenced by the effective stress σ_{eff}. Thus

$$\varepsilon = \frac{\sigma_{eff}}{E_0} = \frac{\sigma}{E_0(1-D)} = \frac{\sigma}{E}, \tag{2.20}$$

where E_0 = "original" modulus (undamaged material) and $E = E_0(1 - D)$ is called the "effective" modulus. The "effective" modulus is reduced from the "original" modulus by the presence of damage. As damage increases, the "effective" modulus decreases. By using the effective modulus in place of the original modulus, the material can be analyzed in the same manner as undamaged material.

2.2.2 Reduction of Elastic Properties of Solids by Microcracks

Much research has been done in finding the effective elastic moduli of cracked solids for arbitrary crack orientation statistics. Budianski and O'Connell (1976) investigated the reduction in the elastic modulus of specimen under tensile loading due to microcracking. The investigation was based on the strain energy loss during the nucleation of each individual crack. The tension across the crack surface was not considered, and all cracks were considered open. Assuming that the cracks were isotropic in nature, the following relationship was determined:

$$D = a^3 N, \tag{2.21}$$

where a is the crack length and N is the crack density per volume. A similar damage parameter was obtained by Krajcinovic *et al.* (1981) and Krajcinovic (1983, 1985) based on thermodynamics.

According to the damage parameter described in Eq.(2.21), Budiansky and O'Connell (1976) and Sayers and Kachanov (1991) gave the effective elastic moduli of uniform cracked solids as follows:

$$E = E_0\{1 - D[16(1-\nu^2)(10-3\nu)]/[45(2-\nu)]\} \tag{2.22}$$

$$K = K_0\{1 - D[16(1-\nu^2)]/[9(1-2\nu)]\}, \tag{2.23}$$

where the subscript $_0$ represents the original moduli; E is Young's modulus, K is bulk modulus and ν is Poisson's ratio with the damage effect.

Horii and Nemat-Nasser (1983) investigated the same phenomena for the case of two-dimensional, plane strain and compressive state of stress. The authors stated that traction across the crack surface could not be ignored in a compressive state. The effect of compression on the reduction of the elastic modulus was not as significant as that of the tensile case. The compressive forces caused crack closure that greatly inhibited nucleation. Consider an elastic solid with N cracks per unit volume; each crack has a normal n^i. Given an applied stress σ^0 at the remote boundary, this configuration can be represented by the problem with crack surfaces loaded by tractions of $f^0 = n^i\sigma^0$ and stresses vanishing at infinity. A 3-D solution was proposed by Kachanov (1993) to approximate the effictive elastic modulus of noninteracting cracks with an isotropic random distribution. The effective moduli are given as follows:

$$\frac{E}{E_0} = (1 + C_1 N)^{-1}$$

$$\frac{G}{G_0} = (1 + C_2 N)^{-1}$$

$$\frac{v}{v_0} = (1 + C_3 N)^{-1}, \tag{2.24}$$

where,

$$C_1 = \frac{16(1-v_0^2)(1-3v_0/10)}{9(1-v_0/2)}$$

$$C_2 = \frac{16(1-v_0)(1-v_0/5)}{9(1-v_0/2)}$$

$$C_3 = \frac{8(1-v_0^2)}{45(1-v_0/2)}$$

2.3 Damage in Ice

During the development of tertiary strain as shown in Figure 2.1, ice may display a sudden or gradual change of deformation mechanism. This process is associated with microstructural changes of ice and may lead to a brittle fracture. The microstructural change may include microcracking nucleation and growth, dynamic recrystalization and pressure melting.

2.3.1 Cracking of Ice

There has been significant research conducted on the characterization of events leading up to initial crack formation and the subsequent crack propagation or coalescence. The onset of the microcracks is associated with the load level (5-10 MPa for uniaxial compression, 1-2 MPa for uniaxial tension), strain rate (10^{-3} s^{-1} for uniaxial

compression) and strain level (1% or more) [Sanderson, 1988; Cole, 1989]. The mechanisms under tensile loading conditions are different from those under compressive loading conditions. For tensile tests, the failure of ice is normally controlled by the unstable propagation of one crack. The most important distinction to make at the outset is that between nucleation of a crack and propagation of a crack. For compressive tests, the process of crack propagation is not so simple as under tension. The propagation of a single crack is highly restricted by the compression and final failure generally occurs by the linkage of a large number of cracks during a stable process.

Consider an initially homogenous specimen of intact ice subjected to a uniaxial tensile load. Crack nucleation appears to be associated with critical strain in the material as proposed by Seng-Kiong and Shyam Sunder (1985) or at a critical level of delayed elastic strain proposed by Sinha (1982). In either case, the physical process of crack nucleation occurs in order to relieve the stress concentrations developing at the grain boundaries during the early stage of the deformation (Schulson and Cannon, 1984). The stress for nucleation to occur shows a clear dependence on grain size. The dependence was modeled by Schulson *et al.* (1984, 1989) with an equation of the form:

$$\sigma_N = \sigma_0 + k/\sqrt{d}\,, \tag{2.25}$$

where σ_0 is 0.6 Mpa; k is 0.02 MPa $m^{1/2}$ and d is the grain size. Schulson's work also shows that the stress for propagation to occur also depends on grain size with an equation of the form:

$$\sigma_p = K_p/\sqrt{d}\,, \tag{2.26}$$

where K_p is an empirical constant with the same dimensions as fracture toughness K_{IC} (0.044 MPa $m^{1/2}$, experimentally). The stresses for nucleation and propagation described in Eq. (2.25) and (2.26) indicate that for grain size d greater than 1.5 mm, fracture is controlled by nucleation, while for d less than 1.5 mm, fracture is more likely controlled by propagation.

Gold (1972) conducted an experimental study on the compressive failure process in ice where an analysis on the dependence of microcracking activity with stress, strain and time was presented. The nucleation of cracks under compressive stresses occurs for the same reason as under tension. Studies by Hallam (1986) also indicated that as many as 50% of nucleated cracks are transgranular in character besides the cracks due to dislocation pile-up at grain boundaries and relief of stress concentration along the boundaries. Hallam (1986) and Seng-Kiong and Shyam Sunder (1985) have proposed that the crack nucleation under compressive stress conditions may occur simply when lateral tensile strain induced by Poisson expansion reaches a critical value.

Experimental studies by Cole (1986) provided quantitative data on length, density and orientation of cracks in polycrystalline ice. The length of cracks, $2a$, is proportional to the grain size d with an approximate relationship:

$$2a = 0.65d\,. \tag{2.27}$$

This relationship was justified by using concepts of elastic strain energy and surface energy by Cole (1986). The density of cracks is grain-size dependent and approximately one crack per grain for grain size exceeding about 5mm. The average absolute angle of

the cracks is 23° with a standard deviation of 17°. About 90% of the cracks were observed within 45° of the principal axis of compressive stress.

After the nucleation of cracks, under uniaxial stress conditions, the cracks tend to grow and align themselves with the principal axis of compression. A numerical study has been performed by Ashby and Hallam (1986). Studies by Kalifa *et al.* (1989) provided the critical stress for crack nucleation for triaxial stress conditions. The work shows that the confinement pressure has a significant effect on the crack nucleation. The results of their tests were regressed by the least squares method giving the following equation,

$$\sigma_1 - \sigma_3 = -2.47 + 0.4\sigma_3 . \tag{2.28}$$

Figure 2.6 shows the theoretical (dotted line) and experimental (solid line) results. It can be determined that the crack formation under compressive triaxial conditions is dominated by the remote effective stress (von Mises stress, $\sigma_1 - \sigma_3$) with a given pressure. The figure also shows that with the pressure increasing, the critical stress for crack nucleation also increases. In other words, pressure increase can inhibit crack nucleation. A similar study was perfomed by Schulson *et al.* (1991) with proportional triaxial stress conditions.

The final failure mode under triaxial test conditions is highly dependent on the confining pressure. Under very low confinement, the same trend as under uniaxial conditions, axial splitting, was found. With increasing confinement, shear fracture was observed by Schulson (1987), Rist *et al.* (1988) and Weiss and Schulson (1995). It has been proposed by Rist *et al.*(1988) and Weiss and Schulson (1995) that the fracture is

highly related to the boundary conditions. The ends of the ice specimen are fixed by the testing equipment which exerts frictional constraint on the ends of the specimen. Axial splitting is restricted by the end effects and increasing confinement. The linkage of the microcracks tends to be oriented along the direction of maximum shear stress. Work by Murrell *et al.* (1991) showed that shear fracture is also restricted and viscoelastic flow dominates the failure if the pressure keeps increasing to a certain level. Studies by Melanson *et al.* (1998) also showed that no fracture was observed when pressure is around 30 MPa. Microcracking and fracture of ice is also observed in indentation tests. Jordaan and Timco (1988) and Jordaan and McKenna (1988) studied the interaction between an ice sheet and flat indentors. A layer of crushed ice is formed in front of the indentor and the microcracks tend to form along the maximum shear stress, as shown in Figure 2.7(a). Jordaan and McKenna (1988) characterized the ice into three zones as shown in Figure 2.7(b): crushed zone, ice with microcracks and undamaged virgin ice.

2.3.2 Dynamic Recrystallization

Dynamic recrystallization is defined as a deformation-induced reworking of the grain sizes, shapes or orientation with little or no chemical change (Poirier and Guillope, 1979). Physically, dynamic recrystallization is a process involving the formation or migration of grain boundaries (Vernon, 1981). The driving force for the grain-boundary migration is due to the difference in strain energy between deformed grains and dislocation-free nuclei and it can be reduced by a large amount when the dislocation in the deformed grains rearrange into low-energy configurations by polygonization (Poirier, 1985).

Dynamic recrystallization was observed to have a significant effect on softening mechanical properties of materials and enhancing the creep discontinuously. The fundamental processes responsible for this effect are summarized by Urai *et al.* (1980) as: changes in grain size, changes in substructure, changes in preferred orientation and changes in grain boundary structure. The formation or migration of grain boundaries due to the dynamic recrystallization can either increase or decrease the grain size. The new generated grain size, D, depends only on the applied stress (Poirer, 1985):

$$\frac{D}{b} = K(\frac{\sigma}{\mu})^{-r} \tag{2.29}$$

where b, K, μ and r are constants; the value of r is usually somewhat larger than 1 and close to 1.2.

Studies by Duval *et al.* (1983) showed that dynamic recrystallization will not be initiated under very low stresses and it will be periodic under intermediate stresses leading to periodic increases of strain rate. Under high stress levels, the strain rate will be accelerated rapidly by the dynamic recrystallization. Studies by Urai (1986) at triaxial conditions for polycrystalline materials observed that dynamic recrystallization is dependent on hydrostatic pressure. It showed that when hydrostatic pressure is more than 28 MPa, the creep stress began to decrease with the increase of pressure. Therefore, the hydrostatic pressure with a certain level of shear stress has a softening effect on polycrystalline ice. Stone *et al.* (1997) and Meglis *et al.* (1999) have recently shown that dynamic recrystallization is a mechanism leading to enhanced creep rate.

2.3.3 Pressure Melting

The mechanism of deformation enhancement of ice at high pressures is believed to be associated with pressure melting besides dynamic recrystalization. The melting point of ice decreases with the increase of pressure. Some of the early work on pressure melting of ice was presented by Hobbs (1974). An equation based on thermodynamics is given as follows:

$$\frac{dT_m}{dp} = \frac{(v_w - v_i)}{(s_w - s_i)}, \tag{2.30}$$

where T_m is the melting temperature of ice in degrees Kelvin, p is pressure; v_w and v_i are the specific volume of water and ice, respectively; s_w and s_i are the entropy of water and ice, respectively. According to the thermodynamic second law, the denominator of the right-hand term will necessarily be positive. Since the density of water is greater than that of ice, the numerator of the Eq. 2.30 is negative. Therefore the melting point of ice is inversely proportional to the pressure. A general solution (the Clausius-Clapeyron equation) is given as:

$$dT_m = -Adp \tag{2.31}$$

where A is a constant dependent on temperature. For ice, A = 0.0743°C / MPa at 0°C and 0.0833°C / MPa at -10°C. At a pressure of 70 MPa, the ice specimen would be expected to melt at about -5.5°C. At a temperature of -10°C, melting occurs at 120 MPa. The results of the experimental work on the relationship between melting point and pressure by Nordell (1990) is plotted in Figure 2.8.

Since pressures of 70 MPa have been observed under field condition (Frederking *et al.*, 1990), the effect of stress concentrations in addition to these pressures may be sufficient during ice-structure interaction to initiate this mechanism at grain boundaries. Recent studies by Meglis *et al.* (1999) and Muggeridge and Jordaan (1999) presented the possible evidence of pressure melting in cylindrical ice specimens under triaxial conditions and the damage layer in the full-scale indentation tests, respectively.

2.4 Schapery's Model and Damage Evolution

2.4.1 Schapery's Model

Polycrystalline ice behaves as a brittle, nonlinear viscoelastic material under a wide range of conditions of engineering interest. The brittleness and polycrystalline structure combine to produce a significant level of distributed damage under compressive stress states. Schapery (1991) established a model for the deformation behaviour of viscoelastic media with distributed damage. His model was based on the correspondence principle, generalized J-integral and Modified Superposition Principle to express the overall strains ε_{ij}. The description is as follows:

$$\varepsilon_{ij} = E_R \cdot \int_0^t D(t-\tau)\frac{\partial}{\partial \tau}\left(\frac{\partial W_C'}{\partial \sigma_{ij}}\right)d\tau, \tag{2.32}$$

where $D(t-\tau)$ is creep compliance and may be got from experiments , E_R is a reference Young's modulus and W_C' is the free energy density which is a function of stress σ and damage parameter S. A proportional stress state is defined as:

$$\sigma_{ij} = \sigma\sigma_{ij}', \tag{2.33}$$

where $\sigma = \sigma(t)$ and σ_{ij}' are the components of a constant symmetric tensor.

The complementary strain energy density W_C' obeys a power-law relationship as follows.

$$W_c'(\sigma_{ij}) = |\sigma|^{r+1} W_c'(\sigma_{ij}'), \tag{2.34}$$

where W_C' also depends on the geometry of the time-varying microcracks, although not explicitly shown in Eq.(2.34). Note that $W_C' = W_C/V$, where W_C is the complementary strain energy and V is the initial volume. Thus Eq.(2.34) is valid even if tractions act on crack faces if these tractions are proportional to σ; such will be the case for closed cracks with crack-face sliding if the frictional traction is zero or proportional to the contact pressure.

Differentiating Eq.(2.34) with respect to σ_{ij} produces:

$$\frac{\partial W_c'}{\partial \sigma_{ij}} = |\sigma|^{r+1} \frac{\partial W_c'}{\partial \sigma_{ij}'} \frac{1}{\sigma} = |\sigma|^{r} \frac{\partial W_c'}{\partial \sigma_{ij}'} \mathrm{sgn}(\sigma), \tag{2.35}$$

where the tensor $\partial W_c'/\partial \sigma_{ij}'$ is independent of σ and is only a function of the damage parameter S, $g(S)$. By substituting Eq.(2.35) into Eq.(2.32), the following equation can be obtained:

$$\varepsilon_{ij} = E_R \cdot \int_0^t D(t-\tau)\frac{\partial}{\partial \tau}[|\sigma|^r g(S)\mathrm{sgn}(\sigma)]d\tau \tag{2.36}$$

For the application to ice, Jordaan *et al.* (1988) proposed an exponential form for the enhancement of inelastic strains (delayed elastic strain and viscous strain) as expressed in the following:

$$g = \exp(\beta S), \tag{2.37}$$

where β is a constant enhancement factor.

Schapery (1991) also established a non-proportional stress model for nonlinear viscoelasticity with distributed damage. In that case, a generalized force and displacement are used so that the traction on the crack faces can be included.

2.4.2 Derivation of Damage Parameter (Schapery's Approach)

Schapery (1981, 1984) developed a continuum damage approach based upon a generalized form of the *J*-integral. This approach included treatment of the energy flux into the crack from the tip, as well as the thin layer of damaged material outside the crack tip zone along the crack surface. The result was developed for materials with a nonlinear power law relationship between stress and strain subjected to proportional loading, Based upon results from past experimental studies, the crack growth rate can be expressed as:

$$\dot{a} = f_1 J^k, \tag{2.38}$$

where f_1 is a constant; a is a half crack length and J is the J - Integral.

Schapery (1984) proved the relationship of

$$J = \frac{\partial W_c}{\partial A}, \tag{2.39}$$

in which, $\partial A = Bda$ (B = crack width). Since J is proportional to the crack length a and W_c is proportional to σ^{r+1}, the following can be derived:

$$\dot{a} = c_2 a^k \sigma^q, \tag{2.40}$$

where c_2 and k are constants and $q = (r+1)k$. The relationship between the original crack length and the new crack length is found by integrating Eq.(2.40). The result is

$$\frac{a}{a_0} = \frac{1}{\left[1-(k-1)c_2 {a_0}^{k-1} S_\sigma\right]^{1/k-1}}. \tag{2.41}$$

where

$$S_\sigma = \int_0^t f_1 \sigma^q d\tau \tag{2.42}$$

is defined as Schapery's measurement of damage. A crack will become unstable when the denominator of Eq.(2.41) tends towards zero. Setting the denominator to zero results in

$$S_\sigma = \int_0^t f_1 \sigma^q d\tau = \left[(k-1)c_2 {a_0}^{k-1}\right]^{-1}. \tag{2.43}$$

The growth of damage and increase of the complementary strain energy is shown in Figure 2.9.

2.4.3 Damage Evolution in Ice and Its effects on Mechanical Behaviour

A constitutive model including the effect of damage has been studied by Karr (1985) under uniaxial conditions and Karr and Choi (1989), Jordaan and McKenna (1988), McKenna *et al.* (1989) and Schapery (1991), etc. under triaxal conditions. Based on Glen's law, the constitutive equation for inelastic behaviour of ice with damage enhancement can be expressed as:

$$\dot{\varepsilon} = c(\frac{\sigma}{\sigma_0})^n \exp(\beta S), \tag{2.44}$$

where c, n and β are constants, σ_0 is reference stress and S is the damage parameter. Jordaan and McKenna (1988), McKenna *et al.* (1989), Xiao (1991) and Jordaan and Xiao (1992) proposed an evolution of damage as:

$$S = \int_0^t a^3 \dot{N}_c (\frac{\sigma - \sigma_c}{\sigma_0})^m dt, \tag{2.45}$$

where a is the grain size, $\dot{N}_c$ is a reference rate, m is constant, σ_0 is a reference stress and σ_c is critical stress for crack nucleation.

Jordaan and McKenna (1991) proposed a similar model as Eq. (2.45) but with a exponential form instead of the power law dependence of stress.

$$S = \int_0^t \dot{N}_c \exp(\frac{\sigma - \sigma_c}{\sigma_0}) dt. \tag{2.46}$$

The models described in Eq. (2.45) and (2.46) were focused on the influence of microcracks on the mechanical behaviour of ice. This has been applied by Xiao (1991) to simulate the ice indentation tests at low speed levels.

Recently, models of damage evolution for ice have been established based on Schapery's approach. However, under triaxial conditions, the damage in ice as discussed in Section 2.3, the mechanisms of damage include not only the microcracking but also dynamic recrystallization and pressure melting. The mechanisms of damage are also highly pressure dependent. Under low confining pressure conditions, microcracking may dominate the damage evolution accompanying dynamic recrystallization. Under high confining pressure conditions, microcracking is significantly inhibited and dynamic recrystallization and pressure melting are the dominant mechanisms.

Models by Xiao (1997), Melanson (1998), Jordaan *et al.* (1999) and Jordaan (2001) separated the damage evolution to two components to interpret the pressure effects. In the model by Melanson (1998), the equation for damage evolution can be described as

$$S = \int [f_1(p)(\frac{\sigma}{\sigma_0})^m + f_2(p)(\frac{\sigma}{\sigma_0})^n]dt\,, \tag{2.47}$$

where m and n are constants; σ_0 is a reference stress; the first component of Eq. (2.47) represents the damage evolution rate of microcracking at low pressure levels; the second component of Eq.(2.47) represents the evolution rate of dynamic recrystallization and pressure melting for all the pressure levels; $f_1(p)$ and $f_2(p)$ can be expressed as

$$f_1(p) = \begin{cases} a_1(1-\frac{p}{p_1})^2 & \text{when } p \le p_1 \\ 0 & \text{when } p > p_1 \end{cases} \tag{2.48}$$

and

$$f_2(p) = a_2(\frac{p}{p_2})^r, \tag{2.49}$$

where a_1, a_2 and r are constants; the values of p_1 and p_2 are reference confinement pressure.

In the model of Xiao (1997), Jordaan *et al.* (1999) and Jordaan (2001), an exponential form of stress as expressed below was presented instead of a power law relationship in Eq. (2.47):

$$S = \int [f_1(p)(\frac{\sigma}{\sigma_0})^m + f_2(p)\exp(\frac{\sigma}{\sigma_0})]dt, \tag{2.50}$$

in which f_1(p) and f_2(p) have the same description as Eq. (2.48) and Eq. (2.49), respectively.

In the present research, Eq. (2.44) is used to predict the behaviour of ice under large deformations. Eq.(2.50) is applied to identify the damage parameter, S. The material constants in Eq.(2.50) have been calibrated through triaxial small-scale tests with temperature corrections.

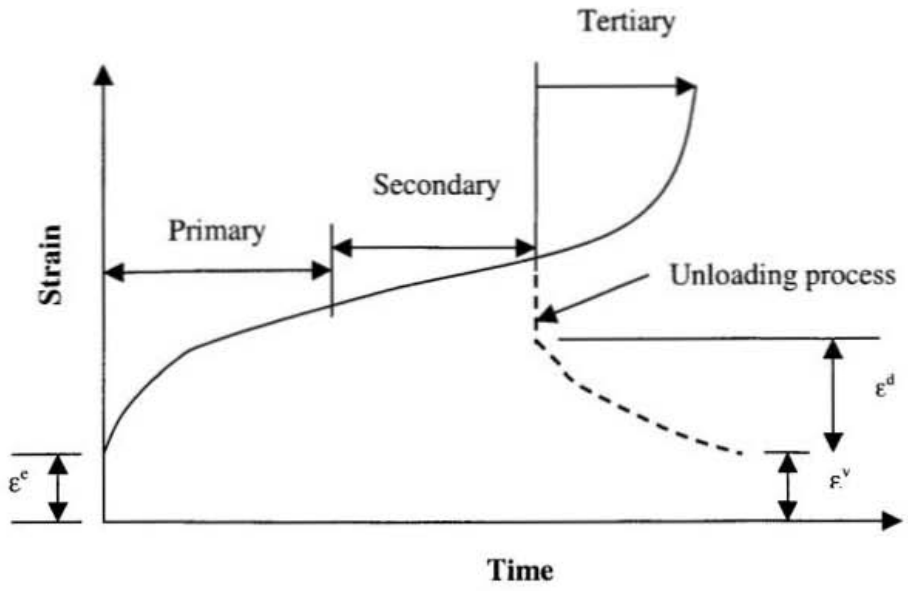

Figure 2.1 Strain history curve of ice under constant stress conditions.

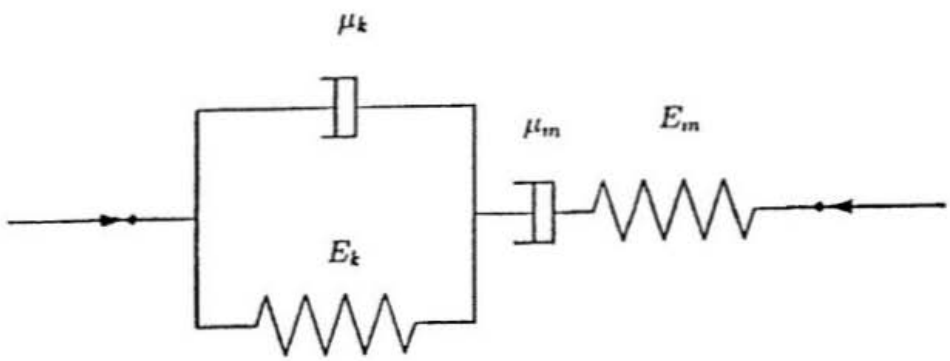

Figure 2.2 Schematic demonstration of Burgers model

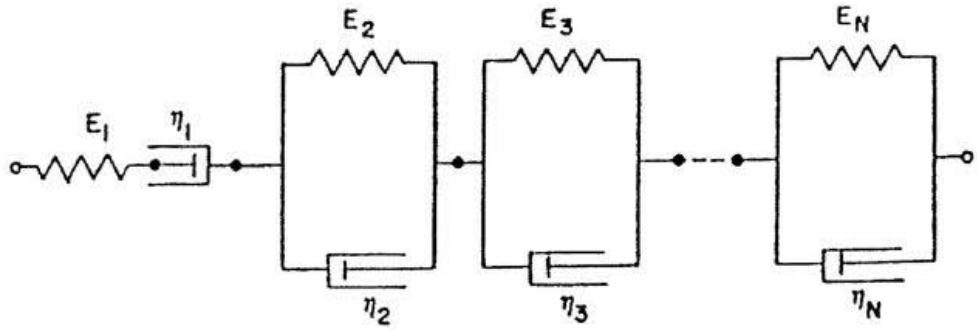

Figure 2.3 Illustration of the spectrum method with a series of Kelvin units

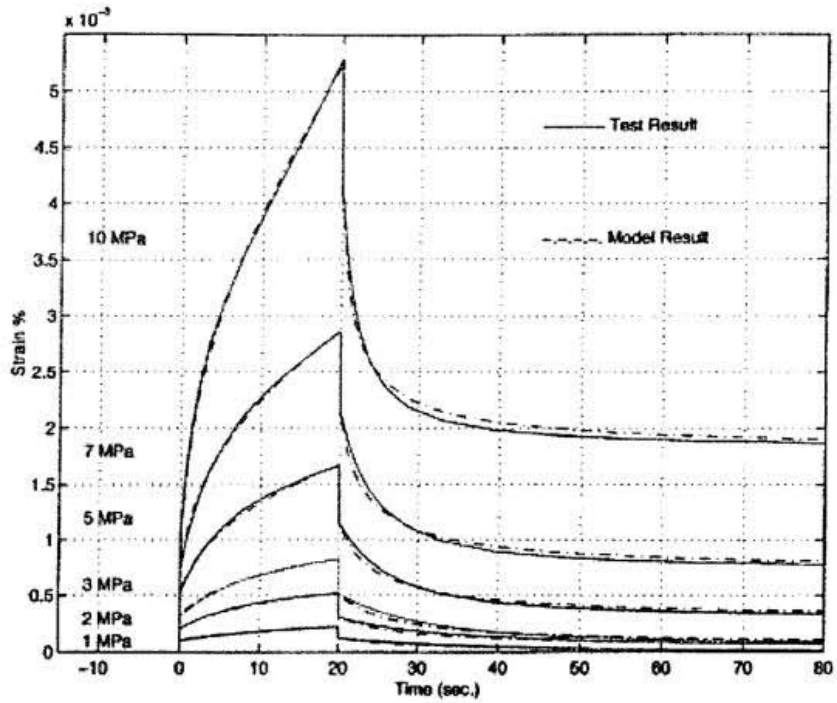

Figure 2.4 Comparison of creep test results with model results on intact ice under stress differences from 1 to 10 MPa and confinement of 10 MPa (Xiao, 1997).

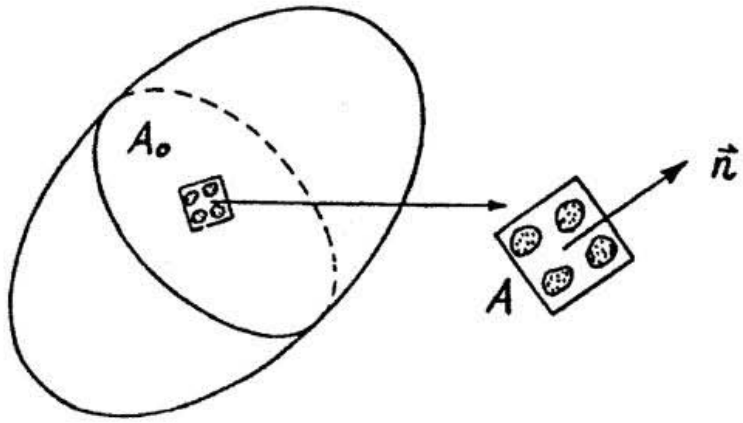

Figure 2.5 The overall area and the damaged area (Kachnov, 1986)

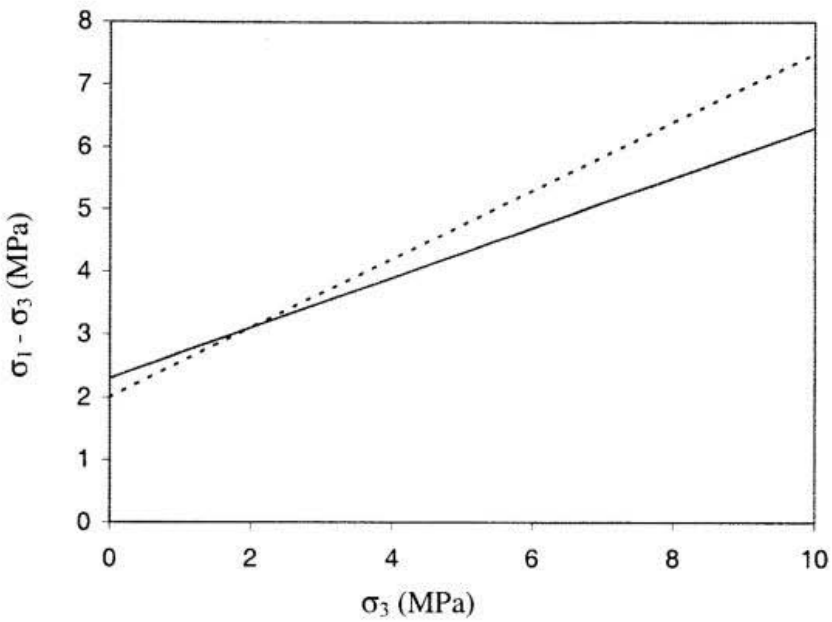

Figure 2.6 Theoretical and experimental critical differential stress as function of confining stress at triaxial compressive conditions. (Kalifa *et al.* 1989)

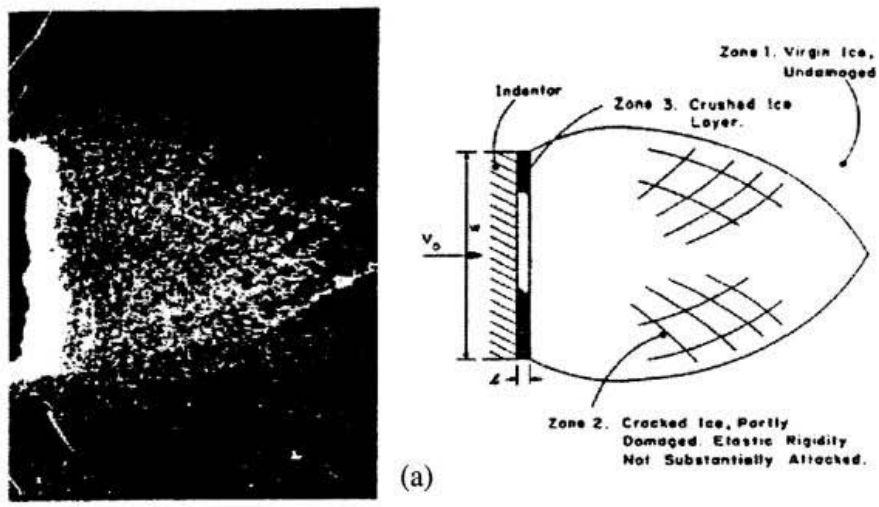

Figure 2.7 Idealizaion of contact zone; plan view (a) photographic representation showing progress of damage; (b) idealization into three zones (Jordaan and Timco, 1988)

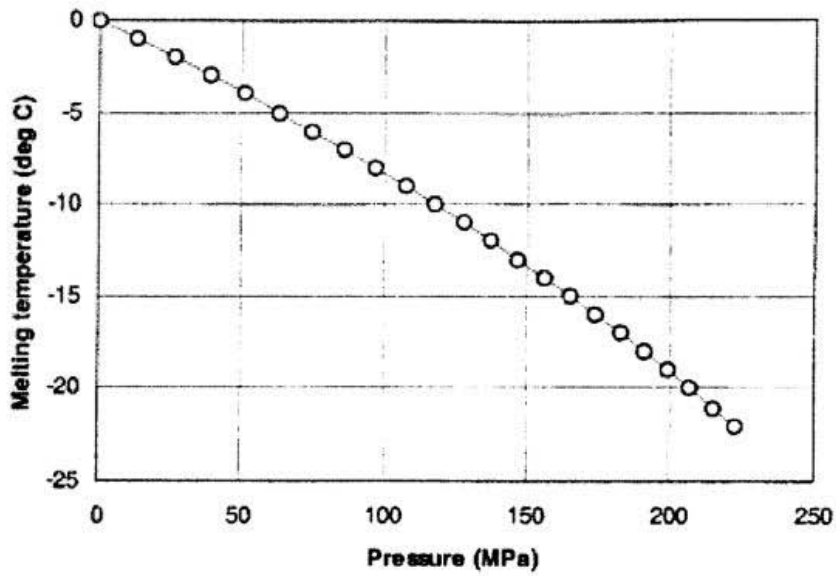

Figure 2.8 Variation of the melting temperature of ice with pressure (Nordell, 1990)

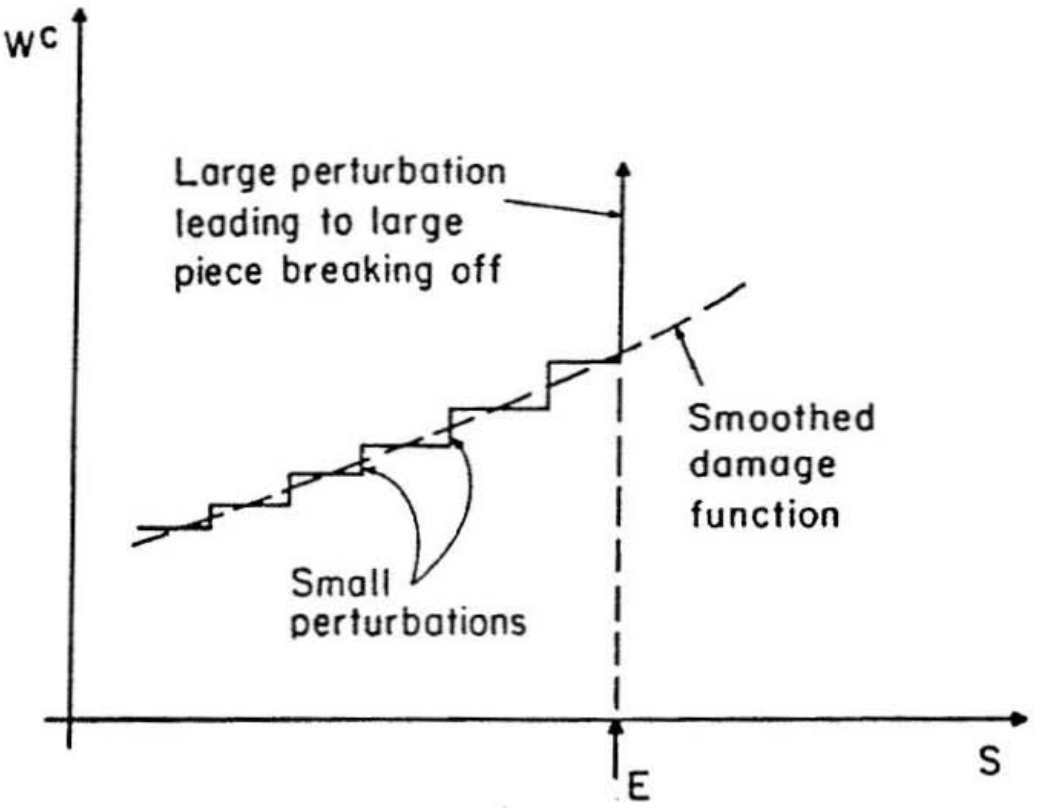

Figure 2.9 Growth of damage S and change in complementary strain energy W^C (Jordaan and Xiao, 1992).

Chapter 3

Experimentation

3.1 Introduction

Research in ice mechanics at the Ocean Engineering Research Centre of Memorial University of Newfoundland has focused on understanding the deformation of ice during impact with offshore structures. Jordaan (2001) proposed a model for the impact of ice with a structure. Three areas of pressure were distinguished in his model as shown in Figure 3.1. These three areas are parts of the nominal interaction area, defined as the projection of the structure onto the original shape (without spalls) of the ice feature. The three areas are then the spalled area, of zero pressure for edge spalls; the area across which crushed ice extrudes, of moderate pressure; and finally the high-pressure zones which apply most of the load. They fluctuate in positions and magnitude during the impact process.

The load acting on a structure during an ice impact event is transmitted through the localized, short-lived zones of intense high pressure at the interaction interface. Jordaan *et al.* (1993) proposed a probabilistic model for the localized high pressure zones based on experimental data from ship-ramming trials in multiyear sea ice on the USCGS Polar Sea and MV Canmar Kigoriak. The loading conditions inside the high pressure zones of the interaction area is multiaxial and the process is very complex. In order to study ice behaviour under such conditions, two medium-scale test programs were carried out on Hobson's Choice Ice Island Research Station by the Ocean Engineering Research Centre of Memorial University of Newfounland, the National Research Council of Canada (NRC), Canadian Cost Guard (CCG) and Sandwell Swan Wooster (SSW) in April, 1989 and May, 1990. To understand the microstructure change of ice and its effect on mechanical behaviour of ice, tests were conducted by Xiao (1991) under unixial conditions and Stone *et al.* (1997), Melanson (1998), Melanson *et al.* (1999), Meglis *et al.* (1999) and most recently by Barrette (2001) with laboratory prepared granular ice and a few ice cores retrieved from icebergs. The data from Barrette (2001) are analyzed to study the phenomena and mechanisms of temperature effect on strain history and failure modes of ice in this research. These tests setup are briefly introduced to describe the experimental conditions and provide a geometrical image for numerical analysis in Chapter 5.

3.2 Medium Scale Indentation Tests

3.2.1 Test Setup

In April, 1989, eleven tests were conducted on Hobson's Choice Ice Island. Three tests used a flat-rigid indentator with speeds varying from to 10 mm/s to 80 mm/s and the other tests used a spherical indentator with speeds ranging from 0.3 mm/s to 90 mm/s. Five indentation tests with flat indentors were performed in May, 1990. The speeds varied form 100 mm/s to 400 mm/s. The insitu temperature of the ice was around –10 to –14 °C. The indentation test system consisted of a hydraulic actuator (some tests in May, 1990 used three actuators) mounted upon a large mobile skid of beam and strut construction, as shown in Figure 3.2. The actuator was controlled by a servo-control system which provided an approximately constant speed, although there were some forward surges during the unloading process. This is because the servo-control valve can not control the rapid movement forward upon the pulverization of the ice. The system was located in a trench 3 m wide, 4 m deep and 100 m long. The walls of the trench were roughly smoothed with a chain saw and the test areas were specially machined with a vertically mounted circular saw. The tests were carried out in an area of 8 m thick multiyear ice which was attached to the edge of the ice island. Pressure sensors were mounted in front of the indentor to measure the local pressures. The ice failure process was recorded with a video camera through a special window (160 × 340 mm) at the center.

3.2.2 Discussion

The results were discussed by Frederking *et al.* (1990a, b), Xiao (1997 for tests of NRC6 and NRC7) and Jordaan (2001). Peak pressures as high as 70 MPa have been shown in the tests on sensors 12.7 mm in the diameter. These high pressures result in the formation of a damage layer of ice in the contact zone. Both large spalls and local crushing under the indentor face typically accompanied the indentation tests. Low speed tests allowed sufficient time for a creep deformation and microcracks to extend into the ice, and the load history curve is relatively smooth. High speed tests showed relatively brittle behaviour and dynamic ice forces on the indentors are recorded. Analyses of damaged layer profiles showed that the layer thickness was irregular. The thickness of the damaged layer was typically 20 mm to 50 mm and a maximum value of 320 mm was observed in test NRC5.

A section through the impacted surface of one test in 1989, as shown in Figure 3.3, was studied by Muggeridge and Jordaan (1999) and Jordaan (2001). A pronounced boundary some distance away from the center contact zone is shown between the damaged ice and the parent ice in Figure 3.3. Lateral motion of grains along the boundary was also observed. Spalls and damaged ice with extensive microfracturing are in evidence in the outer areas, with a bluish interior. This is because at the edge, the lower confinement and high shear will nucleate microcracks. The blue zone in the central region contains a mixture of fine grains and parent-sized grains and extends some way into the ice. Severe grain modification, primarily recrystallization due to the high confinement pressure, was the major feature of this zone. The thickness varies along the

layer and near the center may be merely a damaged zone without a clear boundary. This is because the lateral deformation contributing to the extrusion is minimal (Jordaan, 2001).

Jordaan (2001) proposed a model, as shown in Figure 3.4, to estimate the behaviour of a high-pressure zone during the cycling of load. In his model, damage first forms near the edge of the high-pressure zone. Nucleation of microcracks occurs across the basal planes, at points of stress concentration, accompanied by extensive recrystallization. This results in extensive microfracturing near the edges, with the formation of a white zone containing cracks and air pockets. The coalescence of the microcracks finally results in fragmentation of the material near the edges of the zone. Because of the high confining pressure, the centre of the high-pressure zone exhibits pressure softening as a result of the fine-grained material in the recrystallization process. In the cyclic behaviour, the pressure softening process which occurs towards the peak loads, reverses itself when the pressure drops.

3.3 Triaxial Ice Tests in Laboratory

3.3.1 Test Setup

The tests were conducted using laboratory prepared granular ice and a few specimens retrieved from the field. A cylindrical geometry was used for all specimens. The cylinders were 155 mm high and 70 mm in diameter. Samples were allowed to equilibrate for at least 12 hours at the temperature of interest prior to being tested. Testing

was performed using a MTS test frame (Figure 3.5) fitted with a Structural Behaviour Engineering Laboratories Model 10 Triaxial Cell. The MTS system consisted of two servo-controlled hydraulic rams that applied axial load and confining pressure independently.

A prepared sample was mounted on hardened steel end platens of the same diameter and the assembly was then enclosed in a latex jacket to keep the confining medium (silicone oil) from penetrating the ice. The specimen assembly was placed inside the triaxial cell and, in the tests at low strain levels, two linear variable differential transformers (LVDTs) were clamped to the sides of the jacketed specimen. In these tests, the LVDTs were used to monitor axial displacement and to control the advance rate of the ram. For tests at high strain levels, large sample distortions prevented the use of LVDTs. In these tests, the displacement of the ram was used to control the ram advance rate directly. The confining cell was closed and filled with silicone oil, and a small axial load was applied at ambient pressure to ensure contact between the specimen and piston. The confining pressure was then increased at 0.5 MPa per second to the target confinement, and then the specified axial deformation or creep load was applied to the sample. The parameters recorded during the tests included platen displacement, axial load, confining pressure and temperature.

At the end of each test the axial load was quickly removed and the confining pressure was released gradually. The sample was removed from the cell immediately after testing and inspected for jacket leaks and large scale fractures. When immediate thin

sectioning was not possible, samples were stored at -30°C to restrict grain growth and other microstructural change until thin sections could be prepared and photographed. Temperature was monitored during some tests using an RTD sensor within the confining vessel. However, the RTD was not consistently reliable, particularly for tests at high confinement levels. Therefore in nearly all these tests a consistent starting temperature of the cold room, the ice and the confining fluid was maintained at the temperature of interest.

3.3.2 Test Results and Discussion

Meglis *et al.* (1999) studied the effects of varying deviatoric stress for a selected confining pressure. The selected confining pressures were 20 MPa and 55 MPa while the deviatoric stesses varied from 2 MPa to 20 MPa. It has been observed for both pressures that by increasing the deviatoric stress, the creep strain and strain rate were enhanced significantly. In the tests at high deviatoric stress levels such as 20 MPa, ice showed nearly brittle behaviour. Using a similar method, the effects of different confining pressures under constant deviatoric stress conditions were studied by Meglis *et al.* (1999). The study showed that creep strain and strain rate were also accelerated under low and high pressure levels. The acceleration of the strain and strain rate was believed to be caused by the damage enhancement. Damage analysis is described in detail in Chapter 4.

In this study, the analysis of recent experimental data obtained from Barrette (2001) has been conducted to study the temperature effect, failure modes and relevant mechanisms. A strong temperature effect on the creep behaviour of ice was observed

with a given confining pressure and deviatoric stress. Two groups of tests are analyzed here. The first was done at a deviatoric stress s = 15 MPa and the confining pressure P_c = 10 MPa with the temperature varying from –7 °C to –27 °C. The second was conducted at a deviatoric stress of stress s = 15 MPa and confining pressure P_c = 65 MPa with the temperature varying from –8.5 °C to –25 °C. Figures 3.6 and 3.7 demonstrate the effects of the temperature on the creep strains and strain rates for the two cases, respectively. It can be seen that an increased temperature results in softening of the ice so that the strains and strain rates of ice are enhanced significantly.

In the triaxial tests, two main types of mechanical behaviour were observed. The first is a ductile behaviour as shown in curve C of Figure 3.8. The creep rate increased rapidly from a minimum value, dependent on the confining pressures, and then increased much more slowly with a steady state deformation. The second is a semi-brittle behaviour as shown in curve C′ of Figure 3.8. The creep rate increased also from a minimum value without stabilizing. This is termed "runaway" strain behaviour in this research. This runaway behaviour is assumed to be related to the failure of the ice spemimens. Schematic representations of the macroscopic shapes of typical deformed samples are shown in Figure 3.9. Samples that deformed without rupture showed axial shortening and lateral expansion which was relatively uniform along the length of the sample (Figure 3.9a). Three types of failure (shear strain localization, rupture and splitting), can be roughly identified from the tests as demonstrated in Figure 3.9b, c and d, respectively. Figure 3.10 shows the pressure-temperature relationship of all the tests that have shown a runaway behaviour. Both laboratory ice and iceberg ice specimens were studied. Figure

3.11 shows the pressure-temperature relationship of all the tests which resulted in specimen failure. By checking the final shape of the specimens showing runaway behaviour, these specimens also showed a failure. However, one out of sixteen failed specimens did not show the runaway behaviour. The failure type of this specimen is shear strain localization. From Figure 3.11 it can be simply obtained that the runaway tends to occur at low and high confining pressures for lab ice and no evidence of runaway was found at medium pressure levels among the tests of laboratory ice. Most of the runaway results for tests of laboratory ice occurred at relatively high temperature (higher than –10 °C) and only one test was found to have a runaway behaviour at temperature equal to –21 °C and P_c = 10 MPa with an initial flaw. The runaway behaviour for tests of iceberg ice was relatively less dependent on the confining pressure and temperature. However, the tests did show that most of the runaway strains for iceberg ice specimens occurred at low and high pressures except two tests with a runaway observed at confining pressure equal to 30 MPa. Initial flaws such as cracks,veins and brine pockets, etc., were observed in all the iceberg ice specimens before the tests.

Figure 3.11 shows that at a low pressure level (10 MPa), rupture is the only type of failure observed for both laboratory ice specimens and iceberg ice specimens. At medium pressure, two failed iceberg specimens were observed. One showed rupture at relatively low temperature of –5 °C and another showed a band of strain localization at –26 °C. At relatively high pressure levels (more than 50 MPa), both rupture and shear strain localization were observed and one iceberg ice specimen failed by splitting. An initial vein in the axial direction before the test was observed in the specimen that failed by

splitting. All the ruptured planes and strain localized bands of the specimens were oriented approximately at 45 °.

In summary, for laboratory ice, the failure of ice specimens occurred at low and high pressures and for iceberg ice specimens, failure is relatively less dependent on confining pressure. The failure of iceberg ice specimens is suspected to be induced by the initial flaws. By checking the microstructure of failed specimens with thin sections, along the faulted plane at low pressure levels (10 MPa), a local dense concentration of highly aligned microcracks accompanying some fine-grained ice were observed (Meglis *et al.*, 1999). However, at medium and high pressure levels (more than 30 MPa) fine-grained ice was observed (microcracks are negliblible) along the faulted plane or inside the band of shear strain localization (see Figure 3.12). This evidence suggests that the rupture at low pressure is mainly induced by the nucleation and growth of microcracks along with the dynamic recrystallization and by dynamic recrystallization and pressure melting mechanisms at high pressure levels. Some evidence shows that rupture might be associated with strain localization. There were two tests at pressures of 50 MPa and 65 MPa that showed a band of strain localization which is nearly ruptured. This evidence supports the explanation that the rupture starts from a strain localization band and a rupture will occur along the band when the damage evolution inside the band goes to a certain level. Shear fracture without a significant lateral deformation was observed by Meglis *et al.* (1999) at increased deviatoric stresses (30 MPa). This may be attributed to brittle behaviour induced by the drastic enhancement of the strain rate at the increased stresses so that not enough lateral deformation can be developed before the fracture.

From the study of runaway behaviour and failure of ice specimens, it may be concluded that under triaxial conditions at confining pressures larger than 5 MPa, the ice specimens fail mainly by the rupture starting with strain localization. Runaway and failure of intact ice tend to occur at low and high confining pressures with relatively high temperature (higher than –10 °C). It is also believed that rupture can ccur if the pressure and deviatoric stress reach a certain level. Runaway behaviour can be induced by rupture. Runaway behaviour can also be induced by a certain level of strain localization, but strain localization doesn't necessarily induce runaway behaviour. For the ice with significant initial flaws such as iceberg ice, rupture and runaway behaviour may be triggered by these flaws. A numerical study of mechanism of strain localization is described in details in Chapter 5.

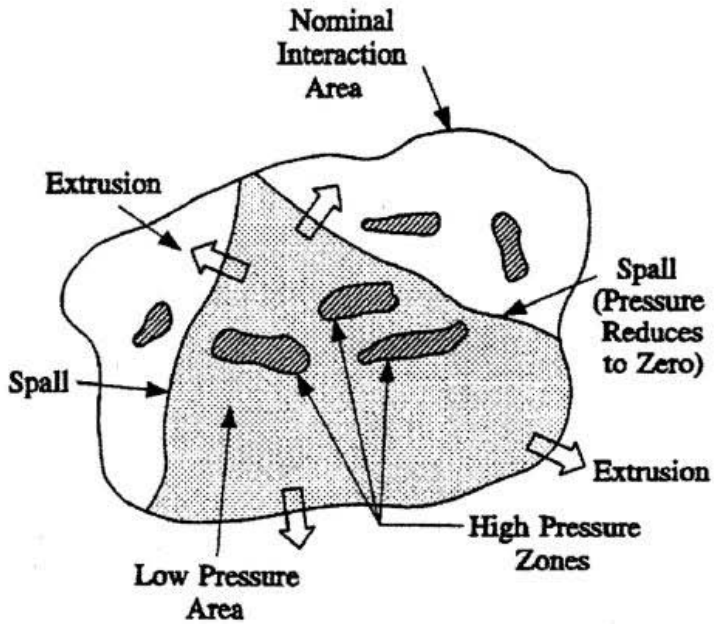

Figure 3.1 Nominal interaction area and contributing components (Jordaan, 2001).

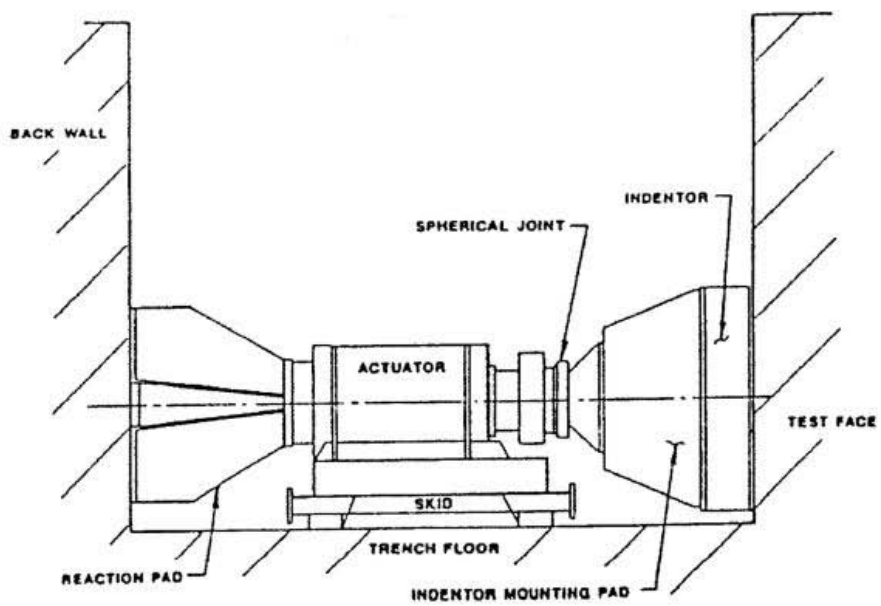

Figure 3.2 Schematic of the actuator indentor system (Frederking *et al.* 1990a)

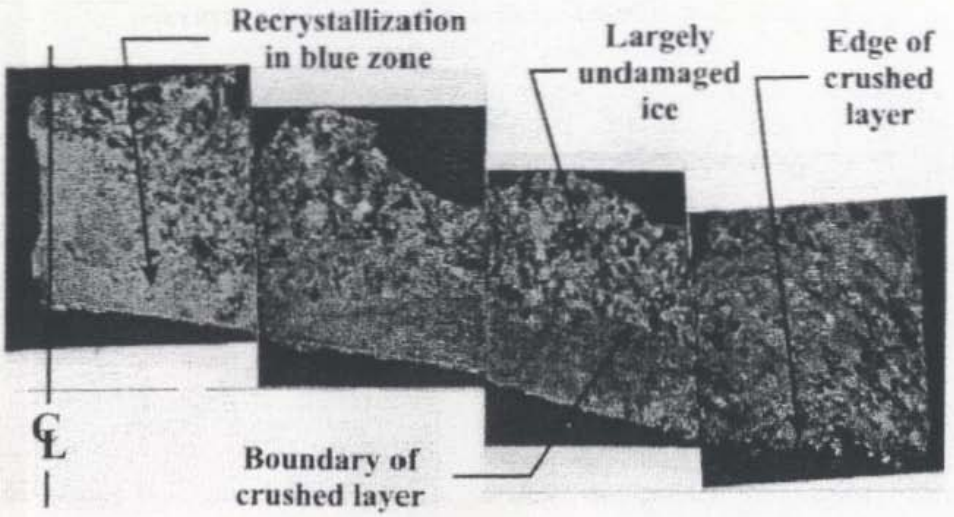

(a)

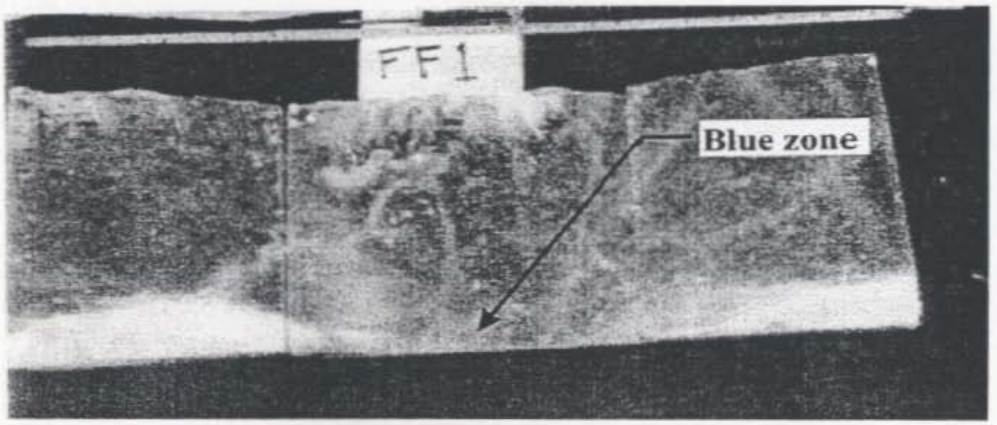

(b)

Figure 3.3 Thin section of the contact zone of ice and the indentor; (a) Hobson's Choice 1989, test NRC 05; (b) Hobson's Choice 1990, test TFF-01. (Jordaan, 2001)

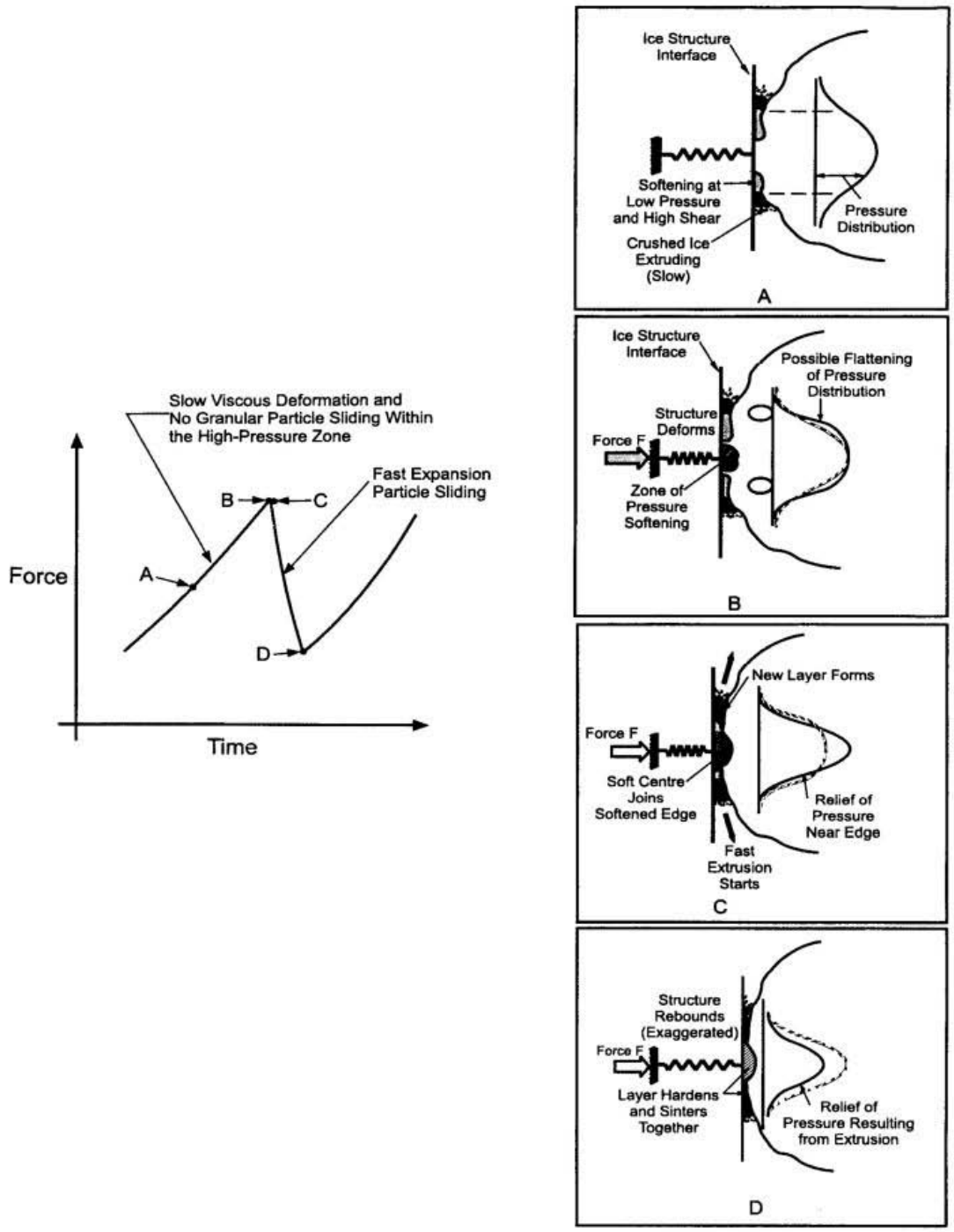

Figure 3.4 Demonstration of the load fluctuation and processes in a high-pressure zone (Jordaan, 2001)

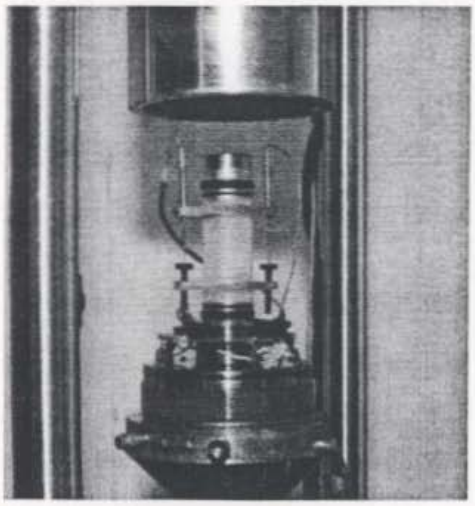

Figure 3.5 View of the triaxial cell with a specimen prepared for testing

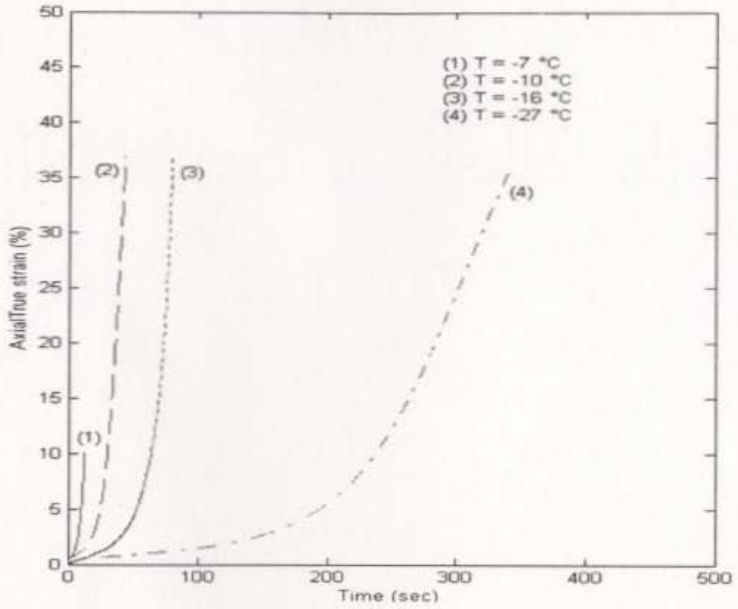

Figure 3.6a Strain history for s = 15 MPa and P = 10 MPa

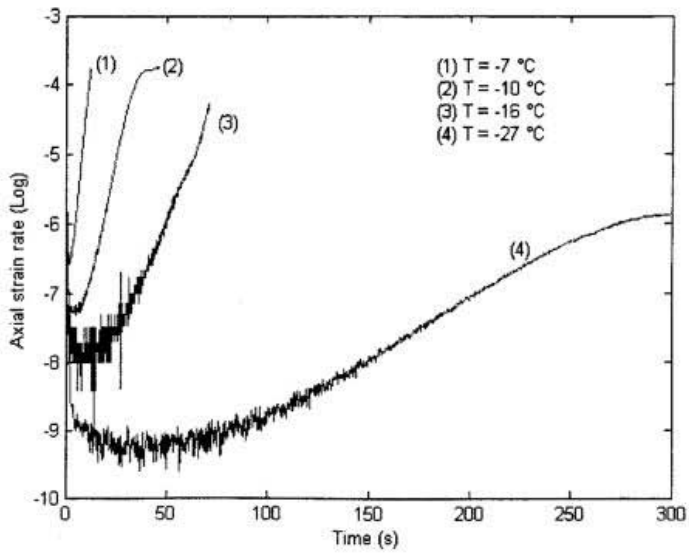

Figure 3.6b Strain rate (logarithm) history for s = 15 MPa and P =10 MPa

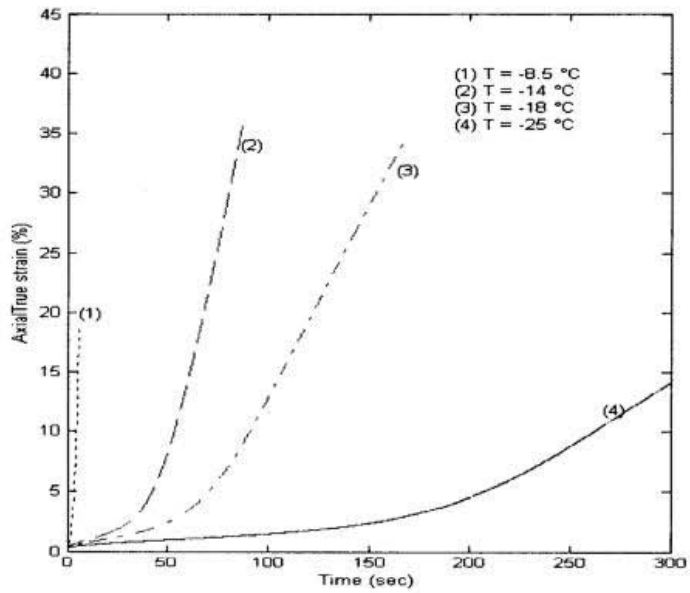

Figure 3.7a Strain history for s = 15 MPa and P = 65 MPa

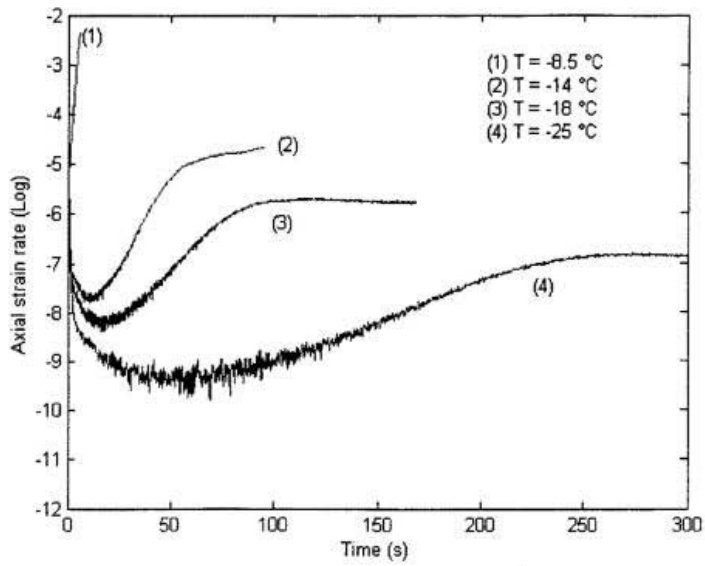

Figure 3.7b Strain rate (logarithm) history for s = 15 MPa and P = 65 MPa

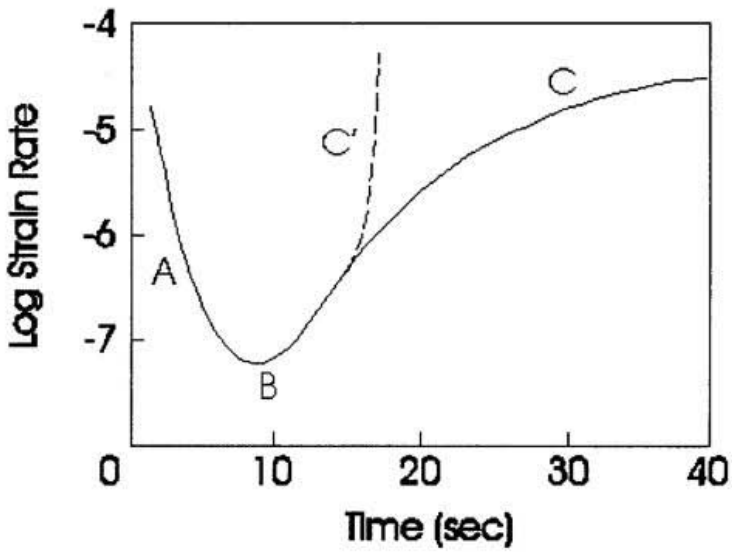

Figure 3.8 Illustration of strain rate history of ice. A: Decelerating creep; B: Minimum creep rate; C: Accelerating creep; C': Run-away behaviour.

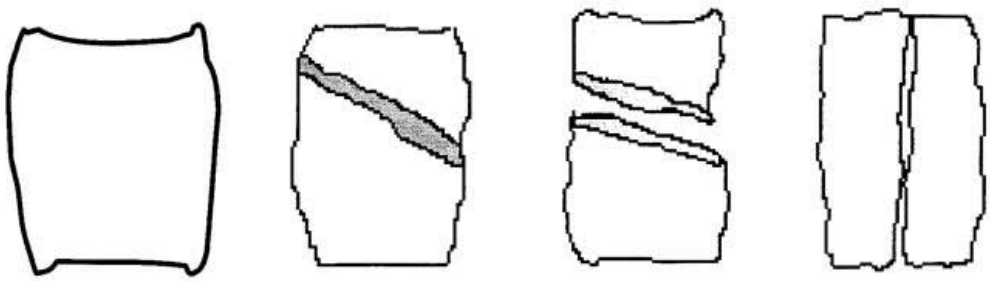

(a) (b) (c) (d)

Figure 3.9 Schematic represents of macroscopic shape of deformed samples after tests. (a) most samples deformed relatively uniformly; (b) strain localization; (c) rupture; (d) axial splitting

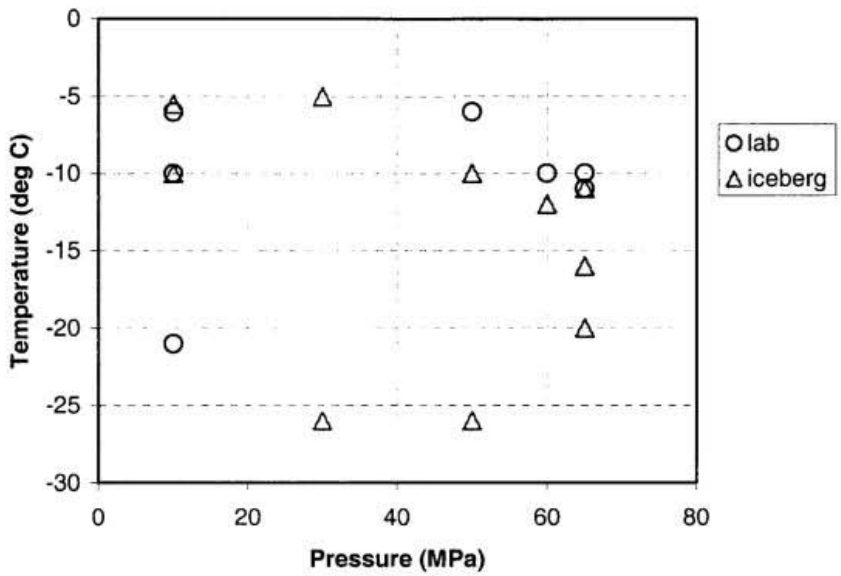

Figure 3.10 P – T relationship for specimens showing runaway behaviour

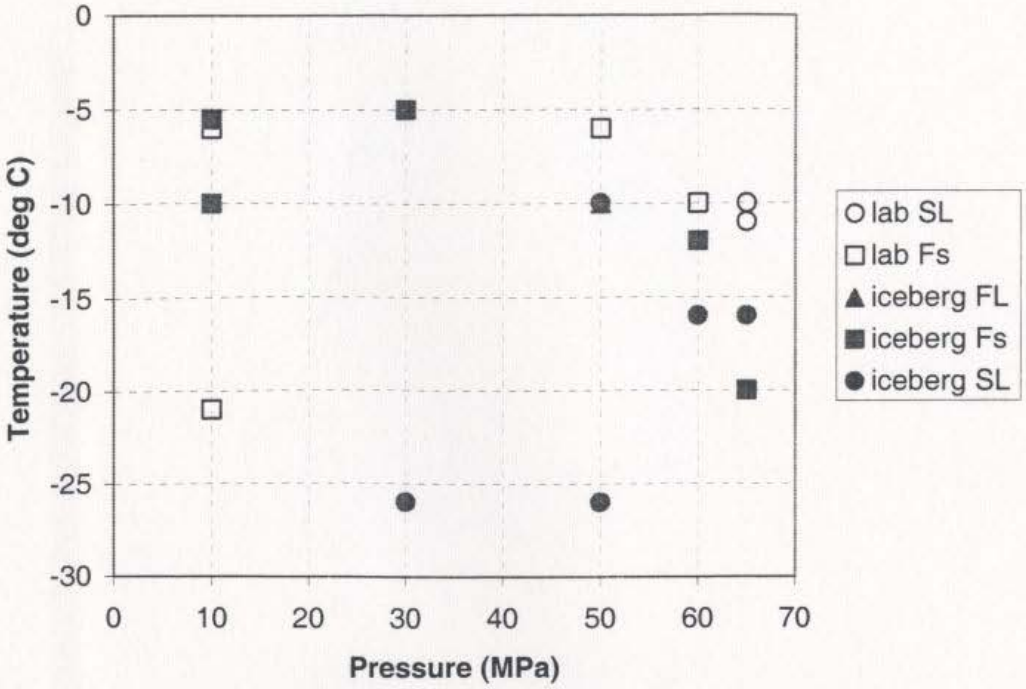

Figure 3.11 P – T relationship for specimens showing different types of failure: SL, Fs and FL represent strain localization, shear fracture and axial splitting, respectively.

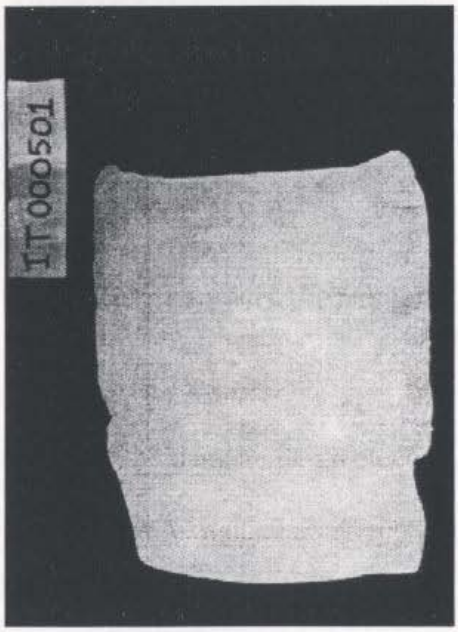

(a)

(b)

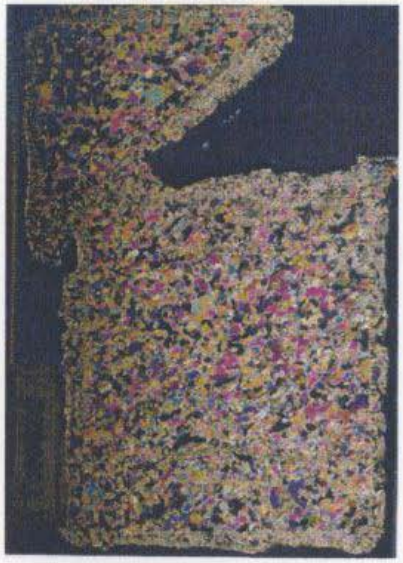

(c)

Figure 3.12 Photographs of samples show strain localization or rupture. (a) Profile for test IT 000501 showing localized bands at deviatoric stress =15 MPa and confining pressure = 50 Mpa; (b) Thin section for IT 000501 showing fine grains concentrated inside the localized bands; (c) Thin section for IT 000505 (deviatoric stress = 15 MPa, confining pressure = 30 MPa) showing fine grains along the faulted plane.

Chapter 4

Constitutive Model for Finite Element Analysis and Parametric Calibration

4.1 Derivation of Constitutive Model

4.1.1 Total Strain and Its Components at Triaxial Loading Conditions

Under triaxial loading conditions, both the delayed elastic strain and viscous creep strain can be expressed in terms of a deviatoric strain component e_{ij} and a volumetric strain component ε_v, i.e.,

$$\varepsilon_{ij}^{d} = e_{ij}^{d} + \varepsilon_{v}^{d} \text{ and} \tag{4.1}$$

$$\varepsilon_{ij}^{c} = e_{ij}^{c} + \varepsilon_{v}^{c} \ . \tag{4.2}$$

Combining the volumetric strain components in Eq.(4.1) and Eq.(4.2), the total strain and strain rate of ice at triaxial loading conditions can be expressed as

$$\varepsilon_{ij} = \varepsilon_{ij}^{e} + e_{ij}^{d} + e_{ij}^{c} + \varepsilon_{ij}^{v}\delta_{ij} \tag{4.3}$$

$$\dot{\varepsilon}_{ij} = \dot{\varepsilon}_{ij}^{e} + \dot{e}_{ij}^{d} + \dot{e}_{ij}^{c} + \dot{\varepsilon}_{ij}^{v}\delta_{ij}, \tag{4.4}$$

where ε_{ij}^{e} represents the elastic strain; e_{ij}^{d} is the deviatoric delayed elastic strain tensor; e_{ij}^{c} is the deviatoric viscous strain tensor; ε_{ij}^{v} is the volumetric strain tensor and δ_{ij} is the delta function.

Under triaxial conditions, for the equivalent delayed elastic strain tensor and equivalent viscous strain tensor the von Mises stress should be used instead of the normal stress. According to Eq.(2.44), the equivalent delayed elastic and viscous elastic strain rates have been derived by Xiao (1991) and Singh (1993) as follows:

$$\dot{e}_{ij}^{d} = \frac{3}{2}\dot{\varepsilon}_{0}^{d}\left(\frac{s^{d}}{\sigma_{0}}\right)^{n}\frac{s_{ij}}{s}\exp(\beta_{d}S) \quad \text{and}$$

$$\dot{e}_{ij}^{c} = \frac{3}{2}\dot{\varepsilon}_{0}^{c}\left(\frac{s}{\sigma_{0}}\right)^{n}\frac{s_{ij}}{s}\exp(\beta_{c}S), \tag{4.5}$$

where $\dot{\varepsilon}_{0}^{d}$ and $\dot{\varepsilon}_{0}^{c}$ are the reference strain rate; s is von Mises stress; s_{ij} is the deviatoric stress tensor; β_{d} and β_{c} are the damage enhancement factors mentioned in Section 2.4.3 and s^{d} is the effective stress in the dashpot of the Kelvin unit which can be expressed as

$$s^{d} = s - E_{K}e^{d}, \tag{4.6}$$

where E_K is the Young's modulus of the spring in the Kelvin unit and e^{d} is the equivalent delayed elastic strain.

The volumetric strain can be obtained by the study of dilatation of ice. The density of ice in the crushed layer adjacent to the indentor was observed to be less than that of

parent ice in Hobson Choice island ice tests (Frederking *et al.* 1990a, b). This indicated the dilatation of ice during the interaction process. The dilatation of ice may be caused by the microcracking. Dilatation of ice was measured in small-scale constant strain rate tests by Wang (1981) and Dorris (1989). Recently, at Memorial University of Newfoundland dilatation of ice has been studied at small-scale constant stress tests by Singh (1993), Stone *et al.* (1997) and Xiao and Jordaan (1996) on intact and damaged ice under triaxial compressive loading conditions. The dilatation (volumetric strain) can be determined by two methods: (1) measuring the diametral expansion of the sample in two orthogonal directions with three specially designed strain gauges at the central portion of the sample. (2) measuring the fluid volume change within the confining cell. An empirical equation for volumetric strain was proposed by Singh (1993) at triaxial compressive loading conditions as follows:

$$\dot{\varepsilon}_v = -\frac{f_3}{p}(\dot{e} - \dot{e}^e) = -\frac{f_3}{p}(\dot{e}_{ij}^d + \dot{e}_{ij}^c), \tag{4.7}$$

where f_3 is a constant; p is hydrostatic pressure; e is the equivalent total strain under triaxial loading conditions and e^e is the equivalent elastic strain.

4.1.2 Constitutive Model for Finite Element Application

For viscoelastic materials, the stress tensor can be described as follows:

$$\sigma_{ij} = K_{ijkl}(\varepsilon_{ij} - \varepsilon_{ij}^i) = K_{ijkl}\varepsilon_{kl}^e \quad , \tag{4.8}$$

where $\varepsilon_{ij}^i = e_{ij}^d + e_{ij}^c + \varepsilon_{ij}^v \delta_{ij}$ is the total inelastic strain tensor and the isotropic modulus matrix:

$$K_{ijkl} = (K - \frac{3}{2}G)\delta_{ij}\delta_{kl} + G(\delta_{ik}\delta_{jl} + \delta_{il}\delta_{jk}), \tag{4.9}$$

where K is bulk modulus and G is shear modulus.

Following Eq.(4.8), the increment of stress tensor is

$$\delta\sigma_{ij} = K_{ijkl}\delta\varepsilon^{e}_{kl} + \delta K_{ijkl}\varepsilon^{e}_{ij}. \tag{4.10}$$

Thus, the stress at time $t + \Delta t$ can be described as

$$\sigma_{ij}^{t+\Delta t} = \sigma_{ij}^{t} + \delta\sigma_{ij}. \tag{4.11}$$

The stiffness matrix in Eq.(4.10) can be obtained using Eq. (4.9) and the shear modulus and Young's modulus are given by Eq. (2.24) as follows:

$E = E_0(1 + C_1 S)^{-1}$ and

$$G = G_0(1 + C_2 S)^{-1}, \tag{4.12}$$

where the damage parameter S follows the expression described by Eq. (2.50). Then, the bulk modulus can be derived from Young's modulus and shear modulus.

The decrement in elastic moduli can be obtained by calculating the difference between the elastic moduli at current and previous state, i.e.,

$\delta E = E' - E$ and

$$\delta G = G' - G, \tag{4.13}$$

where E' and G' represent the elastic moduli of the current state which can be expressed as

$E' = E_0[1 + C_1(S + \delta S)]^{-1}$ and

$$G' = G_0[1 + C_2(S + \delta S)]^{-1}. \tag{4.14}$$

The damage, S, in Eq. (4.14) is given by Eq.(2.50) and the increment of the damage parameter, δS, can be expressed as

$$\delta S = [f_1(p)(\frac{s}{s_0})^q + f_2(p)\exp(\frac{s}{s_0})]dt . \tag{4.15}$$

Substituting Eq.(4.13) into Eq.(4.9), the increment of the stiffness matrix, δK_{ij}, in Eq.(4.10) can be obtained.

According to Eq. (4.3) and Eq.(4.4), the increment of the elastic strain component, $\delta\varepsilon_{ij}^e$, can be calculated by

$$\delta\varepsilon_{ij}^e = \delta\varepsilon_{ij} - \delta e_{ij}^d - \delta e_{ij}^c - \delta\varepsilon_{ij}^v\delta_{ij}, \tag{4.16}$$

where the increment of the total strain, $\delta\varepsilon_{ij}$, is a variable which can be automatically given by ABAQUS with iteration. The increments of equivalent delayed elastic strain, viscous strain and volumetric strain components ($\delta\varepsilon_{ij}^d$, δe_{ij}^c and $\delta\varepsilon_{ij}^v$), can be calculated respectively by the following equations:

$$\delta e_{ij}^d = \frac{3}{2}\dot{\varepsilon}_0^d\left(\frac{s^d}{\sigma_0}\right)^n\frac{s_{ij}}{s}\exp(\beta_d S)\delta t \quad , \tag{4.17}$$

$$\delta e_{ij}^c = \frac{3}{2}\dot{\varepsilon}_0^c\left(\frac{s}{\sigma_0}\right)^n\frac{s_{ij}}{s}\exp(\beta_c S)\delta t , \quad \text{and} \tag{4.18}$$

$$\delta\varepsilon_v = -\frac{f_3}{p}(\dot{e}_{ij}^d + \dot{e}_{ij}^c)\delta t \tag{4.19}$$

This process of the derivation of the constitutive model was modified from a user material subroutine (UMAT) of ABAQUS using FORTRAN code by Xiao (1997) The

stress, delayed elastic strain, viscous strain and damage are all stored as state variables from previous steps; at the end of each increment, they will be updated.

4.2 Calibration for Damage Parameter

The creep response of ice specimens deformed in the laboratory has been analyzed to determine parameters in damage analyses. This analysis has been done for very high strain levels (up to 35%). A nominal constant stress of 15 MPa was applied to all the specimens. The proposed damage model has been calibrated from the data collected during these tests.

At high strains, from a damage mechanics point of view, the Burgers body can be reduced to a single dashpot. The spring in the Kelvin unit for the delayed elastic strain and the spring in the Maxwell unit for elastic strain are neglected. This breakdown of the Burgers body serves to reduce the complexity of the calibration significantly. In the other words, we can use the steady strain rate from the experimental data for calibrating the damage parameter.

4.2.1 Derivation of The Calibration Model for Damage Parameter

Based on the approximation for large deformation of ice described above, a model can be established for calibrating of the damage parameters. As proposed by Xiao (1997), the constitutive model for triaxial tests with damage effects can be expressed as:

$$\dot{\varepsilon} = c(\frac{S}{S_0})^n \exp(S), \tag{4.20}$$

where c and n are constants; s_0 is a reference stress; s is von Mises stress and S is damage parameter as expressed below:

$$S = \int_0^t f(p)(\frac{s}{s_0})^q dt, \tag{4.21}$$

where q is a constant, $f(p)$ is a general function of hydrostatic pressure which can lead to either a reduction in the creep rate by suppression of tensile zones at the tips of microcracks, or to an increase in the creep rate by pressure softening.

For constant stress tests, the damage parameter is only dependent on time, Eq.(4.21) becomes:

$$S = f(p)(\frac{s}{s_0})^q t. \tag{4.22}$$

Substituting Eq.(4.22) in Eq.(4.20) and taking the natural logarithm of both sides yields:

$$\ln(\dot{\varepsilon}) = \frac{f(p)}{s_0^q} s^q t + n\ln(\frac{s}{s_0}) + \ln(c). \tag{4.23}$$

Eq.(4.23) shows that the natural logarithm of the strain rate is approximately linear with time for the special case of constant stress. This can be simplified as:

$$\ln(\dot{\varepsilon}) = \phi t + I, \tag{4.24}$$

where the slope, ϕ, is equal to the damage rate (dS/dt) according to Eq.(4.23) and the intercept, I, is expressed as:

$$I = n\ln(\frac{s}{s_0}) + \ln(c). \tag{4.25}$$

Using Eq.(4.24), with a stress and a strain rate correction to the collected data, a model can be established for constant stress conditions with various pressures.

4.2.2 Stress and Strain Rate Corrections to The Experimental Data

A significant increase in cross sectional area of the samples by lateral strain was observed when specimens deformed to a high strain levels. Because the MTS test system maintained a constant load instead of a constant stress, a stress correction needed to be applied when plotting and analyzing the data. As a result, the calculated strain rates also required a correction to approximate the constant stress conditions.

Two assumptions were made to simplify the problem for data correction (Melanson, 1998). The first is that the specimens are assumed to deform uniformly along the entire length. The second is to assume that the specimens maintain a constant volume during the tests. Based on the power law dependence of creep rate on stress, the following equations can be applied:

$$\dot{\varepsilon}_e = k s_e^n \tag{4.26}$$

$$\dot{\varepsilon}_{cs} = k s_{cs}^n, \tag{4.27}$$

where the subscripts e and cs represent experimental data and data corrected for constant stress respectively. Since k is a material constant, Eq.(4.26) and (4.27) may be combined to give:

$$\dot{\varepsilon}_{cs} = \dot{\varepsilon}_e \left(\frac{s_{cs}}{s_e}\right)^n. \tag{4.28}$$

In this equation, we know $\dot{\varepsilon}_e$ and s_e (determined from the uniform deformation assumption) and s_{cs} (15 MPa). The power law dependence n was obtained from a plot of the logarithm of true stress versus the logarithm of strain rate (Figure 4.1) for strain levels of 5%, 10%, 20%, 30%, 40% and 44%, respectively. By taking the natural logarithm of each side of Eq.(4.26), the slope of each line in Figure 4.1 is the stress dependence n. It can be seen that best fit lines show a trend of power law dependence. Also, from Figure 4.1, the exponent n seems to increase slightly with increasing strain levels. The mean value of the slopes, 4.2, has been used. The standard deviation is 0.4.

The first calibration neglects the damage enhancement factor for strain rate. This enhancement is small for small strain levels, but becomes significant for large strain levels. To include the damage effects, a second calibration is needed after the initial calibration of the damage was performed based on the data after first correction.

Similar to the first correction as described by Eq.(4.28), the second correction can be performed based on the equation expressed below:

$$\dot{\varepsilon}_{cs} = \dot{\varepsilon}_e \left(\frac{S_{cs}}{S_e}\right)^n \exp(S_{cs} - S_e), \tag{4.29}$$

where $n = 4.2$; and S_{cs} and S_e are damage parameter for the constant stress conditions and experimental data respectively. S_{cs} and S_e are calculated based on Eq.(4.21), and the hydrostatic pressure is calculated as: $p = p_c + \frac{s}{3}$.

The following summarizes the procedures used in the calibration process:

1. Collect data and correct the stress based on the assumption of a constant volume of specimens .
2. Correct the strain rate based on corrected stress using Eq.(4.28).
3. Eq.(4.23) is used to develop the initial damage parameter with the strain rate from step 2 and to find the initial function of *f(p)* in Eq.(4.21).
4. With the initial *f(p)*, Eq.(4.28) is used to provide a second correction of the strain rate.
5. With the data from step 4 a final damage parameter can be obtained using Eq.(4.23); thus, *f(p)* is final calibrated.

4.2.3 Formulation of Damage Calibration

The formulation for the damage parameter used in this study is based on the model proposed by Xiao and Jordaan (1996) which is different from the power law model by Melanson (1998). The formulation can be expressed as follows:

$$S = \int_0^t [f(p)(\frac{s}{s_0})^q + f_2(p)\exp(\frac{s}{s_0})]dt \qquad (4.30)$$

where,

$$f_1(p) = a_1(1-\frac{p}{p_1})^2 \quad \text{when } p \le p_{tr}$$

and

$$f_2(p) = a_2(\frac{p}{p_2})^r$$

where a_1, a_2, p_1, p_2, r and q are constants; p_{tr} is a transition pressure at which damage by microcracking is highly restricted and approaches zero; the stress s_0 is a reference value.

Following the procedures outlined above, the damage rate at different pressures has been obtained from the original test data by using Eq. (4.24) with corrected stresses and strain rate. Temperature corrections have been made in the present study, since temperature varied from –5 °C to -27 °C in these tests. Apart from the calibration for pressure, the stress calibration has also been done in this study. This process is performed by a Matlab program. An example giving a comparison of the logarithm of strain rate versus time before and after the first correction and after the second correction is plotted in Figure 4.2.

4.2.4 The First Calibration for Pressure

Figure 4.3 shows the values of damage rate (ϕ) computed for all tests at various pressures. The data points at a pressure of 10 MPa are retrieved from the tests by Melanson (1998). The data in Figure 4.3 include results were obtained at different temperatures. Since the data were collected at different temperatures, it would be beneficial to reduce the values to a single nominal temperature, namely –10 °C in this research. At a given pressure, the damage rate is assumed to be related with temperature as given below:

$$\frac{dS}{dt} = [f_1(p)(\frac{s}{s_0})^q + f_2(p)\exp(\frac{s}{s_0})]\exp(-\frac{Q}{RT}), \tag{4.31}$$

where Q is activation energy, R is Boltzman's constant and T is temperature in Kelvin degree.

Verification of the assumption in Eq.(4.31) can be obtained by taking natural logarithm of data in Figure 4.3 and plotting the resulting values against the inverse temperature. The relationship between $\ln(\phi)$ and $1/T$ is plotted in Figure 4.4a, 4.4b, 4.4c, 4.4d and 4.4e for different pressures. Regression lines and the corresponding equations are also shown in these figures. Then the temperature correction can be made by taking the intercept of $\ln(\phi)$ at $1/T = 0.0038$ which is referred to –10 °C. The damage rate ϕ can be obtained for temperature at –10 °C. Figures 4a to 4e provide empirical evidence for the validity of Eq.(4.31). The damage-pressure relationship at -10°C including the temperature correction is plotted is Figure 4.5.

Figure 4.5 shows the values of the damage rate (ϕ) computed for all tests at various pressures with a constant stress of 15 MPa. The data show a minimum value in the 40 – 50 MPa region. This minimum will serve as the point of inflection or transition point (p_{tr}), where two separate functions described in Eq.(4.30), defining the relation on either side, will meet and overlap. The first part is within the low pressure zone which undergoes microfracturing and shear banding, accompanied by dynamic recrystallization. The second part appears at high pressures and is characterized by possible pressure melting, grain boundary migration, and more intense recrystallisation. Since there is no clear boundary between the two zones, the model parameters were developed to overlap

the ranges, eventually reaching zero as the functions pass the transition pressure. This is shown in Figure 4.6 as both functions are plotted separately.

The first part of the curve was approximated by using a parabolic function up to the transition pressure:

$$f_1(p) = 0.6(1-\frac{p}{50})^2 \quad \text{when } p \le 50 \text{ MPa}$$

and

$$f_1(p) = 0 \qquad \text{if } p > 50 \text{ Mpa} \tag{4.32}$$

The second part of the curve was expressed by a power law function:

$$f_2(p) = 0.10(\frac{p}{50})^5 \tag{4.33}$$

4.2.5 The Second Calibration for Pressure

The procedure for the second calibration is similar to the first calibration presented in Section 4.2.4. The data points for damage rate including the second correction based on Eq.(4.29) without the temperature correction are plotted against pressure in Figure 4.7. The relationship between $\ln(\phi)$ and $1/T$ is plotted in Figure 4.8a, 4.8b, 4.8c, 4.8d and 4.8e for different pressures. Regression lines and the corresponding equations are included in the figures. The damage-pressure relationship at –10 °C, after the temperature correction, is plotted in Figure 4.9. A temperature correction is made as similar as discussed in Section 4.2.4. The calibrated curve fitted to the data is also shown in Figure 4.9. The resulting parameters were determined to be as follows:

$$f_1(p) = 0.7(1-\frac{p}{50})^2 \quad \text{when } p \le 50\,\text{MPa}$$

and

$$f_1(p) = 0 \qquad \text{if } p > 50\,\text{MPa} \tag{4.34}$$

The second part of the curve was expressed as a power law function:

$$f_2(p) = 0.12(\frac{p}{50})^6 \tag{4.35}$$

4.2.6 Stress Calibration

Two sets of experiment data retrieved from Meglis *et al.* (1999) were used to calibrate the q and s_0 in Eq.(4.30). The first is a set of data with various stresses at pressure = 10 MPa. The second is a set of data with various stresses at pressure = 55 MPa. Since at low pressure levels, especially when pressure is around 10 MPa (see Figure 9), damage is mainly caused by microcracks so that the second component in Eq.(4.30) can be neglected. Therefore, under constant stress conditions, Eq.(4.30) can be simplified:

$$\phi = \frac{dS}{dt} = f_1(p)(\frac{s}{s_0})^q \tag{4.36}$$

Similarly, for pressure equal to 55 MPa, the first component of Eq.(4.30) can be neglected and under constant stress conditions, it can be simplified to:

$$\phi = \frac{dS}{dt} = f_2(p)\exp(\frac{s}{s_0}) \tag{4.37}$$

First, Eq.(4.37) is used to calibrate the reference effective stress s_0. By taking the natural logarithm of both sides of Eq.(4.37), the following can be obtained:

$$\ln(\phi) = \ln(f_2(p)) + \frac{s}{s_0}. \tag{4.38}$$

Since pressure is constant during the whole test, $f_2(p)$ is constant and the slope of Eq.(4.38) will be $1/s_0$. Following the similar procedures as described in Section 4.2.4, we can obtain a plot of $\ln(\phi)$ versus s as shown in Figure 4.10. The value for s_0 = 15 MPa can be obtained by take the inversion of the slope of the regression line.

Once s_0 is determined, Eq.(4.36) can be used to calibrate q by taking logarithm to the base 10 on both sides:

$$\log(\phi) = \log(f_1(p)) + q\log(\frac{s}{s_0}). \tag{4.39}$$

Therefore, q is the slope of Eq.(4.39). Again, following the similar procedures as described in Section 4.2.4 and Section 4.2.5, a plot of $\log(\phi)$ against $\frac{s}{s_0}$ can be obtained; this is shown in Figure 4.11. The value of q obtained by this procedure is 2.4.

4.2.7 Calibrated Results

Based on the calibrated results above and the calibration of Xiao (1997) and Melanson (1998) for other parameters in the constitutive equations in Section 4.1, calibrated parameters of the mechanical model for finite element implementation described in Section 4.1 are given in Table 4.1.

Table 4.1 Calibrated model parameters for the mechanical model for finite element implementation.

Description	Parameter	Value (unit)
Elastic modulus	E	9500 (MPa)
Elastic modulus in Kelvin Unit	E_k	9500 (MPa)
Poisson's ratio	v	0.3
Primary creep reference rate	$\dot{\varepsilon}_0^{\,d}$	1.0×10^{-5} at -10°C
Secondary creep reference rate	$\dot{\varepsilon}_0^{\,c}$	1.76×10^{-5} at -10°C
Creep exponent for Kelvin Unit	n	1.0
Creep exponent for Maxwell Unit	m	2.5
Volumetric Constant	f_3	0.11
Reference stress	s_0	15 (MPa)
Creep enhancement parameter	β_d	1
Creep enhancement parameter	β_c	1
Damage function constant	a_1	0.7
Reference pressure	p_1, p_2	50
Damage function constant	a_2	0.12
Low pressure exponent	g	2
High pressure exponent	r	6
Damage function exponent	q	2.4

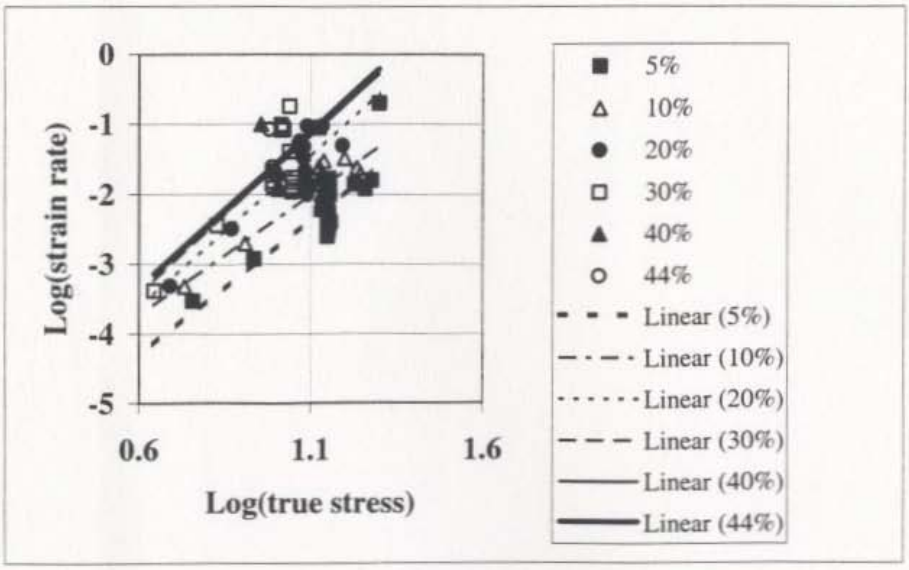

Figure 4.1 Plot of logarithm of true strain rate versus the logarithm of true stress of all tests (Melanson, 1998)

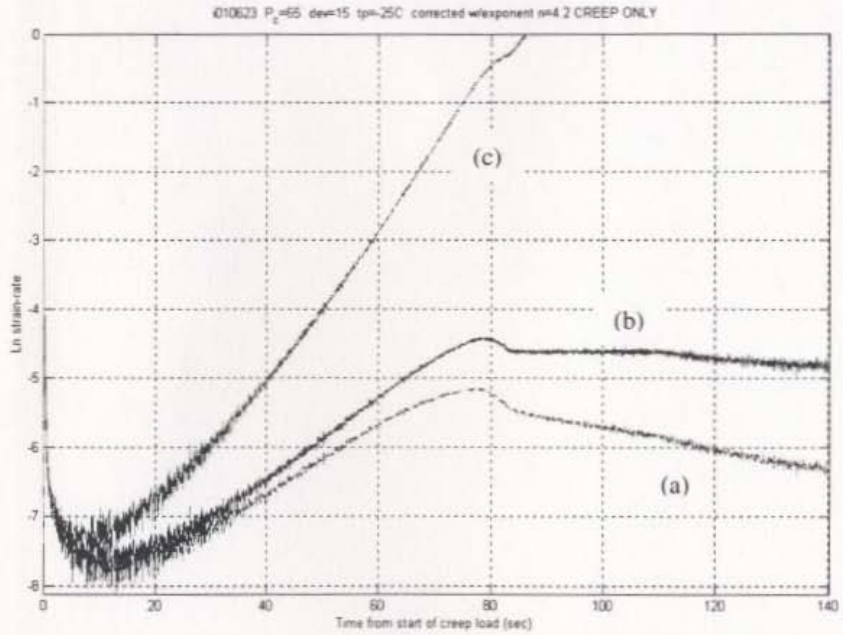

Figure 4.2 Natural logarithm of strain rate against time for (a) original data; (b) after the first correction; (c) after the second correction

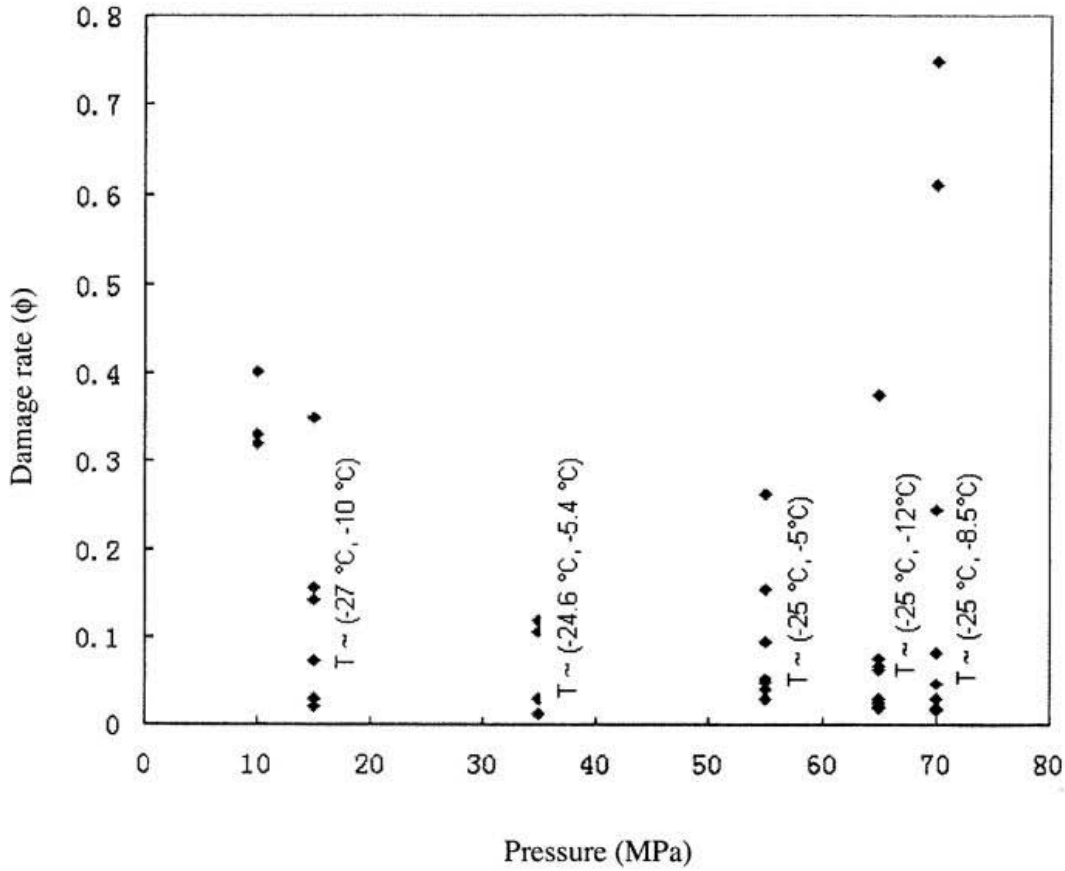

Figure 4.3 Damage rate(ϕ) plotted versus hydrostatic pressure for data under different temperatures from all the tests with the first correction of stress and strain rate

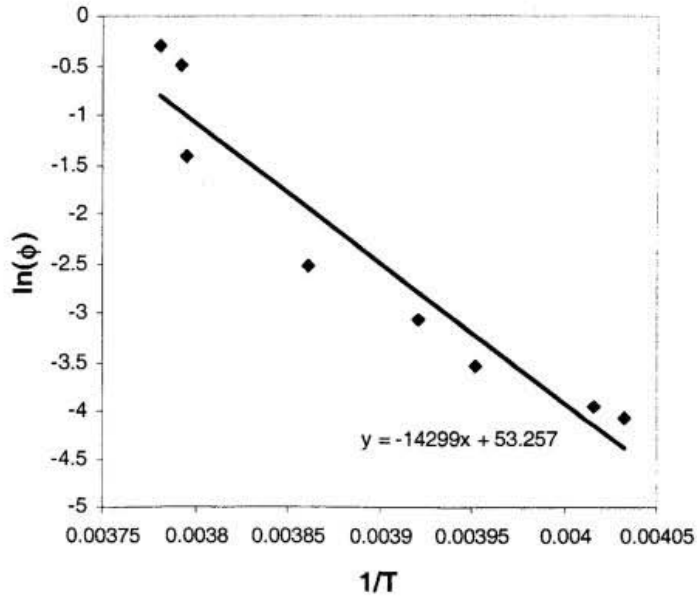

Figure 4.4a ln(ϕ) against 1/T at pressure = 70 MPa after the first correction

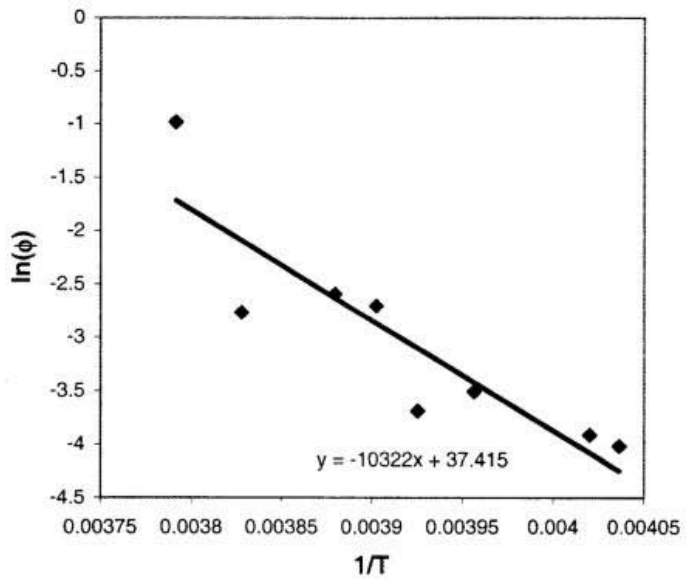

Figure 4.4b ln(ϕ) against 1/T at pressure = 65 MPa after the first correction

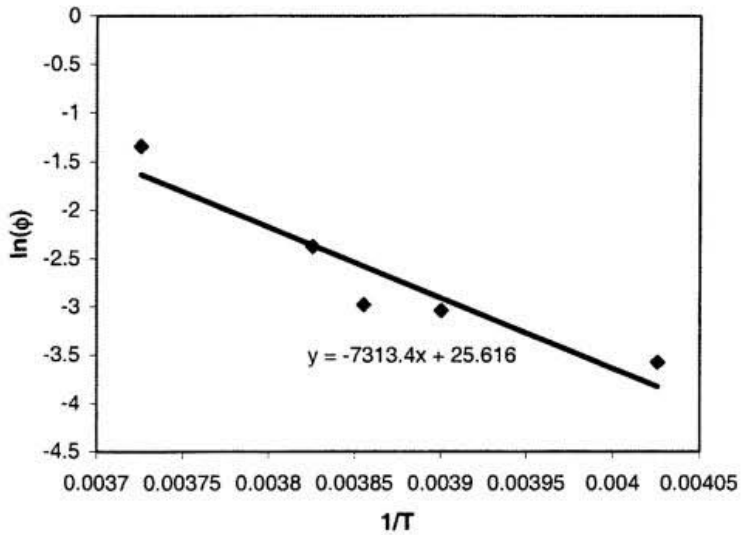

Figure 4.4c ln(ϕ) against 1/T at pressure = 55 MPa after the first correction

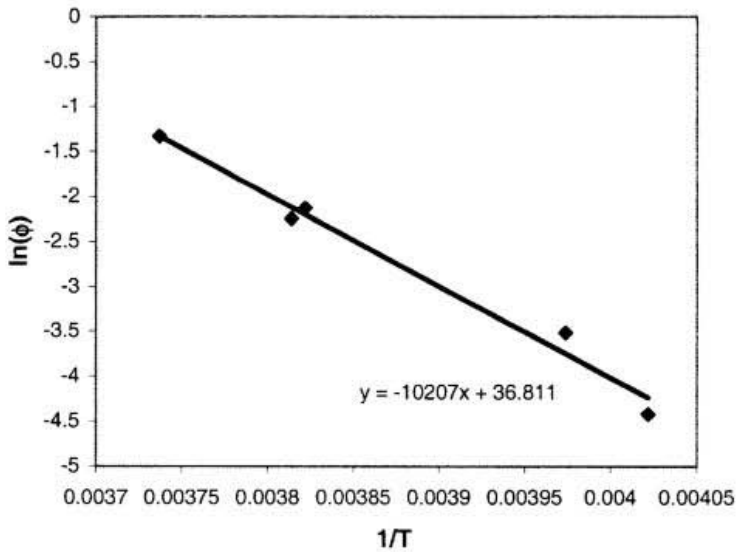

Figure4.4d ln(ϕ) against 1/T at pressure = 35MPa after the first correction

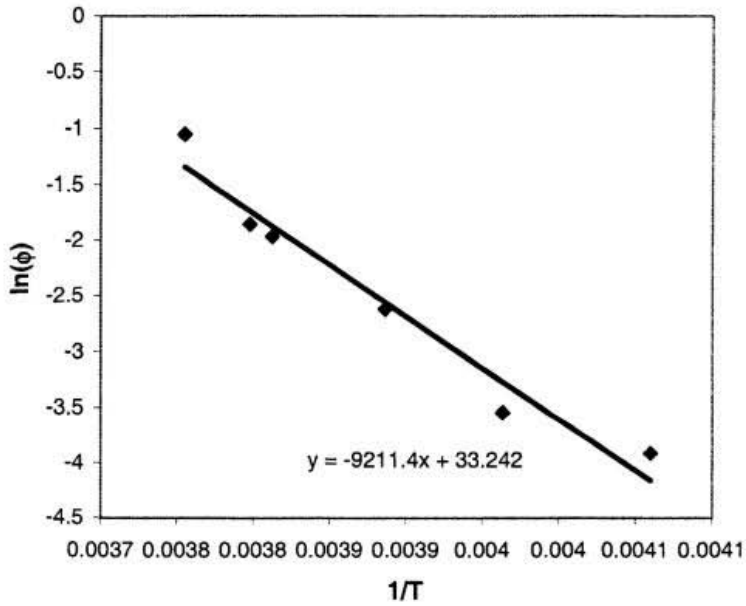

Figure 4.4e ln(ϕ) against 1/T at pressure = 15 MPa after the first correction

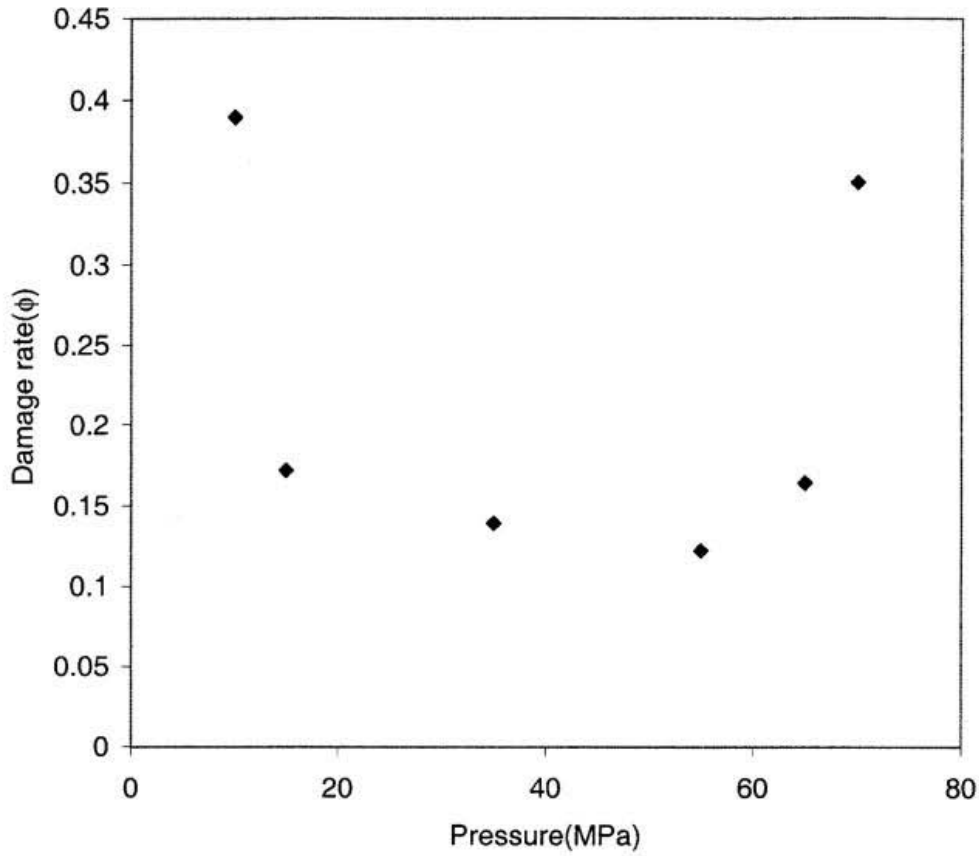

Figure 4.5 Damage rate(ϕ) plotted against hydrostatic pressure at -10°C after temperature correction for the first calibration

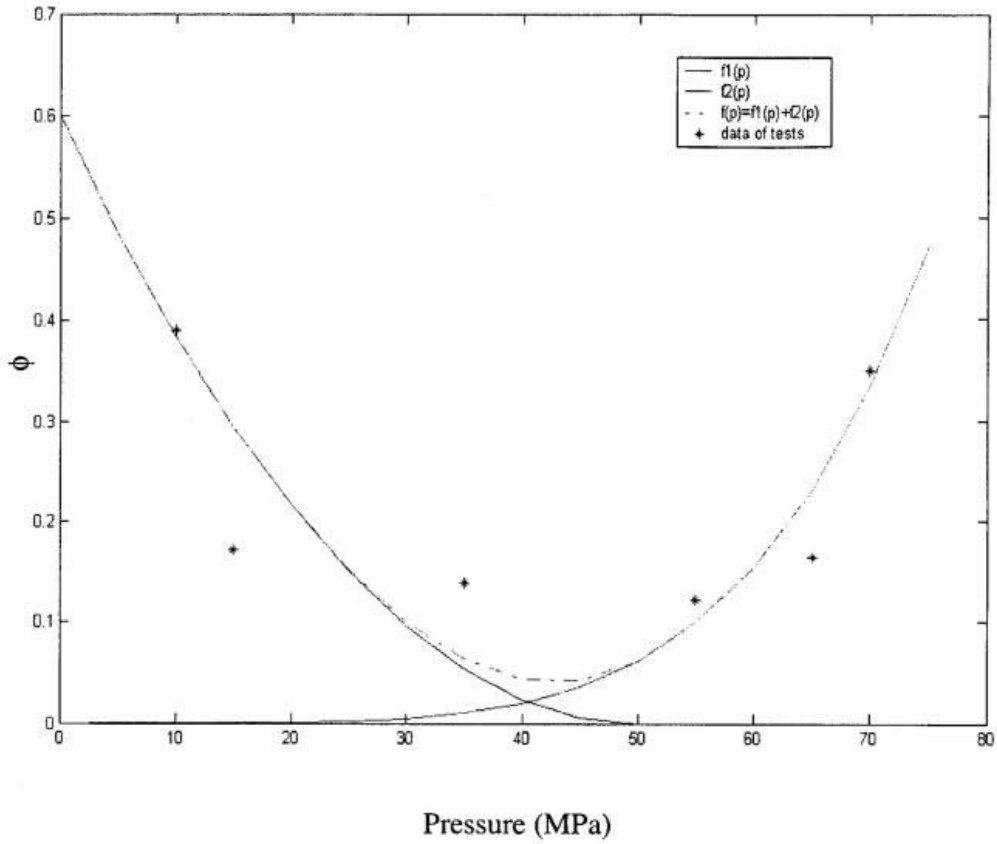

Figure 4.6 The two pressure dependent terms of the damage function, $f_1(p)$ and $f_2(p)$, plotted and summed to show the resultant function $f(p)$ after the first calibration

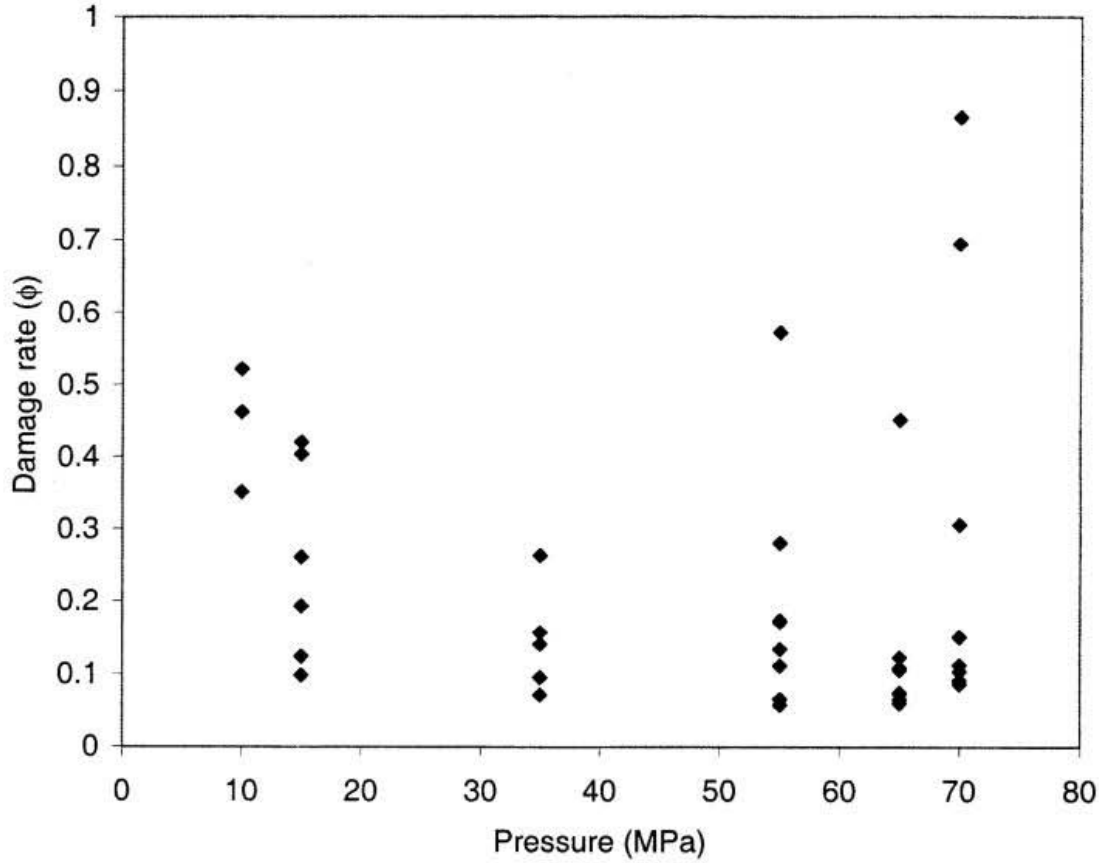

Figure 4.7 Damage rate(ϕ) plotted versus hydrostatic pressure for data under different temperatures from all the tests after the second correction

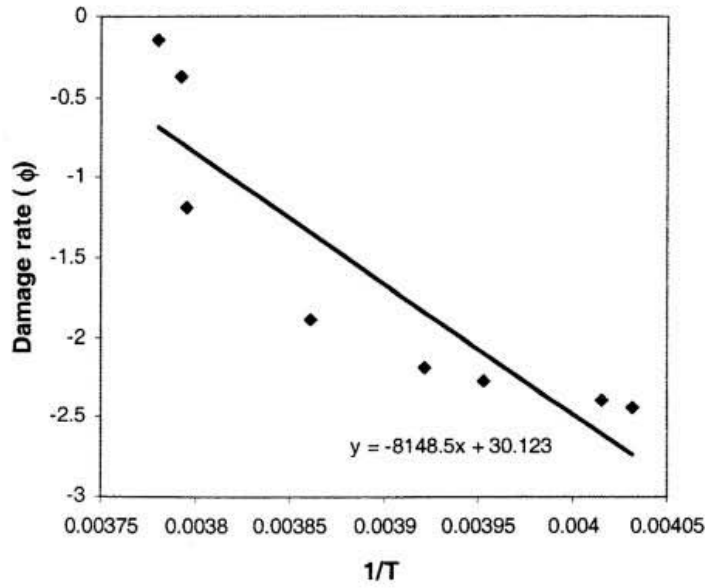

Figure 4.8a ln(ϕ) against 1/T at pressure = 70 MPa after the second correction

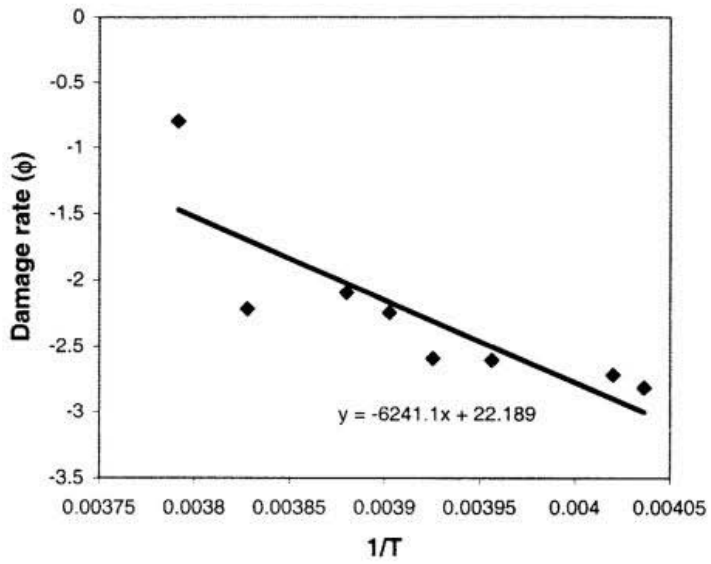

Figure 4.8b ln(ϕ) against 1/T at pressure = 65 MPa after the second correction

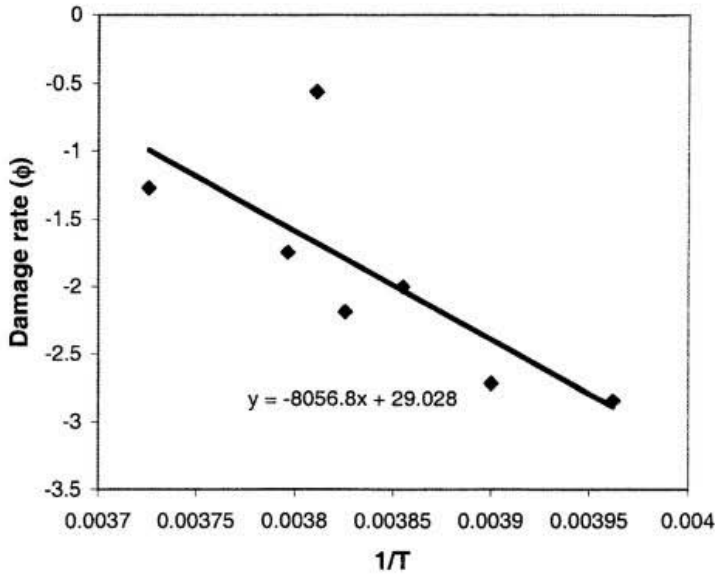

Figure 4.8c ln(ϕ) against 1/T at pressure = 55 MPa after the second correction

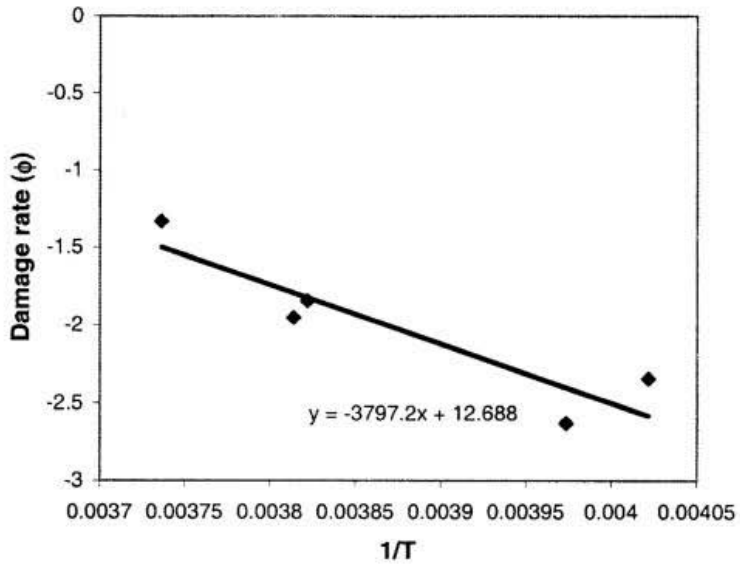

Figure 4.8d ln(ϕ) against 1/T at pressure = 35 MPa after the second correction

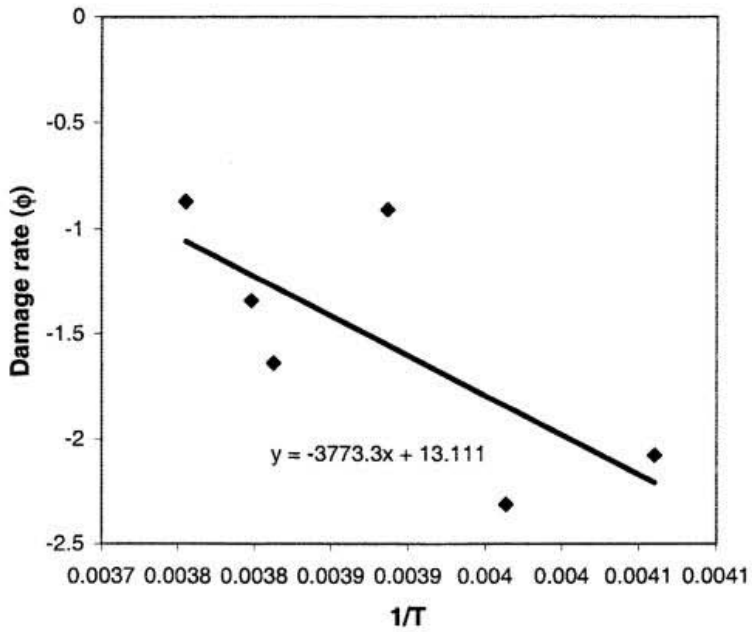

Figure 4.8e ln(ϕ) against 1/T at pressure = 15 MPa after the second correction

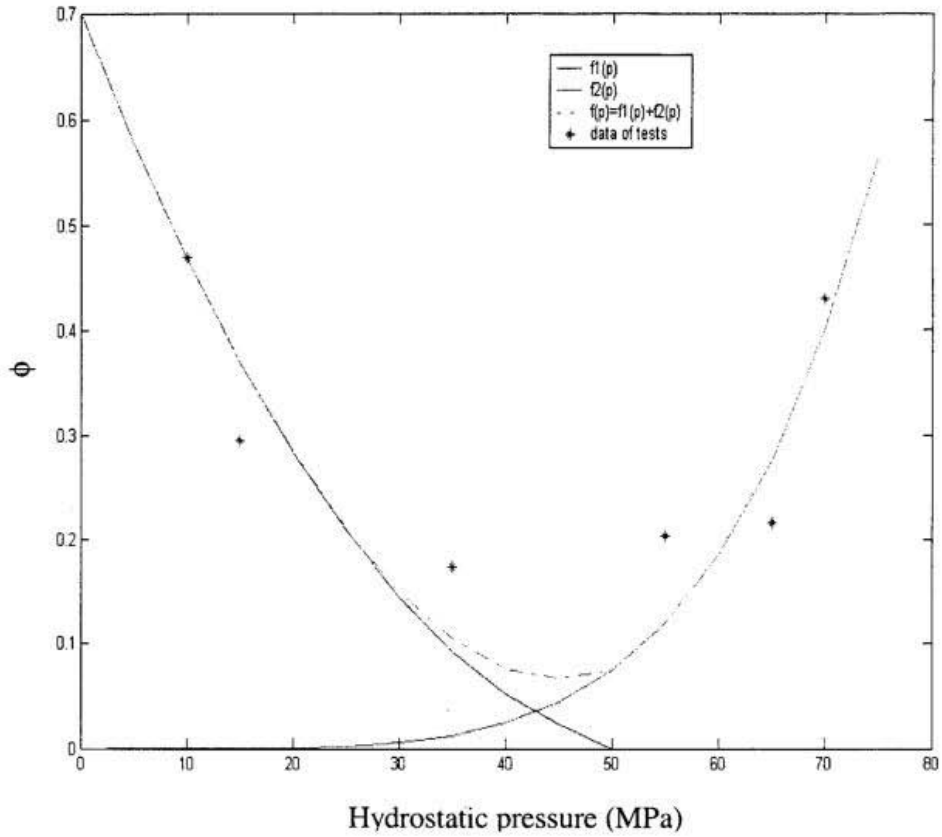

Figure 4.9 The two pressure dependent terms of the damage function, $f_1(p)$ and $f_2(p)$, plotted and summed to show the resultant function $f(p)$ after the second calibration

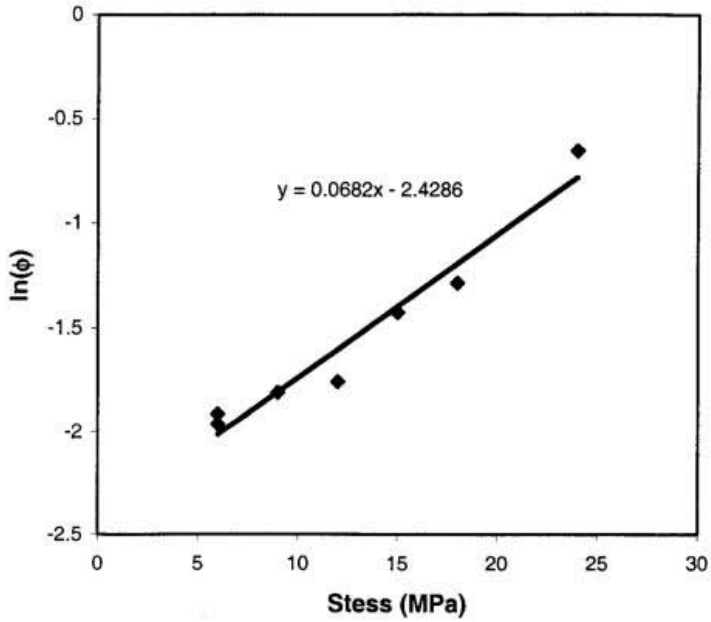

Figure 4.10 Natural logarithm of damage rate, ϕ versus stress at pressure = 55 MPa

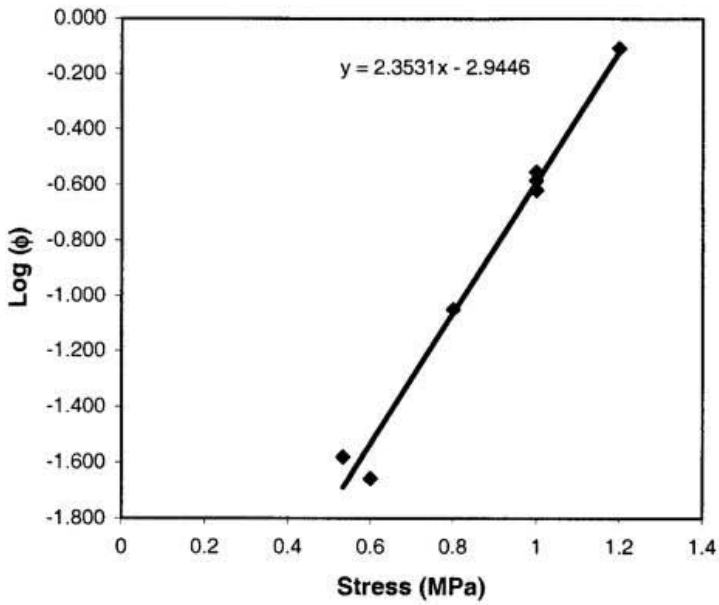

Figure 4.11 Logarithm based on 10 of damage rate, ϕ versus stress at pressure = 10 MPa

Chapter 5

Numerical Analysis of Triaxial Small-scale Ice Tests

As discussed in Chapter 3, two typical mechanical behaviours (ductile behaviour and runaway behaviour) have been observed during the tests in laboratory. From the experimental results, the runaway strain tends to occur at low and high pressure levels for intact laboratory ice under triaxial loading conditions and occurs without obvious pressure dependence for iceberg ice with initial flaws. The runaway strain is believed to be triggered by inhomogeneities in the ice which can cause the formation of localized bands of intense straining. Once localization takes place, large strains can accumulate inside the band and lead to rupture. The term localization used here refers to situations in which the concentration of deformation into a band is an outcome of constitutive behavior of the materials or boundary effects.

In this chapter, the mechanisms of strain localization and consequent instability for rate-independent and rate-dependent materials are studied. Finite element analyses are

conducted with two kinds of inhomogeneities (material imperfection and end effects) in order to study the possible mechanisms of strain localization in ice.

5.1 Mechanisms of Localized Strain and Instability

Besides having been observed in ice, shear instabilities in the form of shear bands are commonly observed in metals and polymers subjected to large deformations. The formation of a shear band is often an immediate precursor to rupture of the materials as observed by Molinari and Clifton (1987) and Anand *et al.* (1987) for viscoplastic solids, and Armero (1999) for rate-dependent inelastic solids and Borja *et al.* (2000) for soft rock. The physical mechanisms responsible for triggering localization vary widely. For example, thermal softening plays a key role in initiating localization at high rates of loading in structural metals (Costin, 1979) and in viscoplastic materials (Molinari and Clifton (1987) and Shawki (1994)). In brittle materials such as rocks, faulting appears to be caused by microcrack nucleation, growth and coalescence under uniaxial compressive stress conditions (Needleman, 1988). His study used incremental constitutive equations to discuss the formation of localization. For rate-independent elastic-plastic materials under homogenous conditions, the incremental constitutive equation can be written as

$$\dot{\tau} = G(\dot{\gamma} - \dot{\gamma}_p), \tag{5.1}$$

where τ is shear stress; G is elastic shear modulus; γ is total shear strain and γ_p is the strain for plastic loading. This strain can be expressed as follows:

$\dot{\gamma}_p = \dot{\tau}/H$ for plastic loading

otherwise,

$$\dot{\gamma}_p = 0. \tag{5.2}$$

Here, H is plastic hardening modulus (see Figure 5.1).

Combining Eq.(5.1) and (5.2) provides

$\dot{\tau} = G_t \dot{\gamma}$ for plastic loading

otherwise

$$\dot{\tau} = G\dot{\gamma}, \tag{5.3}$$

where G_t (see Figure 5.1) is effective modulus and can be given as $1/G_t = 1/G + 1/H$ (Needleman, 1988).

Considering quasi-static loading conditions, assume that a bifurcation from a state of homogeneous shear into a deformation pattern with a shear band appears at some stage of the deformation history as sketched in Figure 5.2. Stress equilibrium requires

$$\dot{\tau}_b = \dot{\tau}_o , \tag{5.4}$$

where the subscripts b and o represent the region inside the band and outside the band, respectively, corresponding to Figure 5.2.

Substituting Eq.(5.3) into (5.4) gives

$$G_t(\dot{\gamma}_b - \dot{\gamma}_o) = 0. \tag{5.5}$$

A nontrivial solution to Eq.(5.5) is only possible when G_t vanishes so that localization is associated with strain softening.

However, for rate-dependent solids, the constitutive equation is different from rate-independent materials and can be expressed as

$$\dot{\tau} = G(\dot{\gamma} - \dot{\gamma}_v), \tag{5.6}$$

Here, γ_v is used to represent the viscous strain and other creep strain such as delayed elastic strain for ice.

Then, considering the quasi-static loading conditions, at some moment of the deformation history when a bifurcation appears, equilibrium requires that the stress state remains homogenous as described in Eq.(5.4). Combining Eq.(5.6) and (5.4) gives

$$G(\dot{\gamma}_b - \dot{\gamma}_0) = 0. \tag{5.7}$$

Since the elastic shear modulus, G, is positive, the unique solution to Eq.(5.7) is $\dot{\gamma}_b = \dot{\gamma}_o$. In fact, Eq.(5.7) excludes bifurcation. Needleman (1988) also used a minimum potential method to confirm this point. Accordingly, for rate-dependent materials, to get a nontrivial solution to Eq.(5.7), a band with some kind of imhomogeneity such as material properties or stress levels different from those in the surrounding materials has to be introduced. Therefore, a solution can be constructed in which there is uniform straining inside the band and uniform straining outside the band with a jump strain rate across the band. The crucial role of imhomogeneity at quasi-static conditions for rate-dependent materials was studied by Anand *et al.* (1987), Molinari and Clifton (1987), Belytschko *et al.* (1991) and Bayliss *et al.* (1994).

Strain localization doesn't necessarily lead to immediate failure, even though a band with different material properties exists. The governing equation for strain localization

instability is $\dot{\gamma}_b / \dot{\gamma}_o \rightarrow \infty$ (Hutchingson and Neale, 1977). By this criterion, a localization instability is associated with an increment of strain occurring in the band and no increase in strain outside the band. Under this condition, the strain localization will dominate the failure. Needleman (1991) used a linear Kelvin-Voigt model to study the localization instability in progressively softening solids by this governing equation. The term progressive softening is used to refer to circumstances where, at least for certain deformation histories, the constitutive relation permits the stress to decrease monotonically to zero after the attainment of a maximum stress. As summarized by Needleman (1991), localization dominates the failure when the material inside the band softens while material outside the band hardens.

5.2 Finite Element Analysis of Localized Failure in Ice Specimens

5.2.1 Model Description

Ice is a progressive softening material which requires a framework that can characterize the actual softening process to model properly the progressive softening and study the localization problem. The nonlinear viscoelastic constitutive equation with damage effects described in Chapter 4 is assumed to be valid for describing ice behavior at high strain levels. With the calibrated damage model discussed in Chapter 4, a UMAT subroutine was written to simulate the time-dependent material properties of ice. The

finite element analysis software, ABAQUS, was used to analyze cylindrical ice specimens deformed to high strain levels.

The length and diameter of the cylindrical specimen were taken as 155 mm and 70 mm, respectively. An axisymmetric condition was assumed and four-point continuum axisymmetric elements (CAX4) were used for the whole specimen. The ice at the beginning of the tests was assumed to be intact. A 20×10 mesh matrix was used. The 2-direction (see Figure 5.3) degree of freedom was fixed for bottom surface of the specimen. The constant load, 57.6 KN, was appled in the 2-direction degree of freedom on the top surface of the specimen. Three cases with confining pressure equal to 15 MPa, 35 MPa and 60 MPa have been studied, which represent low, medium and high pressure levels. The meshed undeformed model is shown in Figure 5.3. The analyses were performed at a constant temperature of –10 °C.

5.2.2 Results and Discussion

As discussed in Section 5.1, for rate-dependent material under homogenous conditions, the strain localization is entirely excluded. Therefore, an inhomogeneity has to be introduced in order to trigger the strain localization. Two types of analyses were made in this research. The first was to introduce a material imperfection inside the specimen with a low elastic modulus as compared to the surrounding ice. The second was to fix the 1 and 3 directions degree of freedom (see Figure 5.2) at the two ends of the specimen to model the friction effect which is believed to be able to cause an inhomogeneity.

For the analysis including a material imperfection, the local inhomogeneity was put in two different positions of the specimen to study its effect. The results of the finite element analysis are shown in Figure 5.4. This shows that the enhanced strains occur within a band triggered by the imperfection along with the normal shear orientation of 45°. It also shows that the strain localization band is sensitive to the position of the imperfection.

For the case without imperfections, three cases as described in Section 5.2.1 with constraints in the 1 and 3 directions were analyzed. Damage contour plots for the specimen under different pressures are showed in Figure 5.5. It demonstrates that damage at pressure = 15 MPa and 60 MPa grows very fast at the center of the specimen in comparison to the surrounding areas and forms a band along with the normal shear direction. This inhomogeneity is caused by end effects which lead to the non-uniform of the damage distribution. In Figure 5.5 damage at pressure equal to 35 MPa is small and almost uniform throughout the whole specimen because in this case the growth of damage is restricted.

Therefore, ice inside the band is damaged faster and more severe, which make the properties of ice change much quicker, than that in the surrounding areas at pressure of 15 MPa and 60 MPa,. At some stage of the damage evolution, it is quite likely that this process will cause the ice inside the band to soften while the ice in the surrounding areas is still in a hardened state. Strain localization instability will occur along the band and cause the ice to fail.

Recently, studies of ductile fracture were conducted by Bandstra and Koss (2001) by introducing two voids inside the materials; Orsini and Zikry (2001) did a similar analsysis with four voids. Both the studies showed strong tendency for strain localization between the voids which can be attributed to the void growth and interaction. Both the constitutive model and the numerical model show that strain localization can be induced by inhomogeneities of mechanical properties such as initial flaws or the end effect for ice. From the analyses for intact laboratory ice, it seems that the confining pressure plays a significant role in the initiation of the strain localization. It shows that when temperature is equal to -10°C, at the low pressure and high pressure levels strain localization occurs readily, but at the medium pressure level, ice is less prone to localization. This meets the observation from the experiments as described in Chapter 3.

Other possible mechanisms of the strain localization and rupture should be considered. As proposed by Molinari and Clifton (1987) and Bayliss *et al.* (1994), for viscoplastic materials at high strain rate deformation, the thermal effect may be significant for the onset of strain localization. This effect has been observed in ice because the temperature through the specimen is not uniform in the tests. The higher the temperature is, the softener is the ice and the imhomogeneity is caused by the thermal effect. The current numerical model can only predict the possibility of the strain localization. For post-localization behaviour (onset of rupture and its growth), a special numerical technique has to be established to solve the strong discontinuity of the mechanical behaviour on the rupture plane and outside the rupture plane.

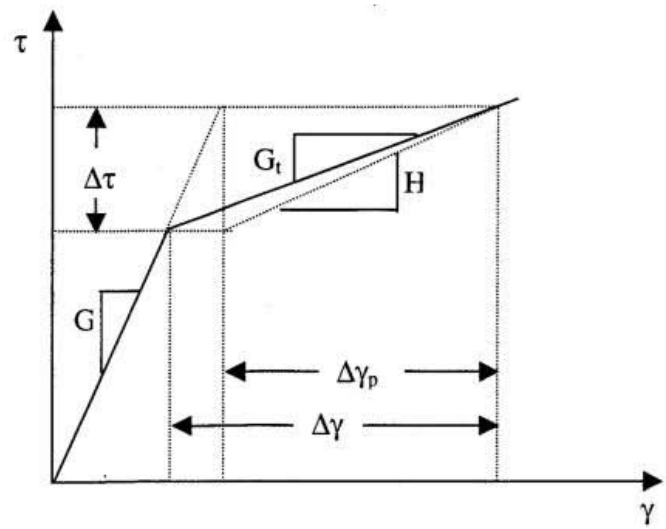

Figure 5.1 Stress-strain relationship for bilinear elastic-plastic material.

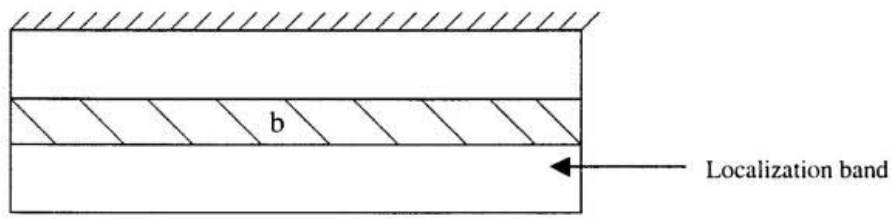

Figure 5.2 Simple shearing of a planar strip.

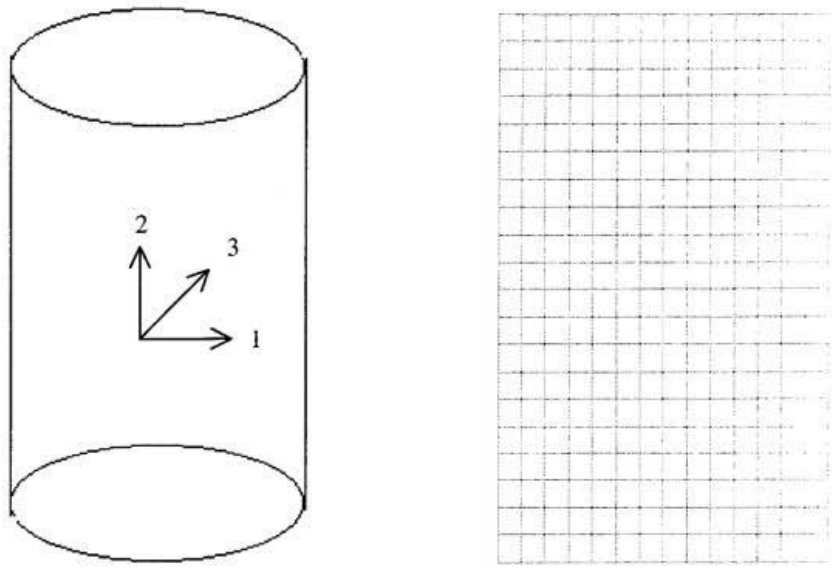

(a) (b)

Figure 5.3 (a) Ice cylindrical specimen; (b) Mesh for a specimen

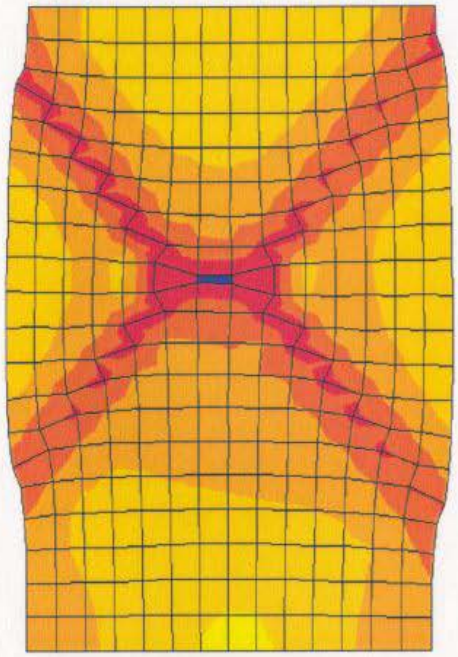

Figure 5.4a Deformed mesh for the imperfection near the center.

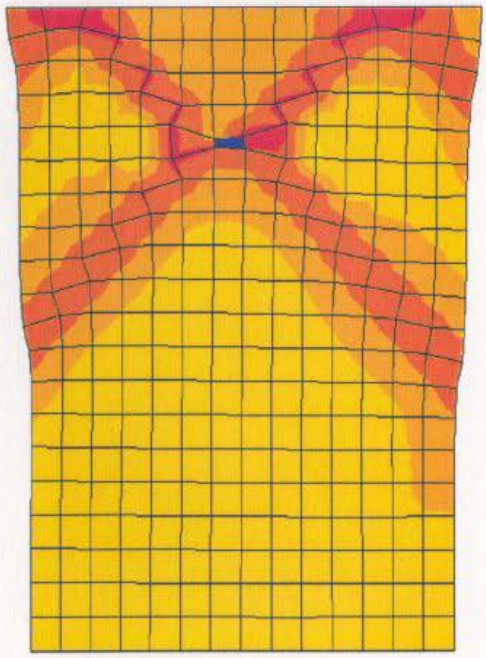

Figure 5.4b Deformed mesh for the imperfection near the top end

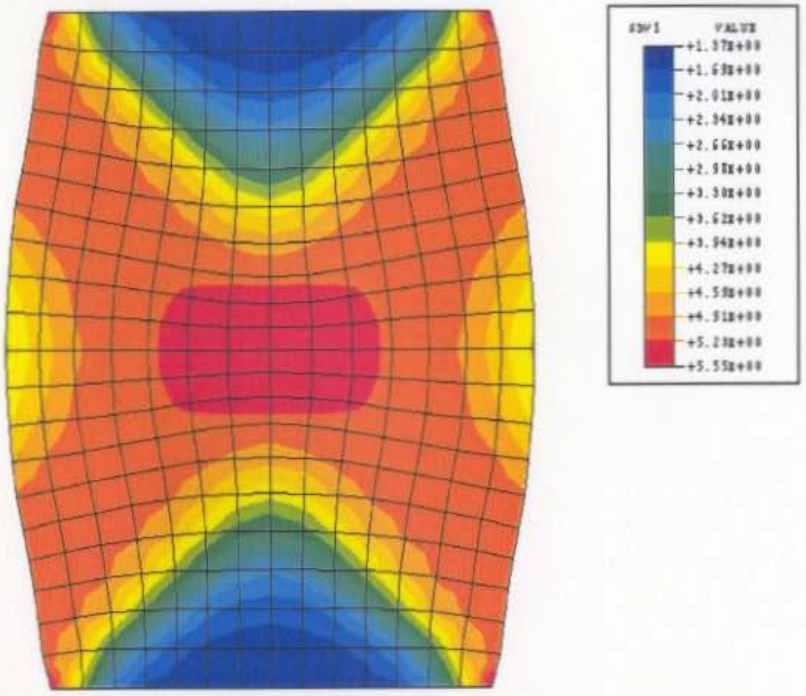

Figure 5.5a Damage contour plot for pressure = 15 MPa

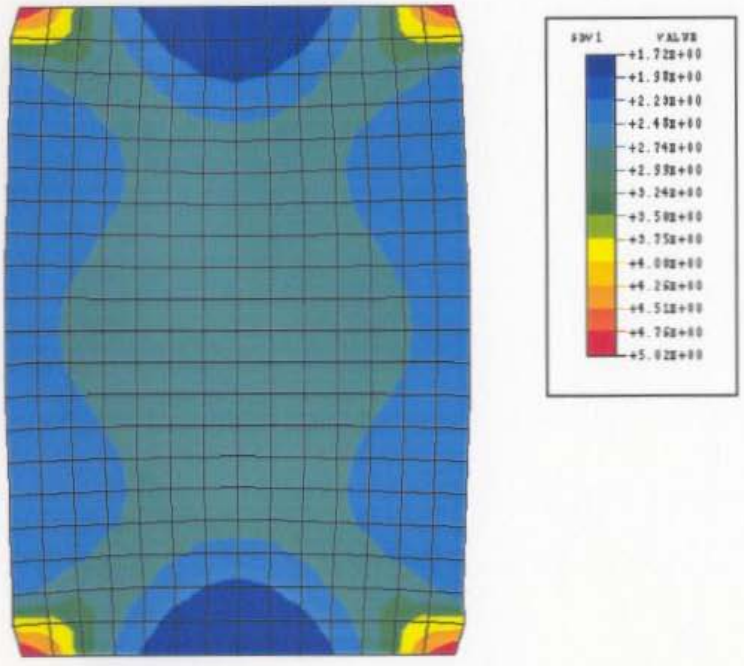

Figure 5.5b Damage Contour plot for pressure = 35 MPa

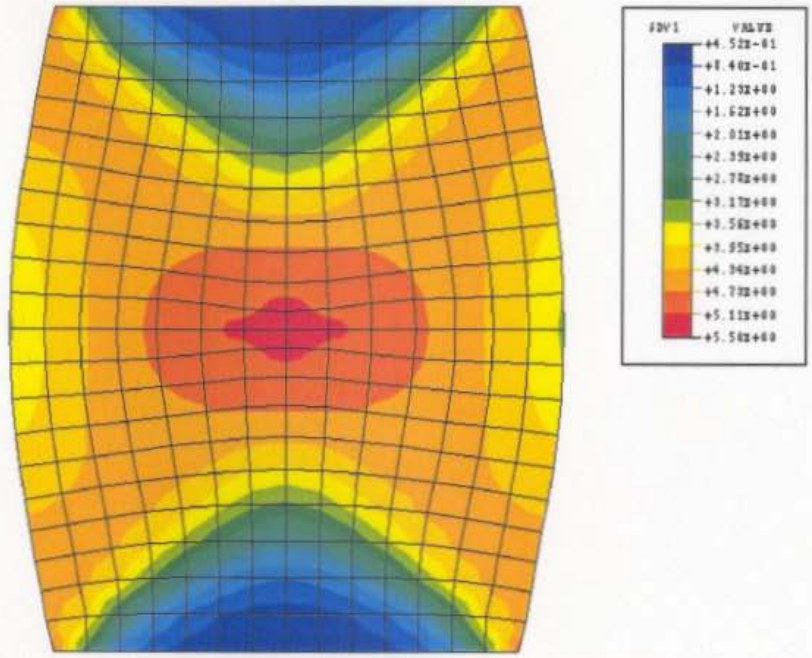

Figure5.5c Damage contour plot for pressure = 60 MPa

Chapter 6

Finite Element Analaysis of Indentation Tests

In this chapter, finite element modeling of one of the indentation tests, TFR07, (Frederking *et al.* 1990 a, b) conducted at Hobson's Choice Ice Island in the 1990's is described to study the high pressure zone. The indentor used in this test is flat and rigid and moves towards the ice mass at a constant speed of 68 mm/s during the whole indentation process. The sketch of the ice mass is shown in Figure 6.1. Since big spalls occurred at the corners at the beginning of the interaction, the ice mass in contact with the indentor is simplified as a pyramidal shape with a radius of 0.1m on the top surface and a slope of 2:3. Finite element analysis is made to simulate this process. Damage evolution and stress state are studied. Mechanisms of formation of the damaged layer involved in this interaction are studied. Scale effect for high pressure zones is also studied with the finite element method.

6.1 Model Description

The whole interaction system can be simply divided into two parts in finite element analysis: the indentor and the ice mass. The finite element geometry is shown in Figure 6.2. Since the whole system is symmetric, an axisymmetrical condition has been assumed to simplify the modelling. The model for the indentor in this analysis is simulated as a flat rigid body by fixing all the degree of freedoms except the 2-direction with a constant speed towards to the ice mass. The ice mesh is separated into three zones with different mesh sizes and material properties. Zone 1 shown in Figure 6.2 is near the contact interface and the mesh is the finest of the three zones. The material in this zone obeys the constitutive model coupled with damage effects as described in Chapter 4. Zone 2 is adjacent to zone1 and has a coarser mesh. It also follows the constitutive model with damage for the ice. Zone 3 is the area surrounding zone 2; it is coarsely meshed and the ice in this zone is taken elastic since damage can be negligible in this zone. The purpose of zone 3 in the finite element mesh is to reduce the boundary effect as discussed by Xiao (1991). The bottom of the ice mass is fixed in both 1 and 2 directions. The temperature of the test is – 10 °C.

6.2 Modelling Results and The Layer Study

Liu (1994) and Xiao (1997) both studied the parameters related to the damage constitutive model and found that they have significant effects on the shape of the load-time curve as well as the magnitude of the peak load. In this research, the calibrated

model in Chapter 4 is applied. Since there are some initial flaws in the ice mass for medium scale indentation tests performed in Hobson's Choice Ice Island, a preexisting scalar damage is given at the beginning of the analysis.

The time history of the applied force is given in Figure 6.3 by the solid line, and the test load history is given by the dashed line. It can be seen that the numerical results compare well with the test data in both the amplitude and frequency. The numerical result is a little higher than the test data, because the current numerical technique can not debond the damaged elements from the parent ice mass. Figure 6.3 also shows that the reaction load will drop at a specific phase of the indentation history. The drop-off of the load is believed to be related to the instability of the deformation caused by strain softening effects within the layer of damaged ice. However, the model results are only valid at the early phase of the drop-off of the applied force. This is because at the moment of the drop-off, the pressure melting effect will reverse accompanying with the stress decrease and some of the microcracks can disappear due to the pressure melting. This reverse of damage is not well understood currently and is not considered in the model, so the present numerical analysis can only simulate accurately half a cycle of the loading history.

Figure 6.4 illustrates the damage evolution process. Figure 6.4(a), 6.4(b) and 6.4(c) show the damage contour plot at the points a, b and c (see Figure 6.3) of the reaction load history, respectively. It can be seen that severe damage first occurs at the edge of the ice mass and expand towards the center of the ice mass along a thin layer. Severe damage finally concentrates on the thin layer along the contact surface. Physically, microcracking

was observed at the edge of the ice mass as the result of the stress concentration. This process expands to the center gradually. At a specific moment of the indentation, the confining pressure at the central area increases to a value sufficient to induce the severe pressure softening effects and damage will finally concentrate on the layer along the contact surface. The pressure distribution along the layer is shown in Figure 6.5 for the moment before the peak load, at the peak load and after peak load, respectively. It illustrates that the pressure distribution shows a roughly parabolic curve around peak load. This can be interpreted by the damage evolution history discussed above. Severe damage starting from the edge softens the ice at that area, decreasing the pressure at the edge. Note that there is a slight drop-off of pressure at central area of the pressure distribution before the peak load. This is because that the pressure softening effect starts from the central area and reduce the total pressure although the softening effect is not severe at the beginning. A similar figure was obtained by Xiao (1991) with a spherical indentor. Figure 6.6 shows the comparison between von Mises stress and confining pressure at different positions along the contact surface. It can be seen that at the edge of the contact surface, von Mises stress (21 MPa) is dominant and confining pressure (4 MPa) is negligible in comparison to von Mises. Confining pressure becomes more and more significant towards to the centre. Confining pressure (46 MPa) is bigger than von Mises (37 MPa) at the central element and the two components (von Mises = 36 MPa; confining pressure = 31 MPa) are almost even at the middle between the edge and centre. The comparison provides an evidence to explain the different mechanisms of damage formation at the edge and at the centre observed in the field test (see Chapter 3).

As discussed above, the drop-off of the reaction load in the indentation history is believed to be related to ice softening inside the layer. This can be illustrated by the energy flux evolution. Three phases were selected: the first was at time of 0.02 s; the second was at the time of 0.048 s (near peak load) and 0.05 s (just after the peak load). The energy flux evolution is shown in Figure 6.7. Energy in phase I flows into the ice mass roughly uniformly except at the edge of the indentation surface. This is because the ice is not severely damaged at the beginning of the contact and energy flows everywhere equally except at the edge as the result of stress concentration. Energy in phase II flows into the region near the central area because severe damage occurred near the region of the edge and softened the ice in that region. Energy at phase III flows into the thin layer along the contact surface because severe damage finally expanded to the whole layer and softened the ice inside the layer. Once ice softens, energy only flows into the softening region and instability will occur. At this moment ice behaves as a brittle material and the damaged layer will be extruded. After this process, a new cycle will begin. The arrow size indicates relative magnitude of energy flux, and the arrow direction indicates the direction of energy flux inside the ice mass. Note in Phase II and phase III that energy at the edge is lower than that at the center. This can be interpreted from Figure 6.5 where around the peak load pressure is much lower at the edge than that at the center.

6.3 Scaling Effect of High Pressure Zones

The problem of scale effect is particularly important to geotechnical materials such as ice because it is inevitable to use reduced-scale laboratory tests to extrapolate real structures, which are too large to be tested systematically. Realization of the problems involved in this extrapolation has led to a surge of interest in this subject in ice-structure indentation. Scale effect for ideal elastoplastic materials ia absent for which the failure criteria can be described by only a well-defined yield stress regardless of size effect as discussed by Jordaan (1999). It is also absent of scale effect for elastic-brittle materials with a constant fracture toughness regardless of scales. However, the model of ice used in this research is highly nonlinear time-dependent creep behaviour coupled with damage mechanics and doesn't have a given failure criterion dependent only on a well-defined yield stress. Therefore, motivation arises for the scale effect of the current model. Results of different scales from finite element analyses are used to study the problem.

Four materials in this section are studied. The first is the ideal elastic material. The second is the linear viscoelastic material. The third is the nonlinear viscoelastic material without any damage effects and the forth is the nonlinear viscoelastic material coupled with damage effects, which was applied in the ice indentation model. For each material, five geometrically similar indentation models have been studied. The diameters of the contact surfaces are 0.08 m, 0.16 m, 0.24 m, 0.48 m and 0.96 m, respectively. For the first three materials without damage, the failure criterion is described by a specific critical stress. For the nonlinear material with damage, the failure criterion is described at the

moment of peak load after which the reaction load will drop. The force-area data points compared with theoretical line without scale effect are shown in Figure 6.8 for each case. It can be seen from Figure 6.8 that the data points from finite element results match the theoretical line well for the elastic, linear viscoelastic and nonlinear viscoelastic materials without damage. Data points of finite element results tend to be below the theoretical line along with the increasing size for nonlinear viscoelastic material with damage effects. This indicates that there is a scale effect for this type of materials.

Bazant (1993) developed a power law relationship for scale effect in absence of characteristic length (for instance, as the depth of beam, the span, the notch size, and so forth). Letting Y as the nominal stress at failure, the scaling ratio Y^*/Y of the corresponding responses Y^* and Y depends only on the size ratio $\lambda = D^*/D$ of two different sizes D^* and D but is independent of the choice of the reference size D. let the scaling law be $f(\lambda)$, then

$$\frac{Y^*}{Y} = f(\lambda), \tag{6.1}$$

where $f(\lambda)$is the unkown function that needs to be found out. As proposed by Bazant (1993), that $f(\lambda)$ is a power function

$$f(\lambda) = \lambda^m. \tag{6.2}$$

For plasticity or elasticity with a strength limit, the value of m is 0 and for LEFM (linear elastic fracture mechanics), the value m is –0.5. The value of m is between –0.5 and 0 for nonlinear fracture mechanics or quasi-brittle materials. Bazant's approach is based on the assumption that the flaws increase in size as sample size increases. However, the flaws of

ice in field under compressive stresses may be micro-cracks, grain boundaries, pressure melting and other imperfections. Instead of strict geometric similarity, Sanderson (1988) gave a more realistic assumption that any material contains a statistical population of flaws of various sizes. On selecting a sample of larger size there is a higher chance of ice containing larger flaws which are not necessary to follow the geometric similarity. By assuming that the compressive failure obeys the "weakest link hypothesis" as what tensile failure does, Sanderson give a function of the failure strength as a function of volume, V in the form

$$\sigma \propto V^{-1/b_f} \text{ or } \lambda^{-3/b_f}, \tag{6.3}$$

where b_f is a statistical parameter charactering the flaw-size distribution. The value of b_f is approximately equal to 15 for fresh water ice (Lavrov, 1973) and equal to 1 or 3 by statistical analysis for *S-2* ice by Gold (1972).

A power law relationship of Eq. (6.2) or Eq. (6.3) can be applied on ice-structure indentation model discussed in Section 6.2 which is lack of characteristic length. The sizes and their corresponding nominal failure stress are listed in Table 6.1. The nominal failure stress against diameter is plotted in Figure 6.9 with a scale on logarithm based on 10. The slope of the regression line of Figure 6.9 shows that the exponent m as described in Eq. (6.2) is – 0.065 and the statistical parameter b_f is approximately 46 according to Eq. (6.3). Both Table 6.1 and Figure 6.9 show that the current model has a slight scale effect. However, the scale effect is not comparable to that of the ice failure dominated by flaws for which the exponent m is – 1 (Sanderson, 1988) and b_f = 15 for fresh water ice (Lavrov, 1973). The recent indentation tests by Sodhi (2000) didn't show a significant

scale effect and Sodhi (2000) concluded that it was absent of scale effect in ice-structure indentation. It was interpreted by Sodhi (2000) that the absence of the scale effect is as the result of the similar failure modes. However, Sodhi's results include some field tests which are not exactly the high pressure zones without any flaws. For high pressure zones without any initial flaws, the current model shows that the scale effect may be triggered by the damage evolution. The physical mechanisms of the slight scale effect in Figure 6.9 are still not well understood and need to be further studied. A set of indentation tests with different sizes is highly recommended to be conducted at the same experimental conditions and a probabilistic analysis is also recommended.

Table 6.1 Scale effect of ice-structure indentation

Size (m)	Failure Stress (MPa)
0.08	80.48
0.16	77.27
0.24	75.6
0.48	72.2
0.96	68.5

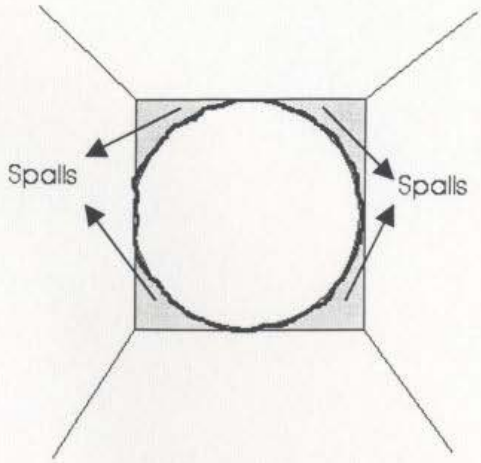

Figure 6.1 Stretch of the contact surface

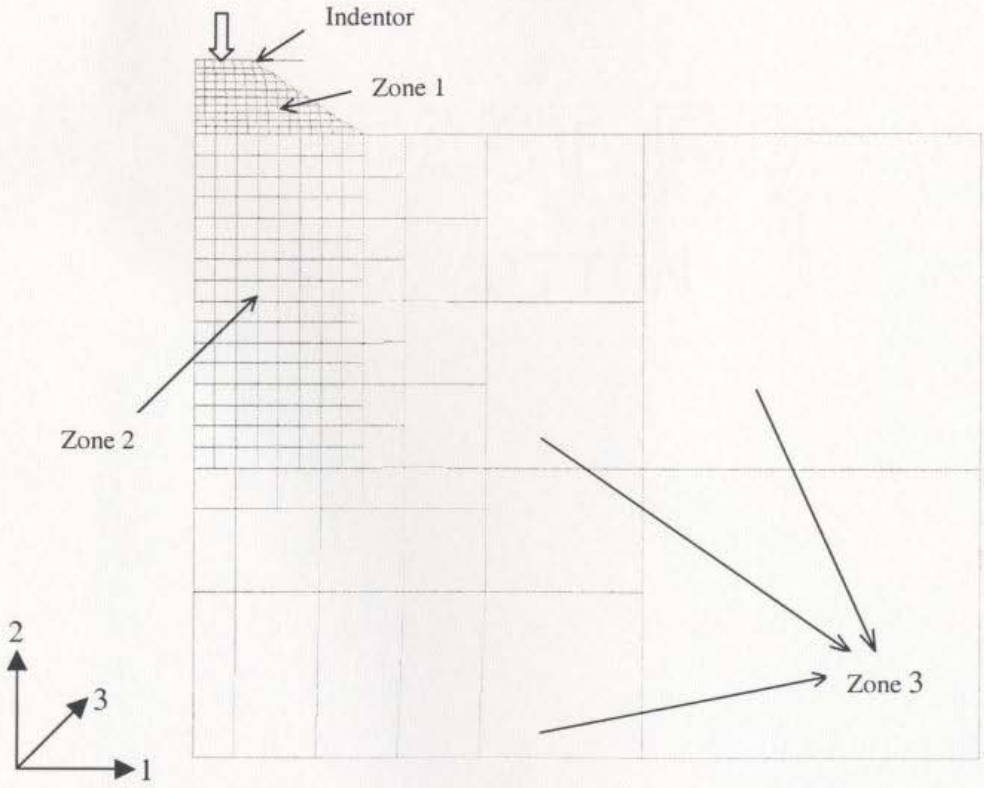

Figure 6.2 Mesh of the indentation model.

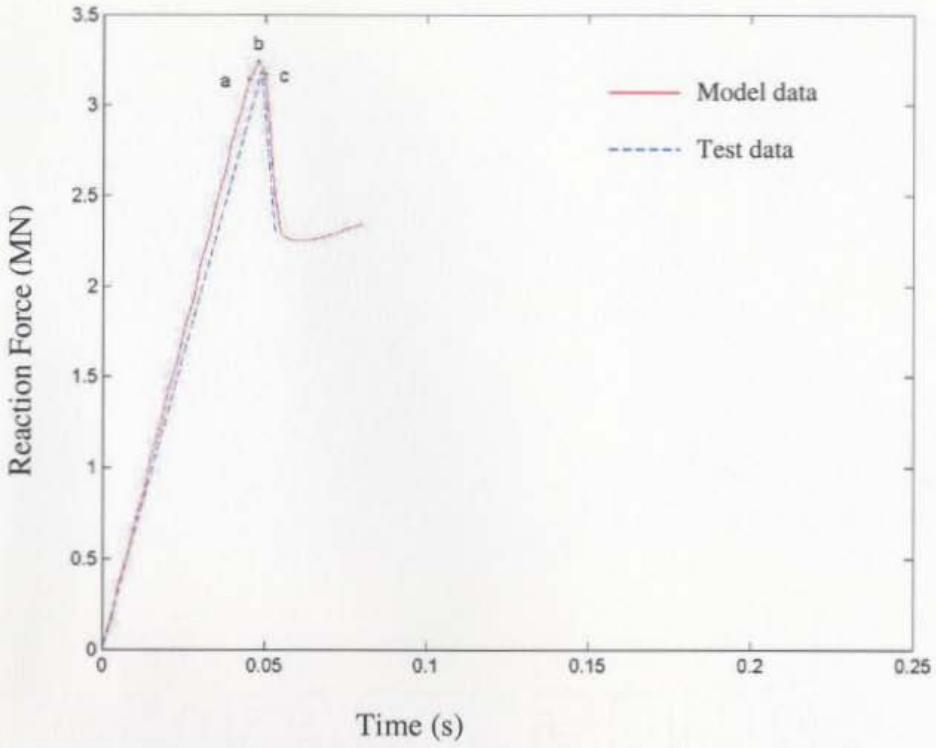

Figure 6.3 Comparison of reaction load history between test data and model data.

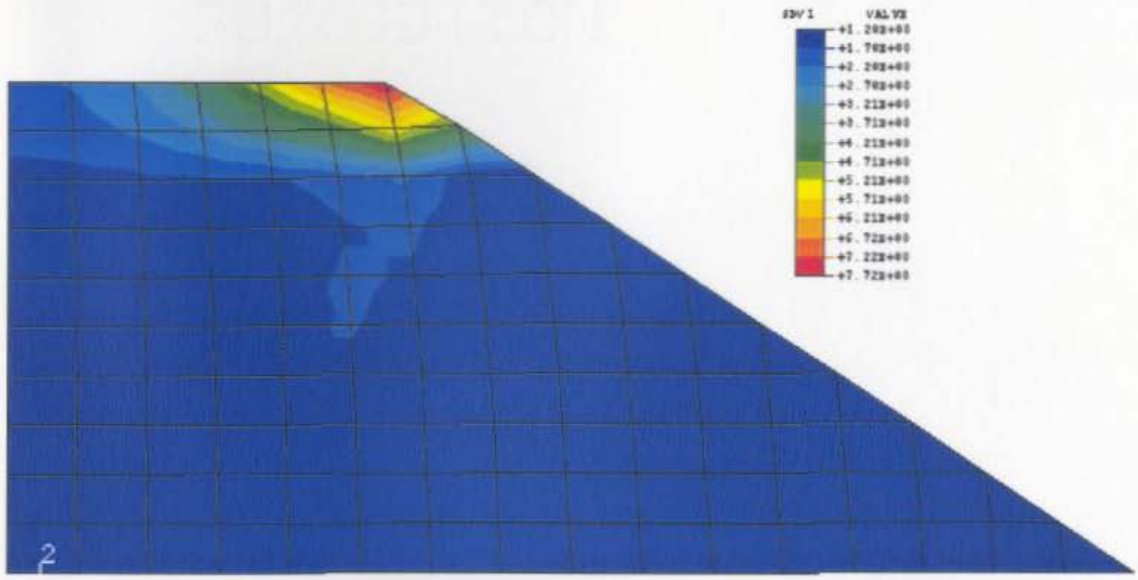

(a)

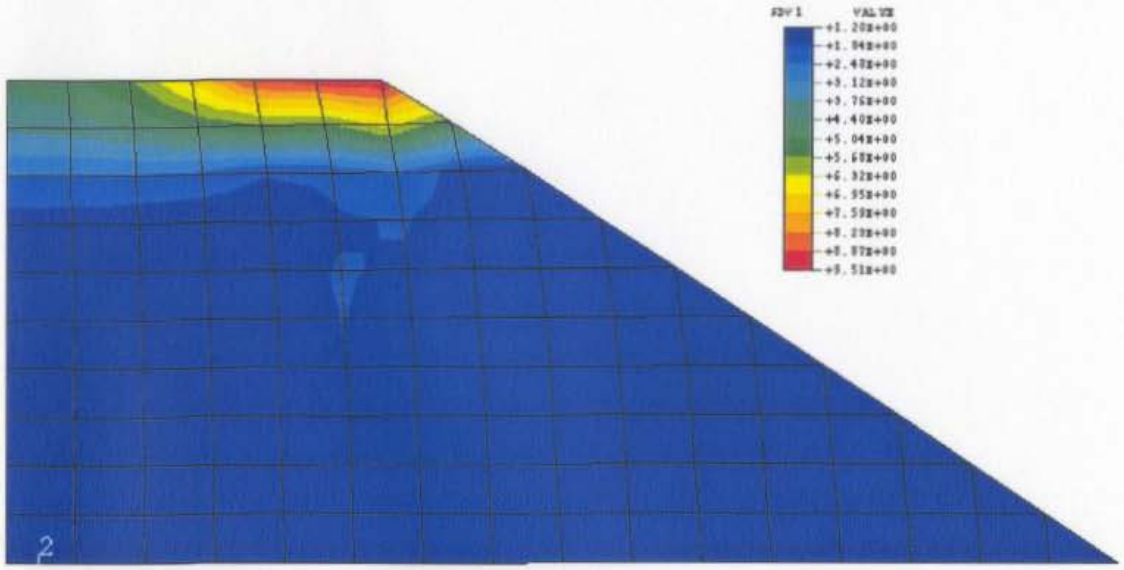

(b)

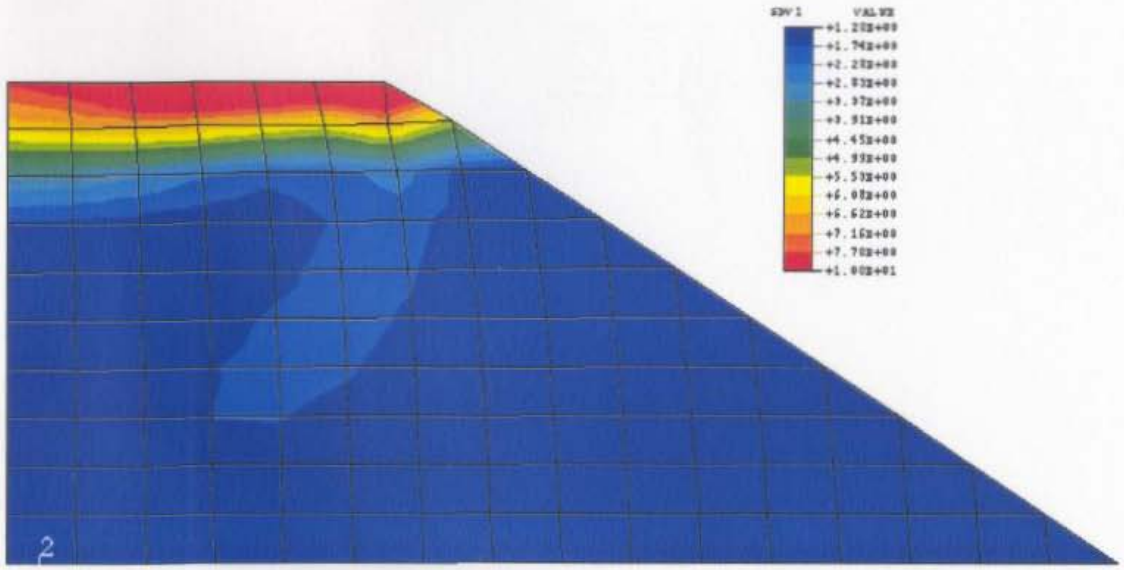

(c)

Figure 6.4 Damage evolution history: (a) damage contour before the peak load; (b)damage contour around the peak load; (c) damage contour just after the peak load.

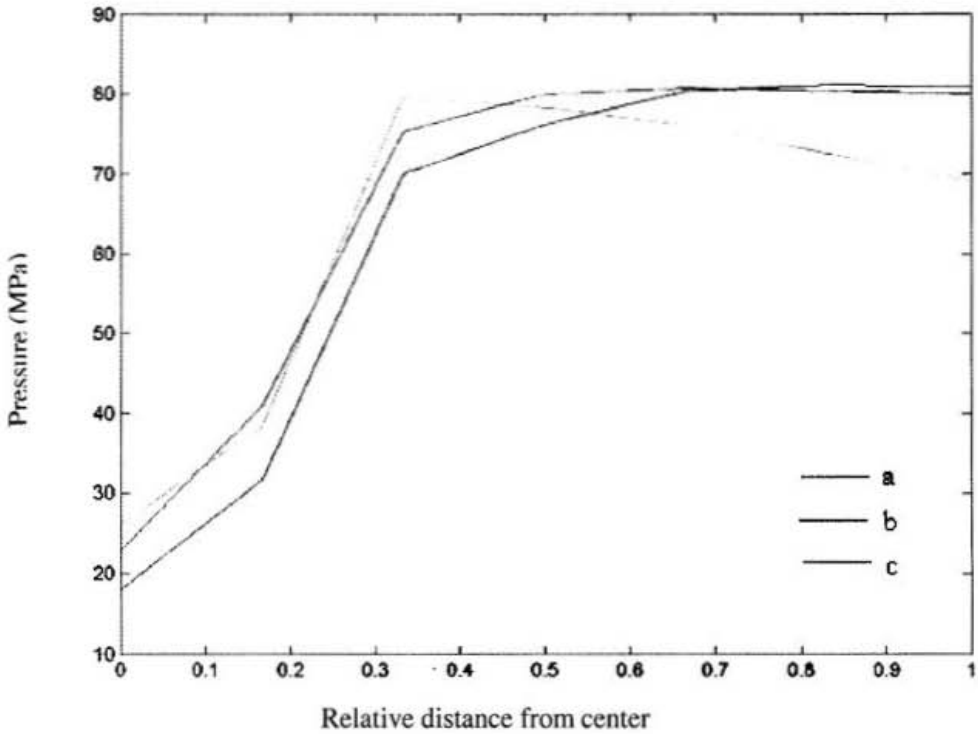

Figure 6.5 Pressure arrangement along the layer: (a) before the peak load; (b) around peak load; (c) just after peak load.

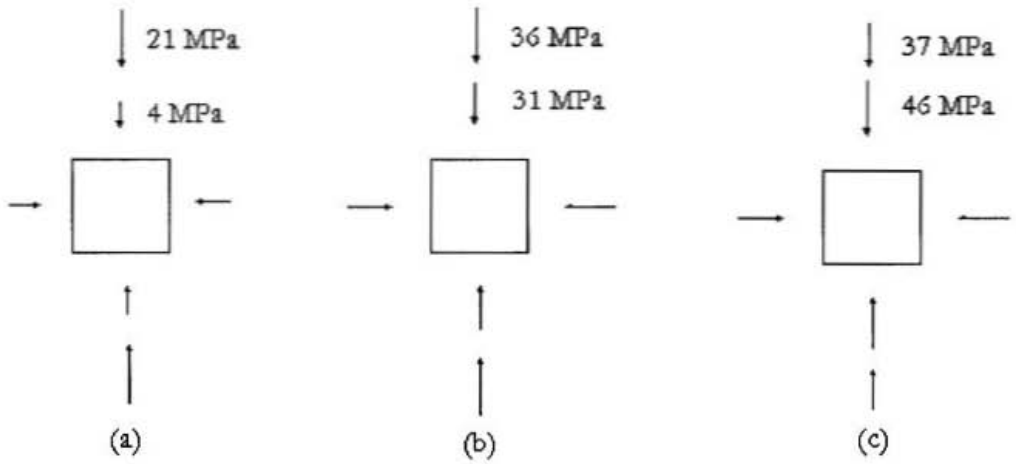

Figure 6.6 Comparison between von Mises and confining pressure at the peak load.(no scale) (a) the element at the edge; (b) the element at the middle of the edge and center; (c) the element at the centre

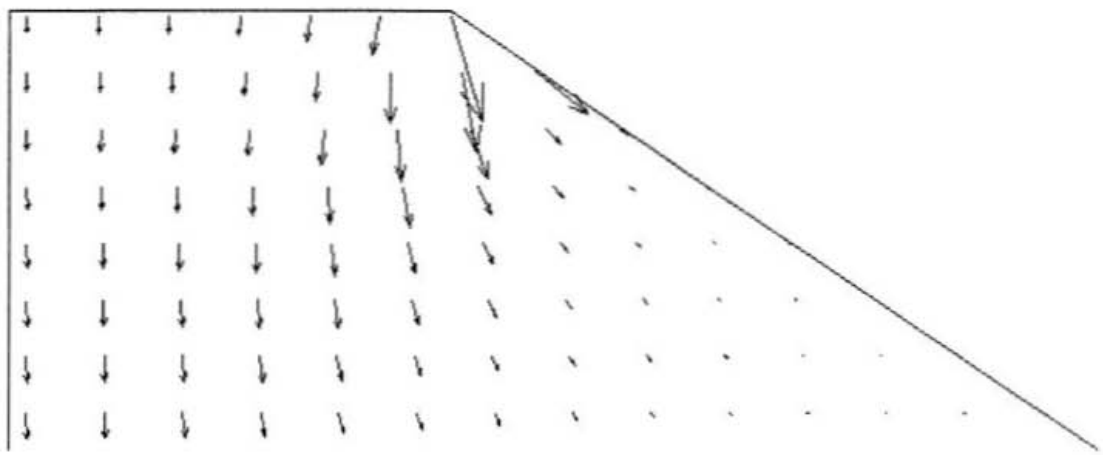

(a)

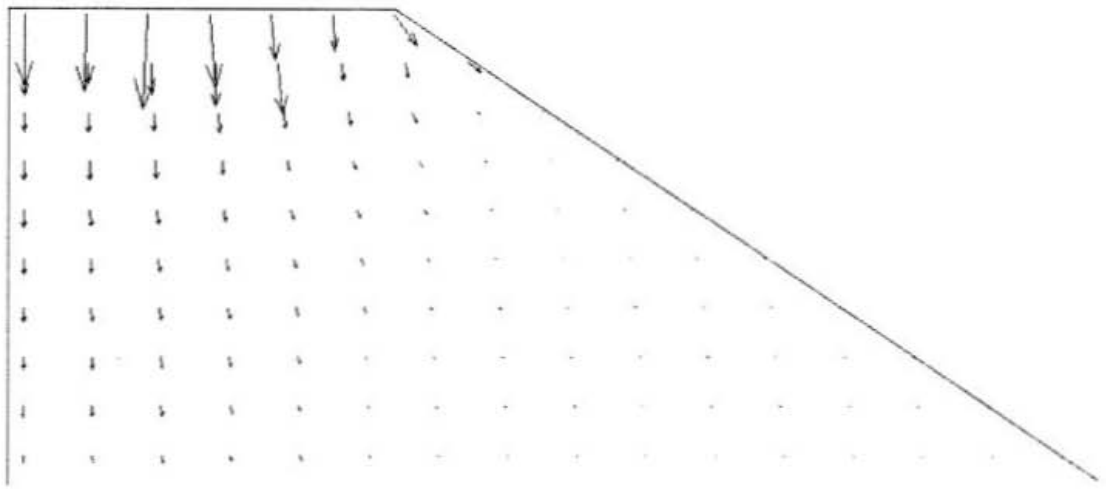

(b)

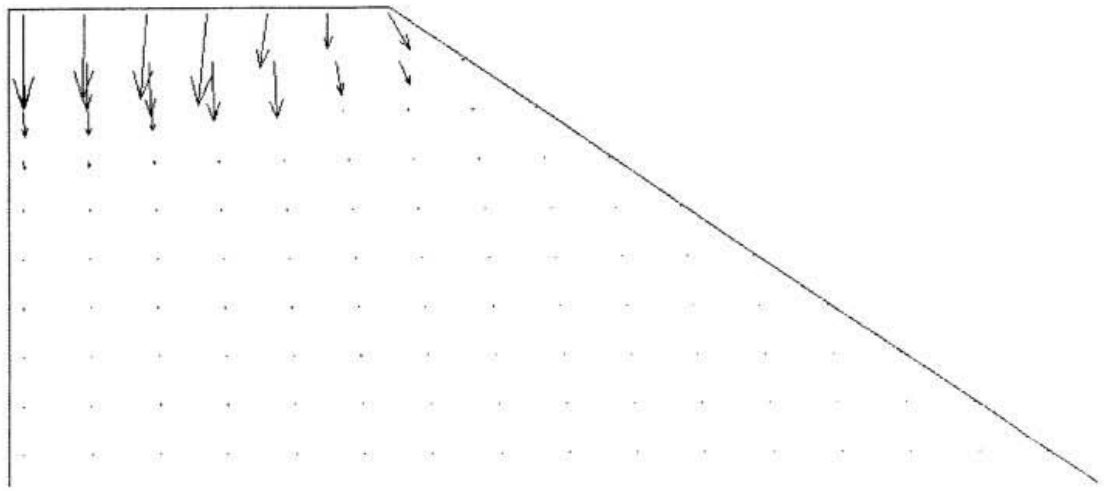

(c)

Figure 6.7 Energy flux evolution history: (a) time = 0.02 s; (b) time = 0.048 s; (c) time = 0.05 s.

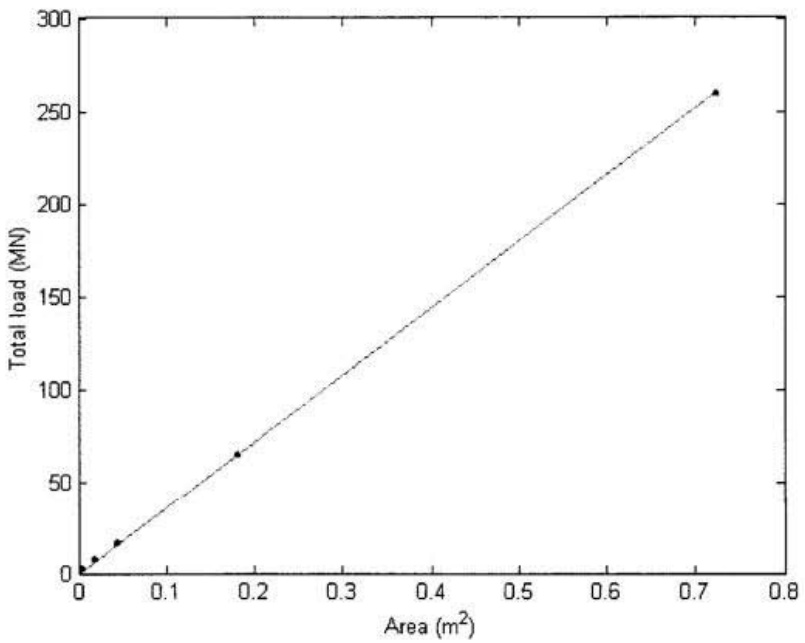

(a)

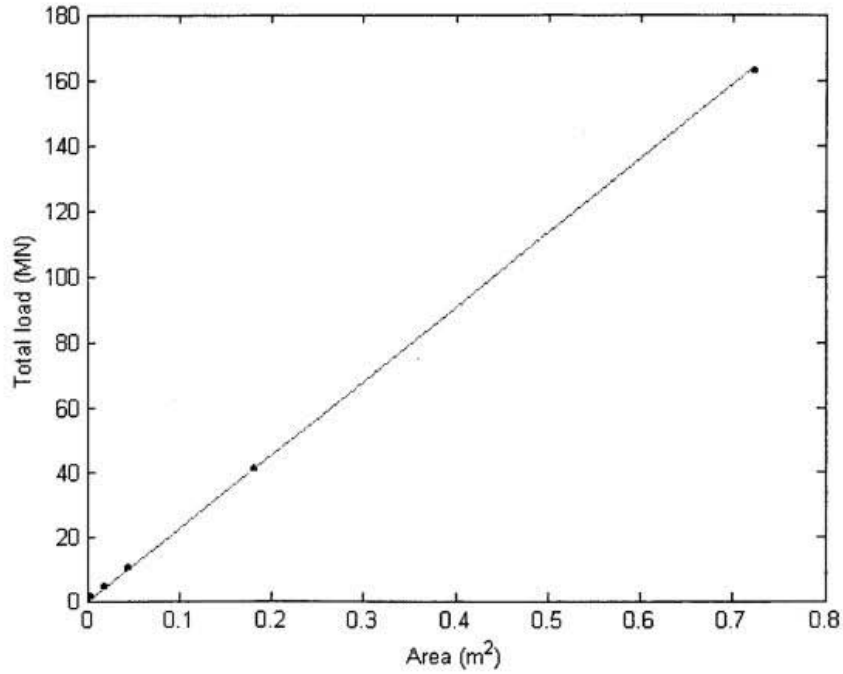
Total load (MN)
Area (m2)
0
20
40
60
80
100
120
140
160
180
0
0.1
0.2
0.3
0.4
0.5
0.6
0.7
0.8

(b)

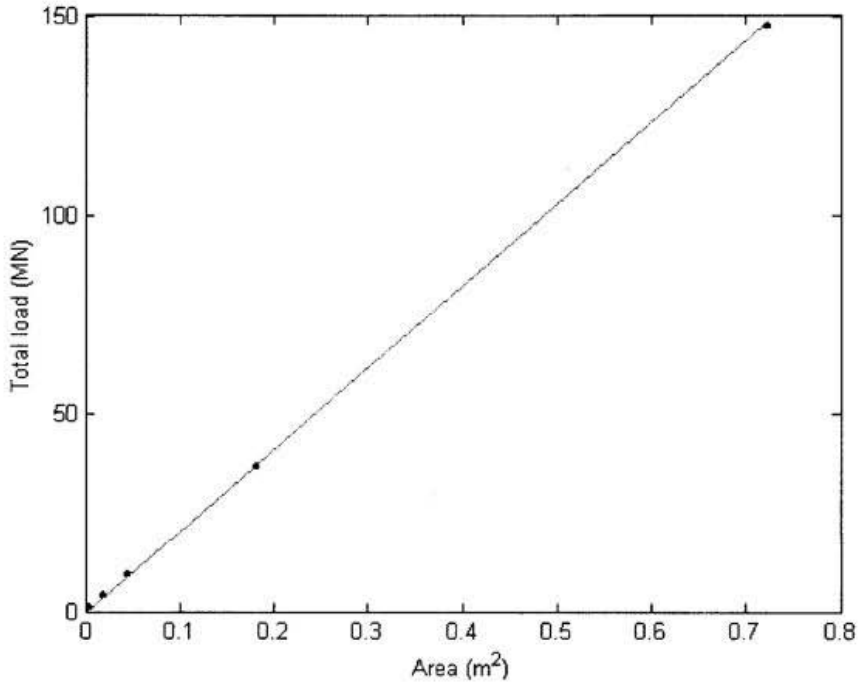
Total load (MN)
Area (m2)
0
50
100
150
0
0.1
0.2
0.3
0.4
0.5
0.6
0.7
0.8

(c)

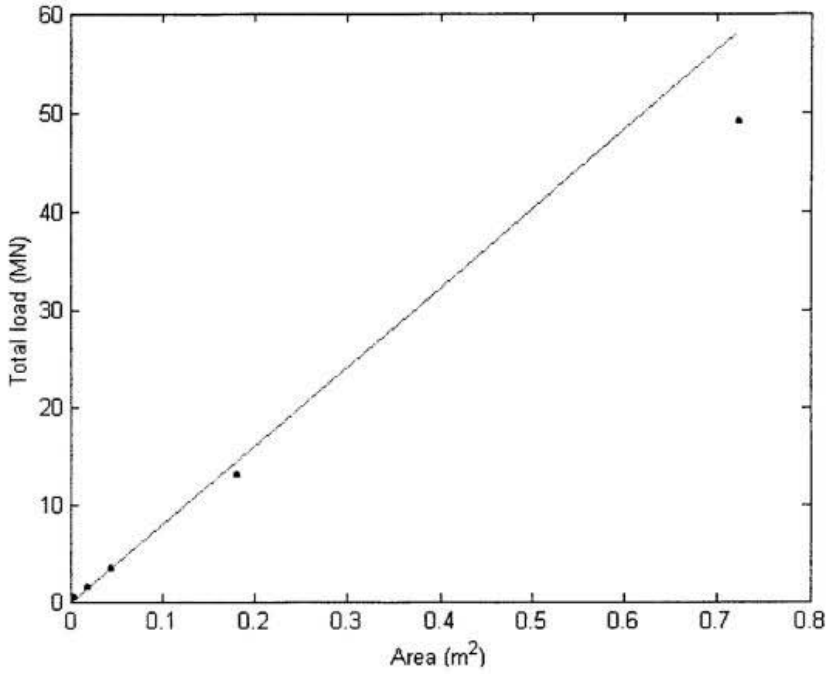

(d)

Figure 6.8 Force-area curve for (a) elastic material; (b) linear viscoelastic material; (c) nonlinear viscoelastic material without damage; (d) nonlinear viscoelastic material with damage (Solid line is the theoretical line without scale effect).

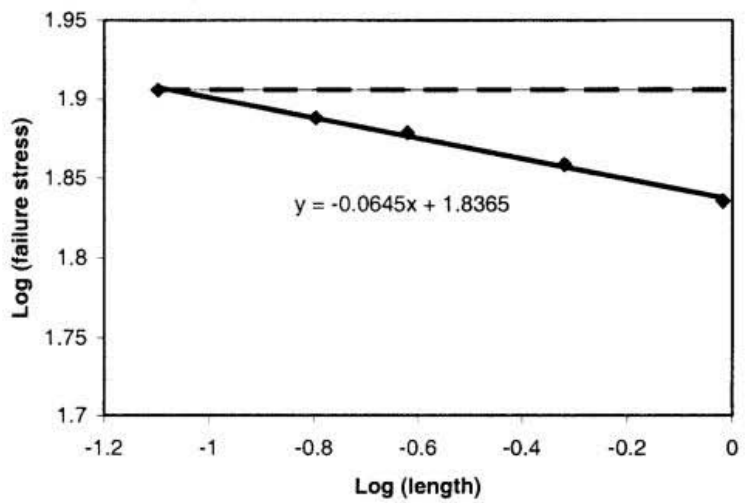

Figure 6.9 Scale effect for ice-structure indentation (dashed line is the theoretical line without scale effect).

Chapter 7

Conclusions and Recommendations

7.1 Conclusions

Medium-scale ice indentation tests on Hobson's Choice Ice Island were studied. A damaged layer was observed in these tests. Inside the layer, microcracks and the evidence of dynamic recrystallization and pressure melting were observed. The mechanisms of the formation of the damaged layer have been discussed. A schematic model by Jordaan (2001) was introduced to estimate the process of ice-structure interaction. This model outlines the process of formation of the damaged layer and the variation of stress distribution during the interaction. Triaxial small-scale tests carried out at Memorial University of Newfoundland showed clear evidence of an enhancement of strain and strain rate at large deformations. The effect of deviatoric stress, confining pressure and temperature on deformation history of ice is discussed. The failure modes of cylindrical ice specimens are investigated. Strain localization and rupture are the two main modes of

failure for laboratory (flawless) ice. Splitting was observed in specimens of iceberg ice with initial flaws. The pressure-temperature relationship of failed specimens showed that rupture tends to occur at low and high confining pressure levels and at relatively high temperature. The observations also showed that strain localization may be the precursor of the final rupture.

A constitutive model for triaxial loading conditions was developed from Glen's law coupled with damage mechanics. The enhancing effect of damage was described with an exponential form. The damage evolution model and calibration were obtained by a series of constant stress tests. The calibrated damage model was separated into two components. The first represents damage associated with microcracking at relatively low pressures while the second represents pressure softening effects such as dynamic recystallization and pressure melting at high pressures. An empirical temperature correction was made in calibrating the damage model. After the calibration, the damage evolution can be represented as a function of effective stress and confining pressure.

The mechanisms of instability due to strain localization are discussed in this thesis for general viscoelastic materials. It is concluded that inhomogeneity plays a significant role in triggering the strain localization. Finite element analyses based on the constitutive model coupled with damage mechanics were conducted to study the possible mechanisms of strain localization in ice. The analyses showed that both material imperfection and end effects can induce strain localization. Other mechanisms such as thermal effects were also discussed.

One of the medium-scale indentation tests was simulated with FEA to study the high-pressure zone. The results of the model showed a good agreement with the test data. Severe damage began from the edge of the contact interface and extended to the whole interface with a thin layer. Energy flux inside the ice mass also concentrated into the thin layer after peak load. These two phenomena give an illustration of the formation of the layer, and the softening of ice inside the layer and the drop-off of the reaction load. The stress distribution along the layer showed that the confining pressure is higher at the center than at the edge of the contact surface. This provides an explanation of the different mechanisms of damage initiation and growth of ice near the center and the edge. The scale effect in ice-structure interaction was also studied by finite element analysis. Results showed that for elastic materials, linear viscoelastic materials and nonlinear viscoelastic materials without damage effects, scale effect is excluded. For nonlinear materials with damage evolution, a small scale effect is observed but is far less extensive than the scale effect for ice subjected to failure with a preexisting crack.

7.2 Recommendations

1. Currently, a power law relationship is well accepted for constitutive relationship of ice. However, it is not that accurate for ice under large deformations (Jordaan *et al.*, 1999). For the further study, a more accurate model based on activation theory by Schapery (1997b) is recommended to replace Glen's law for ice undergoing a large deformation.

2. A special numerical technique is highly recommended to be developed for predicting the moment of initiation and post-behaviour of the material in the further study.

3. In the numerical study of the high-pressure zone, the decrease in pressure can reverse the damage after the peak load. It is therefore recommended to include this effect in the constitutive model. In the study of scale effect of the high-pressure zone, the physical mechanisms of the absence of significant scale effect need to be further studied. A set of small-scale tests under the same experimental conditions are highly recommended to be conducted together with a probabilistic analysis of the data.

References

Armero, F., 1999. Large-scale modeling of localized dissipative mechanism in a local continuum: applications to the numerical simulation of strain localization in rate-dependent inelastic solids. Mechanics of Cohesive-Frictional Materials. Vol. 4, pp. 101-131.

Anand, L., Kim, H. and Shawki, T.G., 1987. Onset of shear localization in viscoplastic solids,. J. Mech. Phys. Solids. Vol. 35, No.4, pp. 407-429.

Ashby, M.F. and Hallam, D.,1986. The failure of brittle solids containing small cracks under compressive stress states, Acta Metall. Vol.34 No. 3, pp.497-510.

Bandstra, J.P. and Kross, D.A., 2001. Modeling the ductile fracture process of void coalescence by void-sheet formation. Materials Science and Engineering. A319-321, pp. 490-495.

Barrette, P., 2001. Triaxial testing of ice: a survey of previous investigations. Proc. Conf. Port Ocean Engrg under Arct. Cond. (POAC), Ottawa, Vol. 3, pp. 1375-1384.

Barrette, P. 2002, in preparation, personal communication.

Bayliss, A., Belytschko, T., Kulkarni, M. and Lott-Vrumpler, D.A., 1994. On the dynamics and the role of imperfection for localization in thermo-viscoplastic materials. Modelling Simul. Mater. Sci. Eng. Vol. 2, pp. 941-964.

Bazant, Z.P., 1993. Scaling laws in Mechanics of failure. J. of Engrg. Mech., ASCE, Vol. 119(9), pp.1828-1844.

Belytschko, T., Moran, B. and Kulkarni, M., 1991. On the crucial role of imperfections in quasi-static viscoplastic solutions. Transactions of the ASME, Vol. 58, pp. 658-665.

Borja, R.I., Regueiro, R.A. and Lai, T.Y., 2000. FE modeling of strain localization in soft rock, Journal of Geotechnical and Geoenvironmental Engineering. Vol. 126, pp. 335-343.

Budiansky, B. and O'Connell, R.J., 1976. Elastic moduli of a cracked solid, International Journal of Solids and Structures, Vol.12, pp.81-97.

Cole, D.M., 1983. The relationship between creep and strength behaviour of ice at failure, Cold Regions Science and Technology, Vol. 8, pp. 189-197.

Cole, D.M., 1986. Effect of grain size on the internal fracturing of polycrystalline ice, CRREL Report 86-5.

Cole, D.M., 1989. Microfracture and the compressive failure of polycrystalline ice. Proceedings IUTAM / IAHR Symposium on Ice-Structure Interaction, St. John's, Newfoundland, Canada, pp.231-250.

Costin, L.S., Christman, E.E., Hawley, R.H. and Duffy, J., 1979. On the localization of plastic flow in mild stell tubes under dynamic torsional loading. J. Hardening, ed., Proceedings 2nd Conference on Mechanical properties at High Rates of Strain, Conference series No. 17 (Bristol and London), pp.90-100.

Duval, P., Ashby, M.F. and Anderman, I., 1983. Rate-controlling processes in the creep of polycrystalline ice, J. Phys. Chem., Vol. 87, pp. 4066-4074.

Dorris, J.F., 1989. A Plasticity Model for the Crushing of Ice. Proceedings IUTAM / IAHR. Symposium on Ice-Structure Interaction, St. John's, Newfoundland, Canada, pp.311-388.

Findley, W.N., Lai, J.S. and Onaran, K., 1976. Creep and relaxation of nonlinear viscoelastic materials. North-Holland Publishing Company.

Flugge, W. 1975. Viscoelasticity, Spinger-Verlag, New York.

Frederking, R.M.W., Blanchet, D., Jordaan, I.J., Kennedy, K., Sinha, N.K., Stander, E., 1990a. Field tests on Ice Indentation at medium scale, Ice Island. National Research Council of Canada Report CR 5866.1

Frederking, R.M.W., Jordaan, I.J. and McCallum, J.S., 1990b. Field tests of ice indentation at medium scale, Hobson's Choice Ice Island, Proc. 10th International IAHR Symposium on Ice, Espoo, Finland, Vol. 2, pp.931-944.

Glen, J.W., 1955. The creep of polycrystalline ice, Proceedings Royal Society of London, Piccadilly, London, W., Ser. A, Vol. 228, pp.519-538.

Glen, J.W., 1975. The mechanics of ice. Cold Regions Science and Engineering, Monograph 11-C2b.

Gold, L.M., 1972. The failure process in columnar-grained ice. Technical Paper No. 369, Division of Building Research, NRC.

Hallam, S.D., 1986. The role of fracture in limiting ice force. Proceedings of IAHR Ice Symposium, Iowa City, Iowa, pp. 287-319.

Hobbs, P.V., 1974. Ice physics. Clarendon Pres, Oxford.

Horii, H. and Nemat-Naser, S., 1983. Overall moduli of solids with microcracks: load-induced anisotropy. J. Mech. Phys. Solids, Vol. 31, No. 2. pp. 155-171.

Hutchion, J.W. and Neale, K.W., 1977, Influence of strain rate sensitivity on necking under uniaxial tension. Acta Metall., Vol. 25, pp. 839-846.

Jacka, T.H., and Maccagnan, M., 1984. Ice crystallographic and strain rate changes with strain in compression and extension. Cold Regions Science and Technology, Vol. 8, pp. 269-286.

Jonas, J.J. and Muller, F., 1969. Deformation of ice under high internal shear stresses, Canadian Journal of Earth Sciences, Vol. 6, pp.963-968.

Jones, S.J., 1982. The confined compressive strength of polycrystalline ice. Journal of Glaciology, Vol. 28, No. 98, pp. 171-177.

Jezek, K.C., Alley, R.B., and Thomas, R.H. 1985. Rheology of glarcier ice, Science Vol. 227, pp. 1335-1337.

Jordaan, I.J., Maes, M. and Nadreau, J.P., 1988. The crushing and clearing of ice in fast spherical indentation tests, OMAE' 88, Proceedings of the Seventh International Offshore Mechanics and Arctic Engineering Symposium, Vol. 4, New York, American Society of Mechanical Engineers, pp. 111-116.

Jordaan, I.J. and Mckenna, R.F., 1988. Constitutive relations for creep of ice. Proceedings International Association for Hydraulic Research (IAHR) Ice Symposium, Sapporo, Japan, Vol. 3, pp. 47-58.

Jordaan, I.J. and Timco, G.W., 1988. Dynamics of the ice crushing process. Journal of Glaciology, Vol. 34, No. 118, pp. 318-326.

Jordaan, I.J., McKenna, R.F., Duthinh, D., Fuglem, M.K., Kennedy, K.P., Maes, M.A. and Marshall, A. 1990. Development of new ice load models. Report for Canada Oil and Gas Lands Administration (COGLA) by (C-CORE), Memorial University of Newfoundland, St. John's, Newfoundland.

Jordaan, I.J. and McKenna, R.F., 1991. Processes of deformation and fracture of ice in compression. Proc. of IUTAM-IAHR Symposium on Ice-Structure Interaction, St. John's, Newfoundland, Canada, August 1989, Springer-Verlag, 1991, pp. 283-309.

Jordaan, I.J., Xiao, J., 1992. Interplay between damage and fracture in ice-structure interaction. Proceeding of IAHR Ice Symposium, Banff, Alberta.

Jordaan, I.J., Maes, M.A., Brown, P.W. and Hermans, I.P., 1993. Probabilistic analysis of local ice pressures. Journal of Offshore Mechanics and Arctic Engineering, Vol. 115, pp.83-89.

Jordaan, I.J., Matskevitch, D.G., Meglis, I.L., 1999.Disintegration of ice under fast compressive loading. International Journal of Fracture. Vol. 97, pp.279-300.

Jordaan, I.J., 2001. Mechanics of ice-structure interaction. Engineering Fracture Mechanics, Vol. 68, pp. 1923-1968.

Kachanov, L.M., 1958. On the creep rupture time. Izv. An SSSR, Ofd. Tekhn. Nauk., No.8, pp. 26-31.

Kachanov, L.M., 1986. Introduction to continuum damage mechanics. Martinus Nijhoff Publishers.

Kachanov, M., 1993. Elastic solids with many cracks and related problems. Advanceds in Applied Mechanics, Vol. 30, Academic Press.

Kalifa, P., Duval, P. and Ricard, M., 1989. Crack nucleation in polycrystalline ice under compressive states. Proceedings, OMAE, A.S.M.E., Vol. 4, pp. 13-21.

Kalifa, P., Ouillon, G., and Duval, P., 1992. Microcracking and the failure of polycrystalline ice under triaxial compression. Journal of Glaciology, Vol. 38, No. 128, pp. 65-76.

Karr, D.G., 1985. A damage mechanics model for uniaxial deformation of ice. OMAE'85, Vol. 2, pp. 227-233.

Karr, D.G. and Choi, K., 1989. A three-dimensional constitutive damage model for polycrystalline ice. Mech. Mater., Vol. 8, pp.55-66.

Krajcinovic, D. and Fonseka, G.U., 1981. The continous damage theory of brittle materials: Pat1: General theory. Journal of Applied Mechanics. Vol. 48, pp.809-815.

Krajcinovic, D., 1983. Constitutive equations for damaging materials. Journal of Applied Mechanics. Vol. 50, pp.355-360.

Krajcinovic, D. 1985. Continous damage mechanics revisited: Basic concepts and definitions. Journal of Applied Mechanics, Vol. 52, pp.829-834.

Lavrov, v.v., 1973. Scale effects as indications of ice-breaking mechanism. In *Studies in ice physics and ice engineering*. Yakovlev.

Liu, B., 1994. Numerical modeling of medium scale indentation tests. Master Thesis in Memorial University of Newfoundland.

McKenna, R.F., Meyssonnier, J. and Jordaan, I.J., 1989. Peak pressures from a damage model for ice in compression. Proc. of the 8th International Conference on Offshore Mechanics and Arctic Engineering, the Hague, Netherlands, Vol. 4, pp. 67-73.

Meglis, I.L., Melanson, P.M., Jordaan, I.J., 1999. Microstructural change in ice: II. Creep behavior under triaxial stress conditions. Journal of Glaciology. Vol. 45, No. 151, pp. 438-448.

Melanson, P.M., 1998. Damage and microstructural change in laboratory grown ice under high pressure zone conditions. M. Eng. Thesis, Memorial University of Newfoundland, St. John's, Newfoundland.

Melanson, P.M., Jordaan, I.J. and Meglis, I.L., 1998. Modelling of damage in ice. Proceedings, IAHR Symposium on Ice, Potsdam, New York.

Melanson, P.M., Meglis, I.L., Jordaan, I.J. and Stone, B.M., 1999. Microstructural change in ice: I. Constant-deformation-rate tests under triaxial stress conditions. Journal of Glaciology, Vol. 45, No.151, pp. 417-422.

Mellor, M., and Cole, D.M., 1983. Deformation and failure of ice under constant stress or constant strain-rate. Cold Regions Science and Technology, Vol. 5, pp. 201-219.

Mellor, M., 1983. Mechical behaviour of sea ice, U.S. Army Cold Region Research and Engineering Lab, Honover, CRREL Report 83-1.

Molinari, A. and Clifton, R.J., 1987. Analysis characterization of shear localization in thermoviscoplastic materials. Transactions of the ASME, Vol. 54, pp.806-812.

Murrell, S.A.F., Sammonds, P.R. and Rist, M.A., 1991. Strength and failure modes of pure ice and multi-year sea ice under triaxial loading. Proceedings of Symposium on Ice Structure Interaction, IUTAM / IAHR, St. John's, NF, Canada, pp. 339-361.

Needleman, A., 1988. Material rate dependence and mesh sensitivity in localization problems. Computer Methods in Applied Mechanics and Engineering. Vol. 67, pp. 69-85.

Muggeridge, K.J., Jordaan, I.J., 1999. Microstructural change in ice: III. Observations from an iceberg impact zone. Journal of Glaciology, Vol. 45, No. 151, pp. 449-455.

Needleman, A., 1991. On the competition between failure and instability in progressively softening solids. Transactions of the ASME. Vol. 58, pp. 294-298.

Nordell, B., 1990. Measurement of P-T coexistence curve for ice-water mixture. Cold Regions Science and Technology, Vol. 19, pp. 83-88.

Orsini, V.C. and Zikry, M.A., 2001. Void growth and interaction in crystalline materials. International Journal of Plasticity. Vol. 17, pp. 1393-1417.

Poirier, J.P. and Guillope, M., 1979. Deformation-induced recrystallization of minerals. Bull. Mineral., Vol. 102. pp. 67-74.

Poirier, J.P., 1985. Creep of crystals. Cambridge University Press, London.

Rist, M.A., Murrel, S.A.F. and Sammonds, P.R., 1988. Experimental results on the failure of polycrystalline ice under triaxial stress conditions. Proceedings of 9th IAHR Conference, Sapporo, pp. 118-127.

Rist, M.A., and Murrel, S.A.F., 1994. Ice triaxial deformation and fracture. Journal of Glaciology, Vol. 40, No. 135, pp. 305-318.

Rist, M.A., Jones, S.J. and Slade, T.D., 1994. Microcracking and shear fracture in ice. Annals of Glaciology, Vol. 19, pp. 131-137.

Sanderson, T.J.O. 1988. Ice Mechanics_Risks to Offshore Structures, Graham and Trotman.

Sayers, C.M. and Kachanov, M. 1991. A simple technique for finding effective elastic constants of cracked solids for arbitrary crack orientation statistics. International Journal of Solids and Structures. Vol. 27, No. 6. pp 671-680.

Schapery, R.A., 1981. On viscoelastic deformation and failure behaviour of composite materials with distributed flaws. Advances in Aerospace Structures and Materials, The American Society of Mechanical Engineers, pp.5-20.

Schapery, R.A., 1984. Correspondence principles and a generalized J-Intergral for large deformation and fracture analysis of viscoelastic media. Int. Journal of Fracture, Vol. 25., pp.195-223.

Schapery, R.A., 1991. Models for the deformation behaviour of viscoelastic media with distributed damage and their applicability to ice. Proc. of Symposium on Ice-Structure Interaction, IUTAM/IAHR, St. John's, NF., Canada, pp.191-230.

Schapery, R.A., 1997a. Thermalviscoelastic constitutive equations for polycrystalline ice. Journal of Cold Regions Engineering. Vol.11, No. 2, pp.146-157.

Schapery, R.A., 1997b. Nonlinear viscoelastic and viscoplastic constitutive equations based on thermodynamics. Mechanics of Time-Dependent Materials, Vol. 1, pp. 209-240.

Schulson, E.M. and Cannon, N.P., 1984. The effect of grain size on the compressive strength of ice. IAHR Ice Symposium, Hamburg. Pp. 24-38.

Schulson, E.M., 1987. The fracture of ice Ih, J. de Physique. Vol. 48: C1-207-220.

Schulson, E.M., Hoxie, S.G. and Nixon, W.A., 1989. The tensile strength of cracked ice. Phil. Mag., Vol. 59, pp. 303-311.

Schulson, E.M., Jones, D.E. and Kuehn, G.A., 1991. The effect of confinement on the brittle compressive fracture of ice. Annals of Glaciology, Vol. 15, pp.216-221.

Schwarz, J., and Weeks, W.F., 1977. Engineering properties of sea ice. Journal of Glaciology, Vol. 19, No. 81, pp. 499-531.

Seng-Kiong, T. and Shyam Sunder, S., 1985. Constitutive modeling of sea ice with applications to indentation problems. CSEOE Research Report No. 3, MIT, Cambridge, Massachusetts.

Shawki, T.G., 1994. An energy criterion for the onset of shear strain localization in thermal viscoplastic materials, Part I: Necessary and sufficient initiation conditions. Transactions of the ASME, Vol. 61, pp. 530-537.

Singh, S.K., 1993. Mechanical behaviour of viscoelastic material with changing microstrucure. Ph.D Thesis, Memorial University of Newfoundland.

Sinha, N.K., 1978. Rheology of columnar-grained ice, Experimental Mechanics. Vol. 18, No. 12, pp. 464-470.

Sinha, N.K., 1979. Grain boundary sliding in polycrystalline materials. Phil. Mag. A, Vol. 40, pp. 825-842

Sinha, N.K., 1982. Delayed elastic strain criterion for first cracks in ice. Proc. of the symposium on deformation and failure of granular materials, pp. 323-330. Rotterdam: Balkema.

Sinha, N.K., 1983. Creep model of ice for monotonically increasing stress. Cold Regions Science and Technology, Vol. 8, pp. 25-33.

Sinha, N.K., 1989. Elasticity of natural types of polycrystalline ice. Cold Regions Science and Technology, Vol. 17, pp. 127-135.

Smith, T.R., and Schulson, E.M., 1993. The brittle compressive failure of fresh-water columnar ice under biaxial loading. Acta Metall. Mater., Vol. 41, pp. 153-163.

Sodhi, D.S., 2000. Absence of size effect in brittle crushing and breakthrough loads of floating ice sheets. IUTAM Symposium on Scaling Laws in Ice Mechanics and Ice Dynamics, Fairbanks, Alaska, USA, pp.55-65.

Stone, B.M., Jordaan, I.J., Jones, S.J. and McKenna, R.F., 1989. Damage of isotropic polycrystalline ice under moderate confining pressures. Proceedings of the 10th International Conference on port and Ocean Engineering Under Arctic Conditions, Lulea, Sweden, Vol. 1, pp. 408-419.

Stone, B.M., Jordaan, I.J., Xiao, J. and Jones, S.J., 1997. Experiments on the damage process in ice under compressive states of stress. Journal of Glaciology, Vol. 43, No. 143, pp. 11-25.

Urai, J.L., Humphrers, F.J. and Burrows, S.E., 1980. In-situ studies of the deformation and dynamic recrystallization of rhombhedral camphor. Journal of Materials Science, Vol. 15, pp. 1131-1240.

Urai, J.L., Means, W.D.M. and Lister, G.S. (1986) Dynamic recrystallization of minerals. American Geophysical Union, Geophysical Monograph 36 (the Paterson volume), pp. 161-199.

Vernon. R.H., 1981. Optical Microstructure of partly recrystallized calcite in some naturally deformed marbles. Tectonophysics, Vol. 78, pp. 601-612.

Wang, Y.S., 1981. Uniaxial Compression Testing of Arctic Sea Ice. Proc. Of 6th POAC, Vol. 1, pp. 346-355.

Weiss, J. and Schulson, E.M., 1995. The failure of fresh-water granular ice under multiaxial compressive loading. Acta Metallurgica et Materialia, Vol. 43, pp. 2303-2315.

Xiao, J. 1991. Finite element modeling of damage processes in ice-structure interaction. M. Eng Thesis, Memorial University of Newfoundland, St. John's, Newfoundland.

Xiao, J. and Jordaan, I.J., 1996. Application of Damage Mechanics to Ice Failure in Compression. Cold Regions Science and Technology, Vol. 24, pp. 305-322.

Xiao, J. 1997. Damage and fracture of brittle viscoelastic solids with application to ice load models. Ph.d Thesis, Memorial University of Newfoundland, St. John's, Newfoundland.